

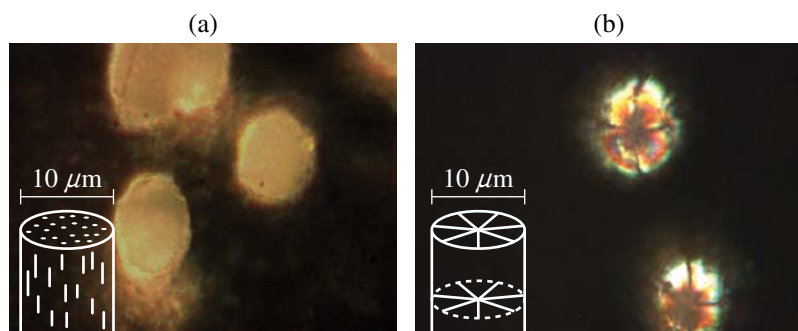
LLE Review

Quarterly Report



About the Cover:

The cover photo shows Department of Chemistry master's student Eric Glowacki inserting a photoswitchable gas permeation membrane into a permeation chamber for testing. Eric, along with LLE advisor Ken Marshall, undergraduate student Karen Horowitz, and Dept. of Chemical Engineering professor Ching Tang has for the first time devised and fabricated a unique type of membrane that changes its permeability to gas merely by shining light onto its surface. This "photoswitching" of the gas permeability is reversible through alternating illumination by ultraviolet and visible light. Photoswitching in these membranes is made possible by tiny micropores filled with light-sensitive liquid crystals, synthesized at LLE, which change their molecular arrangement under certain illumination conditions.



The photos at the left show polarized optical microscopy (POM) images of the liquid crystal filled pores in the photoswitchable membranes. The size of the pores is approximately 10 μm . Images (a) and (b) exhibit different orientations of the liquid crystal molecules.

This report was prepared as an account of work conducted by the Laboratory for Laser Energetics and sponsored by New York State Energy Research and Development Authority, the University of Rochester, the U.S. Department of Energy, and other agencies. Neither the above named sponsors, nor any of their employees, makes any warranty, expressed or implied, or assumes any legal liability or responsibility for the accuracy, completeness, or usefulness of any information, apparatus, product, or process disclosed, or represents that its use would not infringe privately owned rights. Reference herein to any specific commercial product, process, or service by trade name, mark, manufacturer, or otherwise, does not necessarily constitute or imply its endorsement, recommendation, or favoring by

the United States Government or any agency thereof or any other sponsor. Results reported in the LLE Review should not be taken as necessarily final results as they represent active research. The views and opinions of authors expressed herein do not necessarily state or reflect those of any of the above sponsoring entities.

The work described in this volume includes current research at the Laboratory for Laser Energetics, which is supported by New York State Energy Research and Development Authority, the University of Rochester, the U.S. Department of Energy Office of Inertial Confinement Fusion under Cooperative Agreement No. DE-FC52-08NA28302, and other agencies.

Printed in the United States of America

Available from

National Technical Information Services

U.S. Department of Commerce

5285 Port Royal Road

Springfield, VA 22161

Price codes: Printed Copy A04

Microfiche A01

For questions or comments, contact Kenneth S. Anderson, Editor, Laboratory for Laser Energetics, 250 East River Road, Rochester, NY 14623-1299, (585) 275-9352.

Worldwide-Web Home Page: <http://www.lle.rochester.edu/>

LLE Review

Quarterly Report



Contents

In Brief	iii
Photoswitchable Gas Permeation Membranes Based on Liquid Crystals	63
High-Intensity Laser–Plasma Interaction with Wedge-Shaped–Cavity Targets	72
Crossed-Beam Energy Transfer in Inertial Confinement Fusion Implosions on OMEGA	79
Characterization of Highly Stable, Mid-IR, GaSb-Based Laser Diodes	85
A Reduced Particle-in-Cell Model for Two-Plasmon-Decay Instability	88
Publications and Conference Presentations	

In Brief

This volume of the LLE Review, covering January–March 2010, features “Photoswitchable Gas Permeation Membranes Based on Liquid Crystals” by E. Głowacki, K. Horovitz, C. W. Tang, and K. L. Marshall. In this article (p. 63), the authors report the fabrication of switchable gas permeation membranes in which a photoswitchable low-molecular-weight liquid crystalline (LC) material acts as the active element. Liquid crystal mixtures are doped with mesogenic azo dyes and infused into commercially available track-etched membranes with regular cylindrical pores (0.40 to 10.0 μm). Tunability of mass transfer can be achieved through a combination of (1) LC/mesogenic dye composition, (2) surface-induced alignment, and (3) reversible photoinduced LC-isotropic transitions. Photo-induced isothermal phase changes in the imbibed material afford large and fully reversible changes in the permeability of the membrane to nitrogen. Both the LC and photogenerated isotropic states demonstrate a linear permeability/pressure relationship, but they show significant differences in their permeability coefficients. Liquid crystal compositions can be chosen such that the LC phase is more permeable than the isotropic—or vice versa—and can be further tuned by surface alignment. Permeability switching response times are 5 s, with alternating UV and $>420\text{-nm}$ radiation at an intensity of 2 mW/cm^2 being sufficient for complete and reversible switching. Thermal and kinetic properties of the confined LC materials are evaluated and correlated with the observed permeation properties. This is the first demonstration of reversible permeation control of a membrane with light irradiation.

Additional highlights of research presented in this issue include the following:

- W. Theobald, S. Ivancic, B. Eichman, P. M. Nilson, J. A. Delettrez, R. Yan, G. Li, F. J. Marshall, D. D. Meyerhofer, J. F. Myatt, C. Ren, T. C. Sangster, C. Stoeckl, and J. D. Zuegel (LLE), V. Ovchinnikov, L. Van Woerkom, and R. R. Freeman (Ohio State University), and K. U. Akli, E. Giraldez, and R. B. Stephens (General Atomics) present experiments of high-intensity, short-pulse laser–plasma interactions with small-mass copper (Cu) wedge-shaped–cavity targets (p. 72). Experimental diagnostics provided spatially and spectrally resolved measurements of the Cu K_α line emission at 8 keV. The coupling efficiency of short-pulse laser energy into fast electrons was inferred from the x-ray yield for wedge opening angles between 30° and 60° and for *s*- and *p*-polarized laser irradiation. Up to $36\pm 7\%$ coupling efficiency was measured for the narrowest wedge with *p*-polarization. The results are compared with predictions from two-dimensional particle-in-cell simulations.
- I. V. Igumenshchev, D. H. Edgell, V. N. Goncharov, J. A. Delettrez, A. V. Maximov, J. F. Myatt, W. Seka, A. Shvydky, S. Skupsky, and C. Stoeckl model crossed-beam energy transfer in inertial confinement fusion implosions on OMEGA (p. 79). Radiative hydrodynamic simulations of implosion experiments on the OMEGA Laser System show that energy transfer between crossing laser beams can significantly reduce laser absorption. A new quantitative model for crossed-beam energy transfer has been developed, allowing one to simulate the coupling of multiple beams in the expanding corona of implosion targets. Scattered-light and bang-time measurements show good agreement with predictions of this model when nonlocal thermal transport is used. The laser absorption can be increased by employing two-color light, which reduces the crossed-beam energy transfer.

- V. Okishev (LLE), D. Wang, L. Shterengas, and G. Belenky (State University of New York at Stony Brook), and D. Westerfeld (Power Photonic Corporation) report on highly stable, room-temperature, mid-IR, GaSb-based laser diodes (p. 85). Such laser diodes have been characterized at various temperatures and driver currents. Up to 54 mW of output laser power was demonstrated in a 3150- to 3180-nm wavelength range with <20-nm FWHM spectral width.
- H. X. Vu (University of California, San Diego), D. F. DuBois and D. A. Russell (Lodestar Research Corporation), and J. F. Myatt (LLE) present an extension of the fully kinetic, reduced-description, particle-in-cell (RPIC) methodology to model two-plasmon-decay instability (TPD) (p. 88). This work is motivated by the recent resurgent interest in suprathermal electron generation by TPD in direct-drive laser fusion. RPIC provides a computationally efficient, fully kinetic simulation tool, especially in nonlinear regimes where Langmuir decay instability (LDI) is a dominant saturation mechanism. This RPIC methodology is an extension of the modeling of laser-plasma instabilities in underdense plasmas reported previously. The relationship between RPIC and the extended Zakharov model previously used for TPD is explored theoretically and tested in simulations. The modification of the electron velocity distribution—in particular, the generation of hot electrons—as calculated in RPIC leads to weakening of the wave turbulence excited by TPD compared to the Zakharov model predictions but the locations in wave vector space of important spectral features, e.g., arising from the LDI, of the nonlinear wave fluctuations are exactly the same in the two approaches. New results involving two oblique, overlapping laser beams, a common geometrical feature in direct-drive schemes, are presented. The two laser beams can cooperatively excite common primary Langmuir waves, which initiate the LDI process.

Kenneth S. Anderson
Editor

Photoswitchable Gas Permeation Membranes Based on Liquid Crystals

Introduction

Research in the field of high-performance gas permeation membranes has, to date, focused on maximizing both mass transfer and selectivity. Although gateable interconnect membranes for liquids have evolved to a mature level, the development of gas membranes whose permeability can be controlled during operation or tuned to respond to changes in their environment is an important goal that has yet to be realized.^{1,2} Such “smart” materials are in high demand for smaller-scale membrane applications such as microanalysis, reactor devices, and also larger batch processes.² Our goal was to create a novel and scaleable membrane system to achieve complex chemical and fluidic manipulations controllable by external stimuli.

Our inspiration for employing liquid crystal materials as the “active” element for switchable and tunable gas separation membranes comes from two sources: (1) biological membranes composed of various types of lyotropic liquid crystal phospholipids, which, because of their enhanced ordering, make it possible to control reversible structural modifications and corresponding permeation changes, and (2) synthetic polymer-based membranes, where the sorption–diffusion process is controlled by segmental mobility and the free volume of the material. Primary relaxation processes of polymers, such as the glass transition, correspond to large changes in sorption–diffusion characteristics.³

Mesogenic materials offer a range of thermotropic secondary transitions that can potentially afford unique and tunable materials for permeation membranes. In the early 1980s Kajiyama and co-workers were the first to exploit these properties of mesogenic materials in a series of polymer-dispersed liquid crystal (PDLC) membranes. Such a system has many of the advantages of a liquid-diffusing phase, such as high mobility of permeants, yet retains the mechanical properties of a polymeric material. LC–polymer composites have been exploited for light-controlled active transport of metal ions; however, the majority of efforts have focused on harnessing thermotropic control. These PDLC systems demonstrated significant deviations in their permeation properties at both

the crystalline–nematic and the nematic–isotropic transition temperatures.⁴ An obvious caveat is that using changes in temperature to vary the permeability of the membrane material is intrinsically coupled to the kinetics of the permeant. Employing thermal events to tune permeability can be not only energy intensive but for many applications may also have an unacceptably long response time because of unfavorable thermal transport characteristics of polymer materials. Although thermally induced LC phase changes have been successful for controlling permeation in drug delivery applications,⁵ the primary aim of this work was to avoid the complications mentioned above by evaluating the permeation characteristics of LC materials under isothermal conditions.

To generate phase changes isothermally, a technique was adopted that is well established in LC photonics—using photochromic dyes that demonstrate a photomechanical effect. Azobenzene derivatives are among the most-studied and frequently employed photochromic dyes that convert incident light to mechanical energy through the process of *trans-cis* isomerization. Appropriate substitution at the *para* positions affords azobenzene derivatives, where the *trans* form is mesogenic because of its rod-like shape. In contrast, the *cis* isomer’s bent shape substantially perturbs LC ordering. This effect is illustrated in Fig. 122.1.

Several demonstrations of bulk nematic- to isotropic-phase changes induced by *trans-cis* photoisomerization in azobenzenes have been conducted in both low-molar-mass and polymeric systems. This “photomechanical” effect has been exploited to generate numerous types of reversible changes when azobenzene materials are added as “guest” dopants to both fluid and polymer “hosts.” Several extensive reviews document the azobenzene photomechanical effect in bulk materials.⁶

For efficient photoswitching in LC-based permeation membranes, the concentration of azobenzene absorbers in the LC host must be carefully selected to be large enough to effectively induce an isothermal phase shift but not large enough to pre-

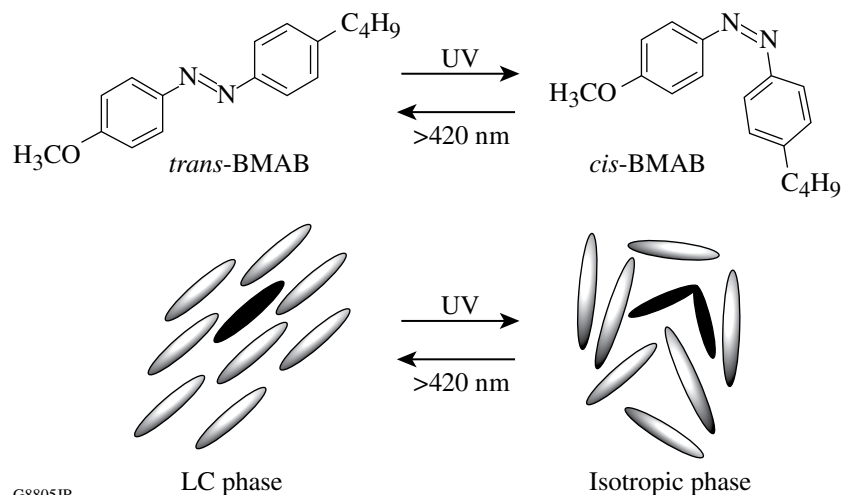


Figure 122.1

Photomechanical effect of 4-butyl-4'-methoxyazobenzene (BMAB) utilized to afford reversible isothermal LC-isotropic phase transitions.

vent penetration of the activating optical radiation throughout the bulk of the film. The particularly high molar extinction coefficient of azobenzenes makes it especially important to limit their content in the membranes to ensure that the entire depth of the film is actuated. Two azo-containing eutectic LC mixtures were prepared (Fig. 122.2). The azobenzene dye 4-butyl-4'-methoxyazobenzene (BMAB) has been used extensively as a photoresponsive mesogenic chromophore to generate refractive-index changes in thin polymer films⁷ and for optical data storage;⁸ it has also been incorporated at 15 wt% in a eutectic mixture with Merck E7 for photoswitching between the nematic and isotropic phases.⁸

To study the influence of chemical composition on permeation, a second eutectic mixture (Eutectic 2) based on the

phenyl benzoate LC materials 4-pentyl-4'-methoxybenzoate (PPMeOB) and 4-pentyl-4'-pentoxybenzoate (PPPOB) was used along with 4-ethoxy-4'-hexanoylazobenzene (EHAB) as the azobenzene dopant. Because both Eutectic 1 and Eutectic 2 have similar nematic ranges, viscosities, and dye content, these systems represented a nearly ideal “matched set” for evaluating the relationship of chemical composition of the LC phase on gas permeability in the confined membrane environment.

Photoswitchable membranes were fabricated either by dispersing the azobenzene-doped LC eutectic mixture into a host polymer solution and casting as a PDLC membrane as described by Kajiyama *et al.*⁷ or by imbuing the LC material directly into the cylindrical “track-etched” micropores of a commercial polycarbonate (Isopore) membrane. Isopore mem-

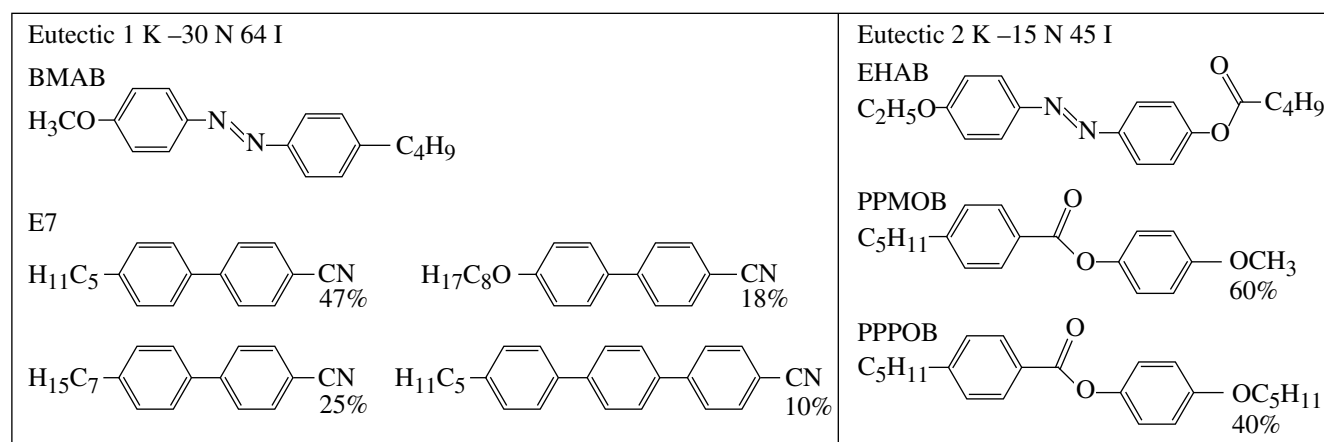


Figure 122.2

Molecular compositions and thermal properties of the two LC mixtures used.

branes are formed by bombardment with high-speed alpha particles, followed by chemically etching the damaged radiation tracks to produce cylindrical pores with remarkably smooth cavity surfaces. Previous studies of nematic LC materials confined in such a micropore environment have shown that the pore walls function as a homogenous alignment surface, resulting in the nematic director field configuration being uniaxial and parallel with respect to the pore wall.⁹ To test the effect of the LC alignment state (parallel or perpendicular to the pore walls) on permeation, the pore walls were treated with the reactive silane n-octyltriethoxysilane (OTS). Figure 122.3 shows a schematic diagram of how a photoswitchable LC material imbedded into a porous polymer membrane could be used for gas-phase switching and tuning applications. Using the well-defined, cylindrically symmetrical, preformed porous structure of the

membrane makes it possible to directly and conveniently probe the permeation properties of the photoswitchable LC host in the membrane as a function of LC orientation and irradiation. Porous membranes imbued with LC proved to be much better candidates than PDLC materials. We characterized the optical, thermal, and orientational properties of the confined LC eutectics and evaluated their permeation qualities, along with demonstrating reversible permeation control of nitrogen gas.

Results and Discussion

1. Photocontrollable PDLC Membranes

Our initial attempts focused on creating PDLC's for functional gas permeation membranes in a manner similar to that reported by Kajiyama *et al.*³ The major challenge in fabricating PDLC membranes for permeation applications is that the

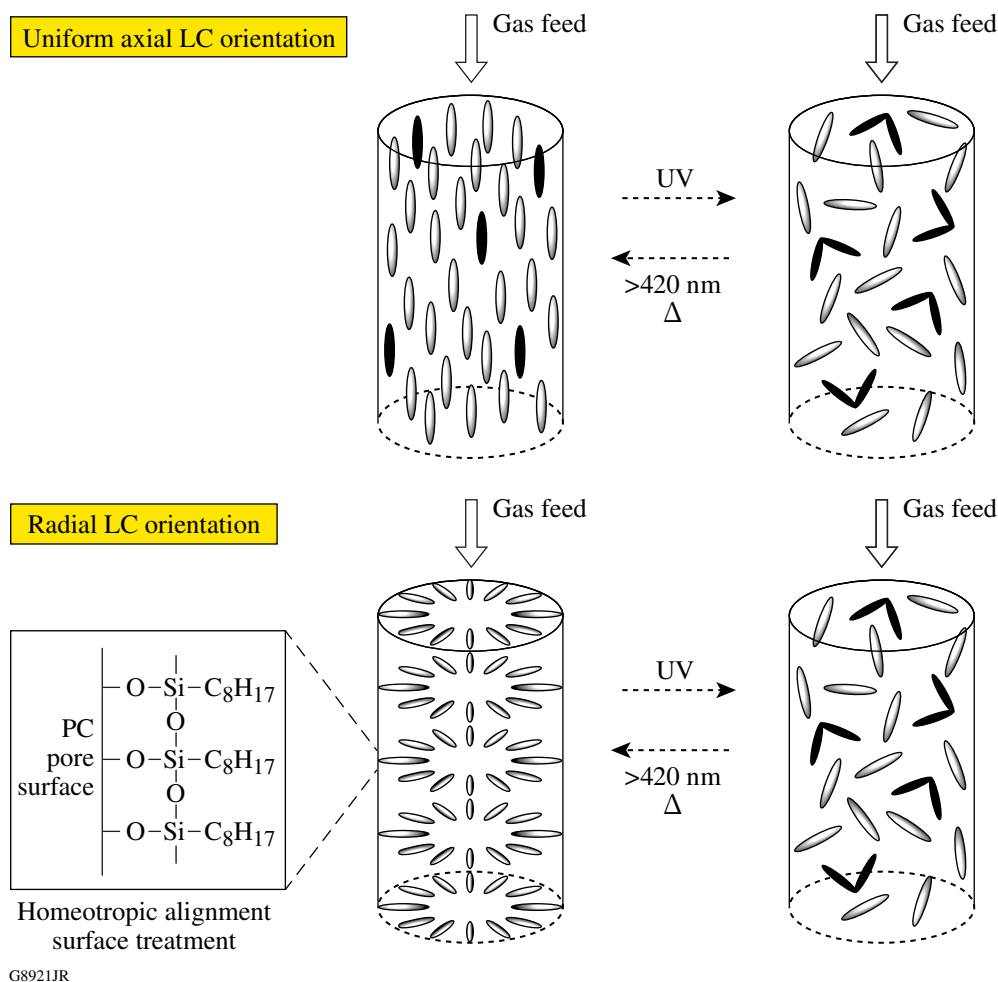


Figure 122.3

Photoswitchable operation of LC/mesogenic dye confined in track-etched pores based on reversible nematic–isotropic phase changes. Both homogeneous and homeotropic (radial) alignments with respect to the confining pore wall are evaluated in this article.

confined LC material will often heavily plasticize the polymer host, producing membranes without the necessary mechanical robustness. The PDLC's reported by Kajiyama overcame this difficulty by using a large thickness (several hundred microns), which precludes efficient photoactuation through the depth of the film because of the high extinction coefficient of azobenzene in the LC mixture. Although we successfully fabricated poly(vinyl chloride) (PVC)-based freestanding membranes that were only a few microns thick, they proved to be insufficiently mechanically robust and were ruptured by pressures >1 psi. Attempts to improve the membrane strength by using poly(methyl methacrylate) (PMMA) crosslinked with ethylene glycol dimethacrylate as the host polymer produced membranes that were extremely mechanically robust. The LC, however, still plasticized the host, resulting in membranes that stretched and "ballooned out" under pressure, but did not break because of the strength of the crosslinked PMMA. Based on these results, it became immediately apparent that, even with a great deal of additional materials research activities, freestanding PDLC membranes would not be practical candidates for photocontrolled membranes in the short term.

2. Photocontrollable Track-Etched Membranes with Imbided LC Material

a. Photoswitching and kinetics. The relatively thin membrane cross section of the photoswitchable LC-imbided Isopore polycarbonate membranes ($\approx 10 \mu\text{m}$), along with their high transparency in the long-wavelength-range UV, makes revers-

ible photoswitching possible by irradiation through alternating bandpass filters (365 nm or 420 nm).

To demonstrate that photoisomerization was indeed solely responsible for the observed phase changes, UV-Vis spectra were obtained for Isopore films imbided with Eutectic 1 and Eutectic 2 both before and after irradiation under the same conditions (Fig. 122.4). Ten seconds of irradiation time (which corresponds to a fluence of $2 \text{ mW}/\text{cm}^2$) is sufficient to nearly eliminate the absorbance band from the *trans* isomer at $\approx 360 \text{ nm}$. The accompanying rise of absorption at 420 nm from the photogenerated *cis* isomer appears as a small peak because of the low molar extinction coefficient of the *cis* isomer relative to the *trans* isomer. The 360-nm peak that appears as a shoulder in the spectrum of the Eutectic 1-imbided membranes is due to the absorbance of the cyanobiphenyl components of the E7 host LC. Irradiation with light >420 nm regenerates the *trans* form and affords the complete return to the original pre-irradiation spectrum for both eutectic mixtures. As is well known from PDLC research, the refractive-index mismatch between micrometer-sized nematic droplets and the polymer host results in a highly scattering film,¹⁰ and this refractive-index mismatch can be changed by inducing the LC material to undergo a phase change to the isotropic state either thermally or photochemically. In the case of an LC host containing azobenzene dyes imbided in a porous polycarbonate membrane, a similar photochemically induced phase change can be expected. The inset in Fig. 122.4 shows an image viewed through a stack of

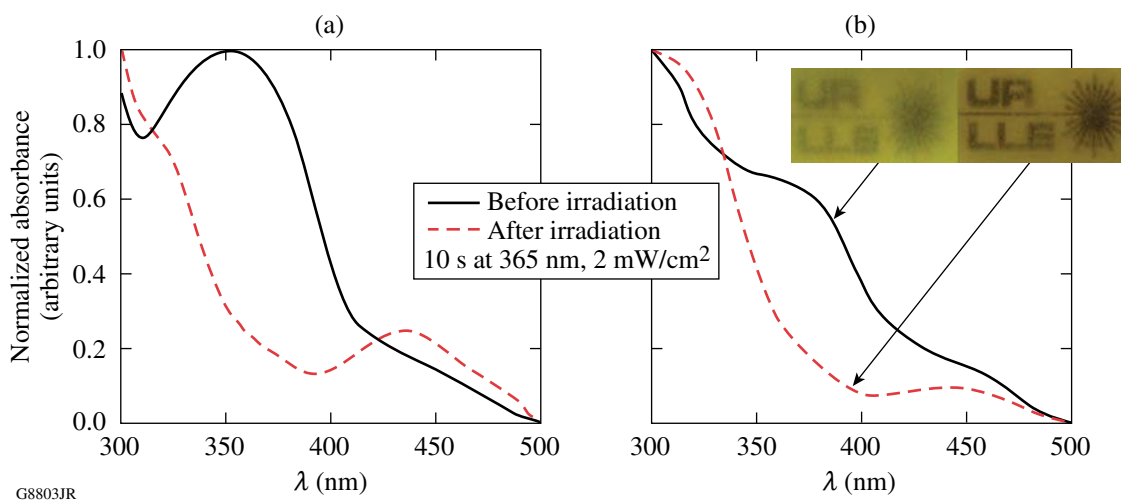


Figure 122.4

UV-Vis spectra of imbedded Isopore membranes before and after irradiation with UV light. Plot (a) shows Eutectic 2, plot (b) Eutectic 1. The inset in the upper right shows three stacked Eutectic 1-imbided membranes before and after irradiation, demonstrating the narrowing of refractive-index mismatch between host polycarbonate and confined Eutectic 1.

three photoswitchable LC-imbibed polycarbonate membranes containing Eutectic 1 (total path length = 30 μm) before and after irradiation with 365-nm UV. Although the contrast ratio between irradiated and non-irradiated membranes was relatively low because of the small LC domain size (400-nm LC-containing pores) in these membranes, they nevertheless clearly demonstrate that an LC-to-isotropic phase change is indeed occurring under the selected irradiation conditions. The isothermal nematic–isotropic phase changes were also verified by polarized optical microscopy (POM) (see **Dispersion State of Imbibed LC Materials** below).

The kinetics of thermal relaxation of the azobenzene dyes from the photogenerated *cis* state back to the original *trans* state in the confined environment are a parameter of interest. After irradiating a membrane for 10 s at 2 mW/cm^2 , the change in absorbance (A_t/A_0) at 365 nm was monitored as a function of time. The recovery of the *trans* isomer π - π^* absorption band with time obeys first-order kinetics for azobenzene dyes dissolved in solution. Azobenzene chromophores in the solid state, such as in thin films, are known to follow a more-complex behavior. This behavior is due to the fact that steric effects of the host environment on the azo dye affect the thermodynamics of thermal *cis*-*trans* isomerization. Figure 122.5 shows a logarithmic plot of A_t/A_0 as a function of time. The steep initial rise in the curve followed by a more-gradual leveling off and linear behavior is attributed to a first-order process with two rate constants, with the greater rate constant corresponding to azobenzene *cis* isomers that are in a more-strained environment. Because of the alignment effect of the confining surface,¹¹ we hypothesize that azobenzene mesogens close to the pore wall isomerize faster than those in the bulk. We found that the thermal relaxation of confined azobenzene mesogens resembled that of azobenzenes in the solid state¹¹ and could be modeled using the biexponential expression

$$[\text{trans}]_t/[\text{trans}]_0 = \alpha \exp[-k_1 t] + (1 - \alpha) \exp[-k_2 t]. \quad (1)$$

The calculated rate constants are an order of magnitude greater than typical azobenzenes in solution in an isotropic solvent.¹² The OTS-aligned Eutectic 1 proved to be anomalous to the other confined materials in that photoinduced isomerization occurred more slowly, and only after 10 min in the dark did the *cis*-isomer population begin to decline. We are currently conducting experiments to explain this observation.

b. Dispersion state of imbibed LC materials. Understanding the ordering of mesogenic molecules in the porous membrane structure is requisite to interpreting the permeation character-

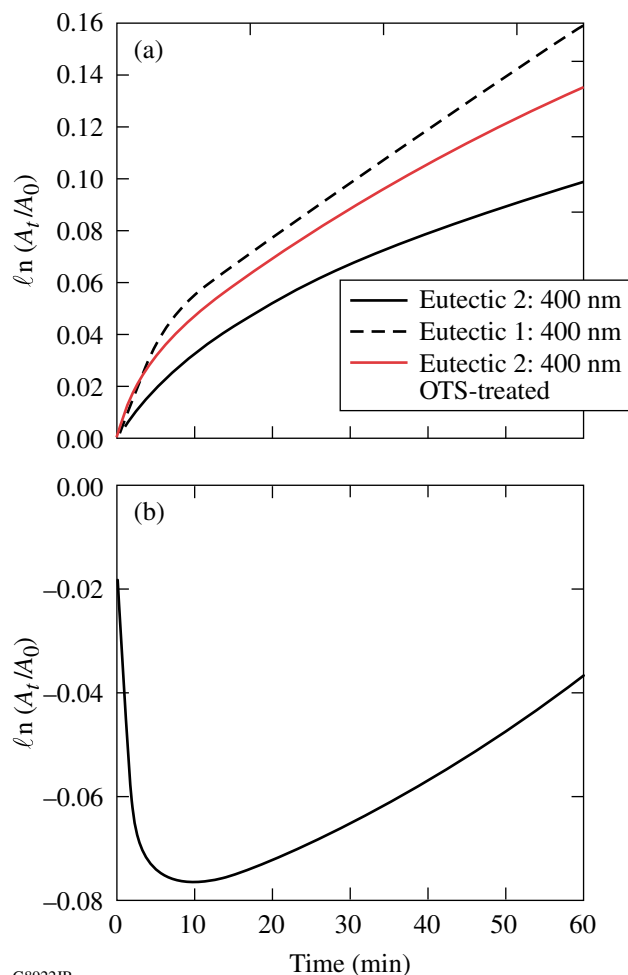


Figure 122.5 Normalized absorbance (A_t/A_0) over time for the two eutectic mixtures at 360 nm following 10 s of irradiation (2 mW/cm^2). Measurements were taken in the dark over 1 h, every 10 s. (a) Unaligned Eutectic 1: $k_1 = 0.72 \times 10^{-2} \text{ min}^{-1}$, $k_2 = 0.20 \times 10^{-2} \text{ min}^{-1}$. Eutectic 2: $k_1 = 0.61 \times 10^{-2} \text{ min}^{-1}$, $k_2 = 0.19 \times 10^{-2} \text{ min}^{-1}$. OTS-aligned Eutectic 2: $k_1 = 0.73 \times 10^{-2} \text{ min}^{-1}$, $k_2 = 0.20 \times 10^{-2} \text{ min}^{-1}$. Graph (b) shows the anomalous behavior of OTS-aligned Eutectic 1 in 400-nm pores.

istics of such materials. We evaluated the nematic range of the eutectic materials both in the bulk state and imbibed into the pores using both POM and differential scanning calorimetry (DSC). For DSC evaluation, the membranes were carefully chopped into pieces and then packed into a DSC pan for measurement. Although the quantity of mesogenic material in the pores was very small, definite phase-transition endotherms were visible with good signal-to-noise ratio at scan rates $\geq 40^\circ\text{C}/\text{min}$ on both heating and cooling. Repeated cycling produced no noticeable changes in the DSC thermograms for all samples evaluated. Thermograms for the eutectic materials in both the free-bulk and confined geometries were normalized to bal-

ance out the large disparity in sample quantity. Figure 122.6 compares the nematic–isotropic phase-transition temperatures for the two photoswitchable eutectic mixtures in the free-bulk versus the confined environment of the membrane pores, with and without treatment with OTS. For Eutectic 1 (biphenyl host), the nematic–isotropic transition temperature T_{cl} decreased only slightly in the confined state, while in Eutectic 2 (phenylbenzoate host) T_{cl} increased relative to the bulk material, which indicates the confined environment increases the LC bulk order and stabilizes the LC phase. For the biphenyl host (Eutectic 1), the observed reduction in T_{cl} may be caused by extraction of trace unreacted monomers from the porous polycarbonate membrane since biphenyl materials such as E7 are well known to plasticize many different polymer systems. Studies of E7 (Ref. 13) and other cyanobiphenyl LC materials¹² in PDLC's have also shown very small drops in T_{cl} of dispersed nematic droplets. OTS treatment increased the T_{cl} for both confined eutectics, suggesting the effectiveness of this treatment in supporting LC alignment.

Direct observation by POM of the texture of the LC photo-switchable host confined in the 400-nm pores of the Isopore membrane was not possible because of (1) the regions of highly crystalline polycarbonate domains of the order of several microns that extensively scatter light in the membrane and (2) the high birefringence of the membrane imparted by the

extrusion process used in its fabrication. For Isopore membranes with 10- μm pores, we were able to easily image the LC orientation in the pores by keeping the optical axis of the film fixed so that it was always aligned parallel to the incident polarizer. Rotating the analyzer so that it was oriented either parallel or perpendicular to the incident polarizer allowed one to see the confined LC at 1000 \times total magnification using combinations of transmitted and reflective illumination. Prior to imaging the membrane, any remaining traces of free LC material were removed from the surface by spinning the membranes at 3000 rpm and washing with several drops of hexane. Figure 122.7 shows a series of photomicrographs of the two photoswitchable LC eutectics imbibed into 10- μm pores of Isopore membranes. When viewed under crossed polarizers in reflection and transmission, the pores appeared as brighter areas while the surrounding polymer matrix appeared dark. The smeared birefringent areas around some of the pores are most likely caused by leaching of the LC eutectic into defect voids that extend laterally out from any pore walls that have been over-etched during membrane manufacture. Viewing under crossed polarizers with both transmitted and reflected illumination while rotating the sample stage establishes that the LC molecules are uniaxially arranged in the 10- μm pores and parallel to the pore axis. These findings are consistent with the ²H NMR studies of Crawford *et al.*¹¹ for nematogens in Isopore membrane pores, as well as for inorganic porous photonic

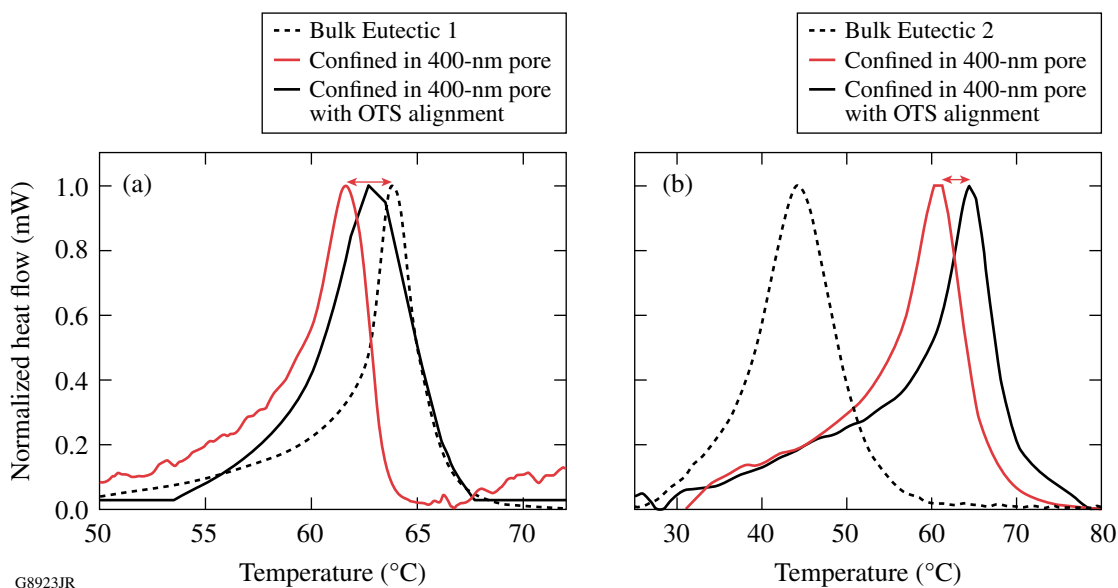


Figure 122.6

DSC heating scans for (a) Eutectic 1 and (b) Eutectic 2. Note that the signals are normalized to compensate for large disparity in sample quantity.

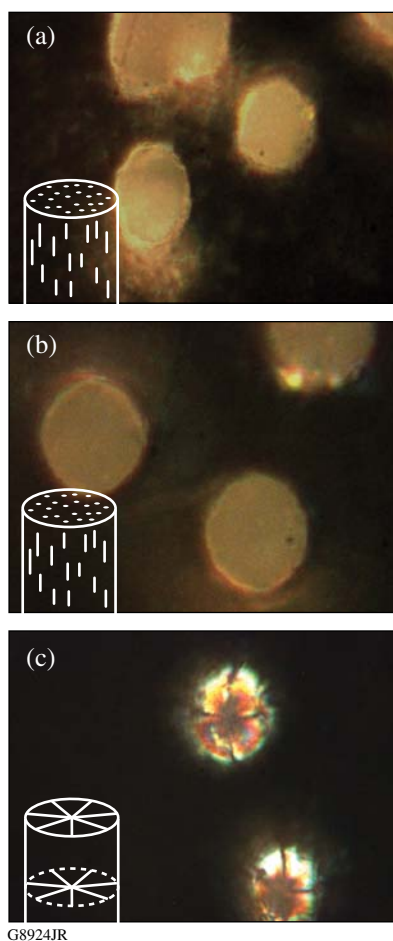


Figure 122.7
POM images of LC material confined in 10- μm pores. (a) Eutectic 1 without alignment, (b) Eutectic 2 without alignment, and (c) Eutectic 1 in a pore treated with 2% OTS solution. The inset drawings illustrate the orientation of the nematic director fields.

crystals (200- to 600-nm pores) imbibed with LC materials.¹⁴ Membranes treated with OTS demonstrated the Maltese-cross optical texture that is characteristic of radial alignment.

c. Permeation properties. Permeation tests are carried out using a traditional volume/time method to determine the steady-state permeation coefficient P (Ref. 15). The coefficient P is defined as the Fickian flux (J) times the value of membrane thickness (l) divided by the pressure difference (Δp) across the membrane, where the flux J equals the concentration gradient (concentration ϕ divided by length x) multiplied by a diffusion coefficient D :

$$J = -D \frac{d\phi}{dx} \quad (2)$$

$$P = \frac{J \cdot l}{\Delta p}. \quad (3)$$

After the membranes equilibrate at a given pressure, the volume of nitrogen diffused over time is measured. The membrane is then irradiated with 365-nm light for 5 s (2 mW/cm^2) to switch it into the isotropic state and subsequently reach equilibrium, after which the permeability is re-measured. Irradiation is then conducted using $>420 \text{ nm}$ for the same time and intensity as the UV irradiation to photoswitch the membrane back to the LC state. This test cycle is repeated to check for reversibility, which we define as four cycles between the alternately photogenerated states without measurable deviations from steady-state permeation behavior of the respective states. From our initial tests, a clear relationship emerged between confining pore size and the capacity to withstand incident pressure. Membranes with larger pores do not display sufficient stability with respect to sustained irradiation–permeation cycles. Neither 5- μm nor 10- μm pore sizes provided sufficient confinement strength to retain the LC eutectics in the pores. We did find that 400-nm pores perform very well over consecutive test cycles. Imbibed 400-nm pore membranes were 6 to 7 orders of magnitude less permeable than empty membranes. When filled with LC eutectics, they exhibited permeability of the same range as highly permeable rubbery polymeric materials, such as poly(dimethyl siloxane).¹ Both LC materials display good reversibility below 500 mmHg. Figure 122.8 shows permeability versus pressure (P/p) data for Isopore membranes with 400-nm pores imbibed with both Eutectic 1 and Eutectic 2. Both materials appear to follow ideal linear P/p behavior in both the LC and the isotropic states.

The isotropic state provides greatly increased permeation in photoswitched imbibed Eutectic 1. Treatment with OTS slightly lowers the permeability of the photogenerated isotropic state, although that of the LC state is unchanged. We conclude that uniaxial versus radial alignment has no effect on the permeability of Eutectic 1. In the case of Eutectic 2, the photogenerated isotropic state is less permeable than the initial LC state, and overall permeability values are an order of magnitude lower than Eutectic 1. The effect of the OTS alignment is significantly more pronounced. The increased T_{cl} shown by DSC and the faster *cis-trans* thermal isomerization suggest that enhanced LC ordering is responsible for lower permeation. Eutectic 1 shows permeation overall an order of magnitude greater than Eutectic 2, for both LC and isotropic states, with or without OTS treatment. This finding leads us to conclude that the intrinsic sorption–diffusion–desorption properties (with respect to nitrogen) of the imbibed material are what change upon photoirradiation. Increasing the permeation difference

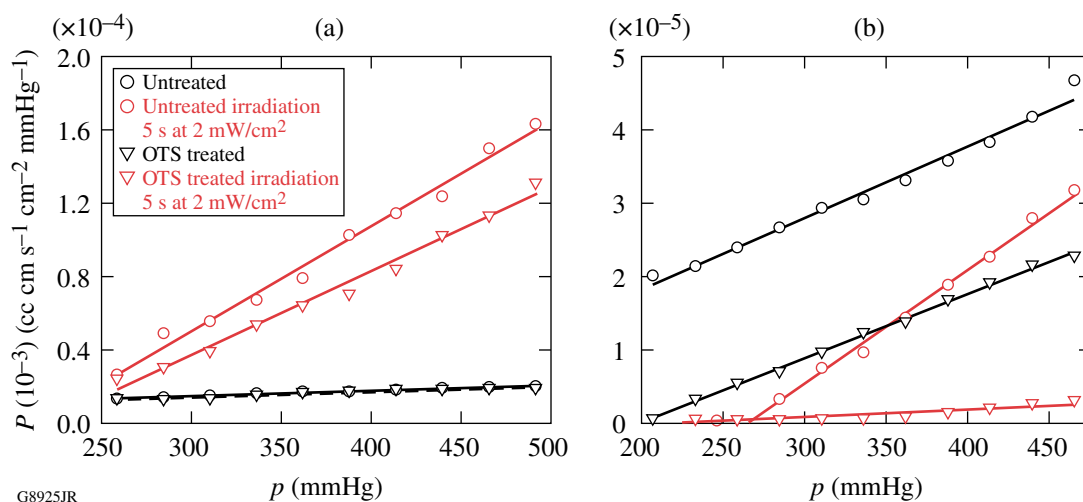


Figure 122.8

Permeability/pressure relationships for imbibed LC materials in 400-nm pores: (a) Eutectic 1 and (b) Eutectic 2. Photoswitching causes a reversible change in the permeation coefficient P .

between photogenerated states and achieving potential tunable selectivity are the subjects of our ongoing investigations.

Conclusions

The results of this effort have shown that photoswitchable LC materials based on azobenzene derivatives as the active element have potential for application to reversible photocontrollable gas permeation membranes. The imbibed mesogenic materials offer several tunable variables based on exploiting LC composition and alignment effects. For all imbibed materials, linear sorption–diffusion behavior was observed. Isothermal permeability switching response times between the LC and isotropic state of 5 s were demonstrated at an intensity of 2 mW/cm² using alternating UV and >420-nm radiation. Our goal now is to increase the overall differences in permeability that can be achieved through photoswitching, as well as explore possibilities for tunable selective permeation. These goals lead us to focus on exploiting the multitude of LC phases that are regularly used for various electro-optical applications (smectic phases, chiral phases, etc.). These materials potentially offer many types of tunable-ordered media that can be applied to separation technology and gateable interconnects in “smart” photocontrollable membranes.

Experimental

1. Preparation of Photoswitchable LC Mixtures

Photoswitchable eutectic mixtures were prepared by adding an azobenzene LC material to an existing eutectic LC mixture and mixing above the isotropic temperature of the

mixture. The phase transition of the mixtures was verified by hot-stage polarizing microscopy (POM). The composition of the two mixtures studied is given in Fig. 122.2. Eutectic 1 was prepared by doping 14% w/w of the azobenzene 4-butyl-4'-methoxyazobenzene (BMAB) into the biphenyl host Merck E7 at an elevated temperature. This azobenzene compound was synthesized, as previously reported.¹⁶ Eutectic 2 was prepared by doping 15% w/w of 4-ethoxy-4'-hexanoylazobenzene (EHAB) obtained from Eastman Chemical into a 60:40 w/w eutectic mixture of 4-pentylphenyl-4'-methoxybenzoate (PPMeOB) and 4-pentylphenyl-4'-pentoxybenzoate (PPPOB) at an elevated temperature. These two phenylbenzoate materials had been previously synthesized and purified in-house using well-known preparation and purification techniques.

2. Preparation of LC-Imbibed Track-Etched Membranes

Track-etched, 10- μ m-thick Isopore polycarbonate films (Millipore Corp.) with pore sizes of 0.4 μ m, 5 μ m, and 10 μ m were heated to 100°C in vacuum (200 mtorr) overnight to remove water and other volatile components. The membranes were imbibed with LC through capillary action by completely immersing them into the LC eutectic at a temperature above the LC isotropic transition (80°C) for 1 h. Excess LC on the surfaces of the membrane was removed by carefully rubbing the membranes between two sheets of filter paper. To achieve homeotropic alignment, reactive silane octyl triethoxysilane (OTS) was used. Membranes were immersed in a solution of 2-wt% OTS in ethanol with a few drops of acetic acid catalyst for 5 min, then dried in a vacuum oven. For POM imaging,

all residual LC material was removed from the surface by spinning the membranes at 3000 rpm and washing with a few drops of hexane. Photoswitching experiments were conducted using a Rolence Technologies Q-Lux handheld UV curing unit (365 nm at 70 mW/cm²). The output wavelength bandwidth was narrowed to 365 nm and 420 nm, as required, using optical bandpass filters (Edmund Optics).

3. Characterization

Differential scanning calorimetry (DSC) measurements were conducted using a Perkin-Elmer DSC 7 with a CCA-7 liquid nitrogen subambient accessory. The sample and reference compartments were purged with nitrogen at a flow rate of 20 ml/min. Optical spectroscopy (UV-VIS) was accomplished using a Perkin-Elmer Lambda 900 spectrophotometer, while visualization of the LC confined in the porous membrane structure was carried out using either a Leitz Orthoplan POL polarizing microscope or a Leica DMRX polarizing microscope at up to 1000× total magnification with reflected and transmitted illumination.

4. Permeability Measurements

The permeability of the photoswitchable LC membranes to nitrogen was measured according to the volume/time method using an apparatus that was constructed in-house. The membrane being tested was clamped between two rubber gaskets in an aluminum manifold and equilibrated with a given upstream pressure (200 to 500 mmHg). The permeation cell was designed in such a way that the membrane was irradiated directly. The permeation area was 0.5 cm².

ACKNOWLEDGMENT

This work was supported by the U.S. Department of Energy Office of Inertial Confinement Fusion under Cooperative Agreement No. DE-FC52-08NA28302, the University of Rochester, and the New York State Energy Research and Development Authority. The support of DOE does not constitute an endorsement by DOE of the views expressed in this article.

REFERENCES

1. D. R. Paul and Y. P. Yampol'skii, in *Polymeric Gas Separation Membranes*, edited by D. R. Paul and Y. P. Yampol'skii (CRC Press, Boca Raton, FL, 1994), Chap. 1, pp. 1–17.
2. M. Ulbricht, *Polymer* **47**, 2217 (2006).
3. T. Kajiyama, in *Polymers for Gas Separation*, edited by N. Toshima (VCH Publishers, New York, 1992), Chap. 3.
4. T. Kajiyama, A. Takahara, and H. Kikuchi, *Polym. J.* **23**, 347 (1991).
5. R. Dinarvand and M. Ansari, *J. Membr. Sci.* **223**, 217 (2003).
6. R. H. El Halabieh, O. Mermut, and C. J. Barrett, *Pure Appl. Chem.* **76**, 1445 (2004); C. J. Barrett *et al.*, *Soft Mat.* **3**, 1249 (2007); G. S. Kumar and D. C. Neckers, *Chem. Rev.* **89**, 1915 (1989).
7. H. Kurihara, A. Shishido, and T. Ikeda, *J. Appl. Phys.* **98**, 083510 (2005).
8. T. Ikeda and O. Tsutsumi, *Science* **268**, 1873 (1995).
9. G. P. Crawford *et al.*, *J. Chem. Phys.* **96**, 7788 (1992).
10. M. R. LaPointe and G. M. Sottile, in *Solar and Switching Materials*, edited by C. M. Lampert, C.-G. Granqvist, and K. L. Lewis (SPIE, Bellingham, WA, 2001), Vol. 4458, pp. 112–119.
11. I. Suzuki *et al.*, *Macromolecules* **35**, 577 (2002); I. Mancheva, I. Zhivakov, and S. Nespurek, *J. Optoelectron. Adv. M.* **7**, 253 (2005).
12. W. Ahn *et al.*, *Macromolecules* **25**, 5002 (1992).
13. S. R. Challa, S. Q. Wang, and J. L. Koenig, *J. Therm. Anal.* **45**, 1297 (1995).
14. P. El-Kallassi *et al.*, *J. Opt. Soc. Am. B* **24**, 2165 (2007).
15. D. W. Brubaker and K. Kammermeyer, *Anal. Chem.* **25**, 424 (1953).
16. E. Głowacki, K. L. Marshall, and C. W. Tang, in *Liquid Crystals XIII*, edited by I. C. Khoo (SPIE, Bellingham, WA, 2009), Vol. 7414, p. 74140H.

High-Intensity Laser–Plasma Interaction with Wedge-Shaped–Cavity Targets

Introduction

The interaction of intense, picosecond laser pulses with cone- and wedge-shaped–cavity targets is an important topic for applications such as fast ignition,¹ proton^{2,3} and electron⁴ acceleration, x-ray generation,⁵ and isochoric heating⁶ of solid matter. The primary coupling mechanism of high-intensity laser pulses ($\geq 10^{18}$ W/cm²) interacting with solids is the acceleration of electrons to kinetic energies of up to several MeV. A significant portion of the laser energy is converted into these suprathermal electrons. Maximizing this conversion efficiency for the various applications is a major challenge.

A number of factors that affect the conversion efficiency include the laser contrast (which is defined as the ratio of peak power to the power of a pedestal at a certain time before the main pulse), the laser polarization, and the target geometry. Several studies have shown that a high contrast ratio is critically important for cone-in-shell fast ignition.^{7–9} A better coupling efficiency has been demonstrated with second-harmonic irradiation of microcones.¹⁰ It has also been shown that pre-plasma formation in the hollow cone substantially affects the conversion process.^{8,9} Large-scale-length plasmas inside the cone significantly influence the relativistic laser–plasma interaction, the laser-energy deposition, and the generation and transport of hot electrons toward the compressed fuel core.¹¹

The coupling efficiency in wedge and cone targets is not completely understood, and more studies are required to fully quantify how the shape of the target affects the fast-electron production for the various applications. Particle-in-cell (PIC) simulations by Nakamura *et al.*³ predicted that higher-energy fast electrons and protons would be produced using cones having a narrower (30°) cone angle and irradiated with a laser intensity of $\sim 10^{19}$ W/cm². The simulations predict that laser energy is more efficiently absorbed and funneled into the tip of the cone through surface-field effects. Similar studies were performed by Lasinski *et al.* with 2-D PIC simulations for fast-ignition targets.¹² The cone geometry was studied to maximize the laser energy that is absorbed into fast electrons and to optimize the conditions for achieving a collimated fast-

electron beam at the tip. Other theoretical studies predict some benefit of using cone-shaped targets over flat foils in terms of increased laser absorption and enhanced energy transfer into fast electrons¹³ and surface-guided fast electrons into the cone tip.¹⁴

This article presents experimental studies of fast-electron generation in hollow wedge-shaped–cavity targets, which consist of two square copper metal foils that are seamlessly joined together at one side to form a cavity. A laser beam with a contrast ratio higher than 10^8 was focused into the cavity to the target’s corner with intensities of $\sim 1 \times 10^{19}$ W/cm² using either *s*- or *p*-polarization irradiation.^{15,16} The small-mass targets were in the refluxing regime,¹⁷ meaning that strong Debye sheath fields were created at the target boundaries that confined the majority of the fast electrons in the target.¹⁸ This made it possible to infer the laser-to-fast-electron conversion efficiency by measuring the absolute K_{α} -line emission produced in the target.¹⁹ The following sections describe the targets and the experimental setup; present and analyze the experimental results; discuss the results and compare them to 2-D PIC simulations; and present conclusions of this work.

Targets and Experimental Setup

General Atomics fabricated the targets by micromachining small wedges from ~ 100 - μm -wide aluminum (Al) bars to form an extremely sharp edge (edge radius of curvature of less than ~ 1 μm); the bars were electroplated with a thin (~ 20 - μm) Cu layer on both sides and cut into separate pieces. The inner Al material was etched away, leaving hollow Cu wedges comprising two ~ 100 - μm squares of ~ 20 - μm thickness joined seamlessly together. Figure 122.9 shows photos of (a) 30°- and (b) 45°-opening-angle wedges mounted on a target stalk.

Targets with 30°, 45°, and 60° full opening angles were fabricated. The laser propagated along the *y* direction (see Fig. 122.9 for the definition of the coordinate system) into the cavity with its focal plane located at the inside wedge seam. The inside corner radius was estimated to be ~ 1 μm , smaller than the focal-spot diameter of ~ 5 μm . The wedge-shaped–cavity

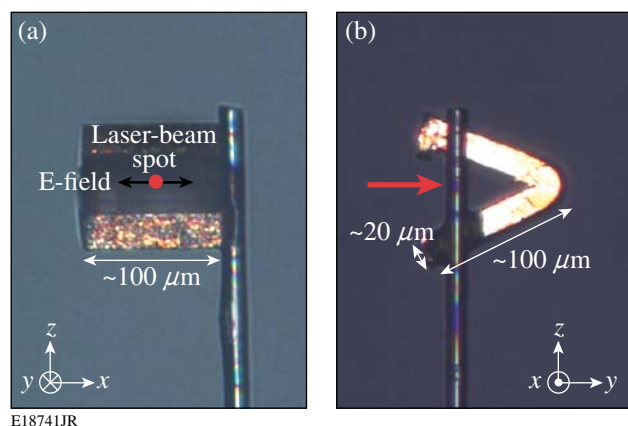


Figure 122.9

(a) A mounted 30°-opening-angle wedge looking along the laser propagation direction and (b) a mounted 45°-opening-angle wedge orthogonal to the laser propagation direction. Both targets were mounted for *s*-polarization irradiation.

targets' orientation set the laser polarization with respect to the target surface. With the electric field vector of the laser beam along the *x* direction, both targets in Fig. 122.9 were mounted for *s*-polarization irradiation. Rotating the target by 90° around the laser axis made it possible to investigate the interaction with a *p*-polarized beam. The targets were mounted onto 17- μm -diam SiC fibers. The accuracy of the target mounting with respect to beam polarization was estimated to be 5°. The targets were aligned with a precision of $\sim 5 \mu\text{m}$ and $\sim 2^\circ$ with a target-positioning station comprising three translational and one rotational axes; a target-viewing system made two orthogonal views of the target possible. Approximately 40 targets were used in this campaign with about half for each polarization.

The Multi-Terawatt (MTW) Laser System consists of an optical parametric chirped-pulse amplification (OPCPA) front end,¹⁵ which delivered pulses with $\sim 250\text{-mJ}$ energy and 0.5-ps duration at $\lambda = 1.053 \mu\text{m}$; these pulses were subsequently amplified in a Nd:glass amplifier chain up to 10 J (Ref. 20). For this experiment, pulse energies of around 5 J with 1-ps duration were used. The beam was focused with an off-axis parabolic mirror with an effective *f* number of ~ 4 to a nearly diffraction limited spot of $\sim 5\text{-}\mu\text{m}$ diameter, defined by the full width at half maximum (FWHM) of a peak intensity of $\sim 1 \times 10^{19} \text{ W/cm}^2$. The high temporal contrast was measured with a scanning third-order cross correlator. The ratio of the peak power to the power of a pedestal 100 ps before the main pulse was $>10^8$ (Ref. 16).

Laser-produced fast electrons generated an 8-keV line emission by knocking out K-shell electrons. Both x rays and

energetic electrons may produce inner-shell vacancies, assuming that the radiation has sufficient energy to excite above the K edge (for Cu, $h\nu > 9 \text{ keV}$), but energetic electrons are the main contributors to K_{α} and K_{β} production in a high-intensity, ultrashort, laser–solid interaction with low- and mid-*Z* materials.²¹ Three different single-shot x-ray diagnostics measured the 8-keV K_{α} fluorescence emission from the Cu targets. A single-photon-counting x-ray spectrograph (XCCD),²² a crystal spectrograph equipped with two highly oriented pyrolytic graphite (HOPG) crystals, and a crystal imager (IMAGER)²³ were used. The IMAGER was a spherically curved α -quartz (2131) crystal with a 38-cm bending radius that imaged the $\text{K}_{\alpha 1}$ emission in a narrow spectral bandwidth of $E/\Delta E = 1340$ and $8.57\times$ magnification onto a front-illuminated, 16-bit charge-coupled-device (CCD) camera.²⁴ A 13.5- μm , 1024 \times 1024-pixel chip provided a field of view of $\sim 1.6 \text{ mm} \times 1.6 \text{ mm}$. A 1.6-cm-diam aperture in front of the crystal reduced the astigmatism, resulting in a spatial resolution of $\sim 15 \mu\text{m}$. A thin, 35- μm Cu foil was mounted in front of the CCD camera to block stray laser light and provide bandpass filtering in the x-ray range from 8 to 9 keV. Additional lead apertures were introduced in the beam path to block the direct line of sight.

The HOPG consisted of two grade-ZYA (low-mosaic-spread) crystals,²⁵ 10 mm \times 50 mm and 2-mm thickness mounted 49 cm away from the target. The crystals covered photon-energy ranges of ~ 7.7 to $\sim 8.7 \text{ keV}$ and ~ 8.2 to $\sim 9.2 \text{ keV}$, respectively. A 16-bit, back-illuminated SI-800 CCD²⁴ with 2048 \times 2048, 13.5- μm -wide pixels was mounted 49 cm from the crystals to use mosaic focusing for best spectral resolution.²⁶ A spectral resolution of $E/\Delta E \approx 700$ was sufficient to resolve the $\text{K}_{\alpha 1}$ (8048-eV) and $\text{K}_{\alpha 2}$ (8028-eV) transitions. The integrated reflectivity of the HOPG crystal dispersing the K_{α} signal was measured with $2.82 \pm 0.1 \text{ mrad}$ at two different locations on the crystal. A 10- μm Cu foil filter mounted in front of the HOPG crystal blocked visible and soft x-ray radiation from the target while providing $>60\%$ transmission in the region of interest. Both the HOPG crystal and the XCCD used SI-800 CCD models equipped with back-illuminated chips from e2v Technologies,²⁷ comprising a 16- μm -thick depletion layer.²⁸ The XCCD's spectral resolution of $E/\Delta E \approx 45$ at 8 keV was insufficient to resolve the fine transitions. An absolute calibration was performed in Ref. 28 for single-photon-counting applications of the same camera model and chip used in this experiment. Assuming this calibration for the XCCD, an efficiency of $3.1 \pm 0.5\%$ was inferred for 8-keV x-ray photons when using the standard histogram analysis method.²⁸ This is lower than the $5 \pm 2.5\%$ that was previously measured for that camera model, but it is still in agreement with the recent calibration

within the measurement uncertainties.^{22,29} The current calibration error of the XCCD was $\sim 20\%$. An absolute calibration of the HOPG was obtained by taking into account the quantum efficiency of a $16\text{-}\mu\text{m}$ -thick Si slab at $\sim 8\text{ keV}$, the measured crystal reflectivity, the dispersion curve, and the transmission of the $10\text{-}\mu\text{m}$ Cu foil in front of the spectrograph. The HOPG calibration error was $\sim 10\%$.

The simultaneously operating diagnostics had different viewing directions: the azimuthal (θ) and polar (ϕ) diagnostic angles were $\theta = 135.0^\circ, 90.0^\circ, 62.4^\circ$ and $\phi = 0^\circ, 355.0^\circ, 59.7^\circ$ for the IMAGER, HOPG, and XCCD, with respect to the coordinate system shown in Fig. 122.9 with the polar axis along the z direction and the laser propagation along the y direction.

Experimental Results and Analysis

Figure 122.10 shows a spatially resolved K_α image of a 60° wedge. A nearly homogeneous emission was observed over the target although the laser interacted with only a small target region in the seam. The measurement indicated that the laser-generated fast electrons homogeneously filled the target. Only a small percentage of the fast electrons were energetic enough to escape the target. The resulting net charge set up strong electrostatic sheath fields at the target boundaries. Most of the fast electrons were confined in the target and were reflected back into the target upon reaching the boundary. The refluxing fast electrons eventually filled the target, provided that their mean-

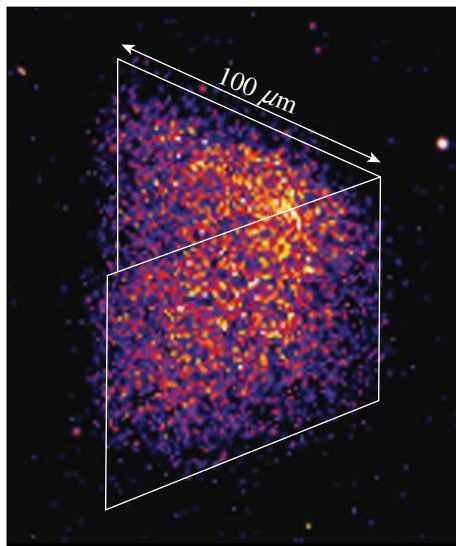


Figure 122.10 X-ray image of an s -polarized 60° -opening-angle wedge target (shot 2117). A nearly spatially homogenous 8-keV x-ray emission was observed. The pre-shot target boundaries are indicated by white lines for comparison.

free-path length was about the same as the target dimension or larger. The electron range in Cu is ~ 1 to $\sim 700\ \mu\text{m}$ for energies between 10 keV to 1 MeV (Ref. 30). Since fast electrons generate most of the K_α emission, this explains the observation of a spatially homogeneous fluorescence emission. Similar x-ray images were recorded with flat-foil targets.

Figure 122.11 shows measured x-ray spectra from (a) XCCD and (b) HOPG. The HOPG spectral resolution was high enough to resolve the $K_{\alpha 1}$ and $K_{\alpha 2}$ lines and the K_β line. Spectral integration yielded 4.38×10^{12} and 5.10×10^{11} photons into 4π steradians for K_α and K_β , respectively, for the XCCD spectrum. The HOPG spectrum yielded 4.39×10^{12} and 5.26×10^{11} photons for K_α and K_β . Both detectors were in very good agreement with respect to the total number of detected K_α and K_β photons.

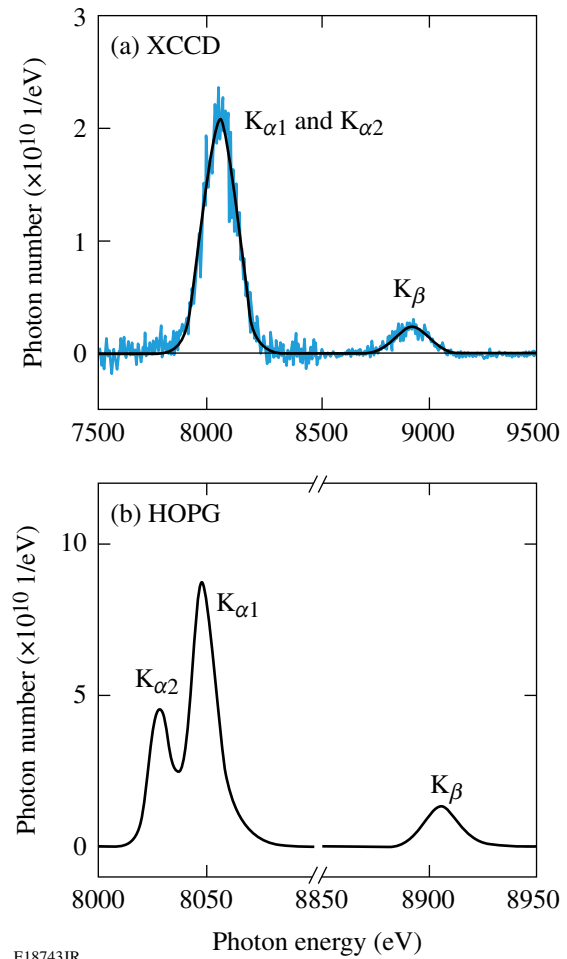


Figure 122.11 Measured x-ray spectra from XCCD (a) and HOPG (b) from a 30° -wedge target irradiated with p -polarization (shot 2164). HOPG resolved the $K_{\alpha 1}$ and $K_{\alpha 2}$ lines because of a higher spectral resolution. The abscissa is broken in (b) to show the K_α and K_β lines with reasonable resolution.

The diagnostics measured the x-ray emission from different angles with respect to the target. The line emission generated in deeper layers of the target was affected by reabsorption. This was taken into account by calculating the opacity effect for each diagnostic depending on the diagnostic view angle. The $1/e$ absorption lengths³¹ of K_α and K_β photons were $22.2 \mu\text{m}$ and $29.7 \mu\text{m}$, respectively, for the solid-state Cu material, and there was a significant direction-dependent reabsorption of that emission in the $\sim 100 \times 100 \times 40\text{-}\mu\text{m}^3$ target volume. The opacity was taken into account by describing the wedges as two rectangular prisms. $N = 2.7 \times 10^4$ grid points were placed in each prism. The average transmitted radiation

$$1/N \sum_{i=1}^N \exp(-\alpha_x d_i)$$

was calculated, where α_x was the corresponding absorption length and d_i was the distance that the radiation had to propagate through the target into the solid angle of the diagnostic. The distances depend on each grid point, the target orientation, and the diagnostic angle. The average emission from each prism was calculated, and the total emission was calculated by taking into account the partial obscuration of the radiation of one prism by the other.

Five to six laser shots were performed for each target species and polarization, and the average K_α signal was calculated. Figure 122.12 shows the measured K_α signal normalized to the laser energy as a function of the wedge angle for the different diagnostics. All three diagnostics were in good agree-

ment, showing that the Cu K_α emission was isotropic within the probed line of sights and the measurement accuracy. The open symbols represent the HOPG measurement while the solid symbols show the XCCD yields in Fig. 122.12(a) and the IMAGER yields in Fig. 122.12(b). The error bars indicate the statistical error of each measurement. The HOPG and XCCD diagnostics were absolutely calibrated, while the IMAGER was cross calibrated against the HOPG diagnostic. The data point at 180° marks the reference measurement with flat foils irradiated under normal incidence. The measured average yield of ~ 20 planar-foil targets of about the same mass was $(7.07 \pm 0.3) \times 10^{-4}$ (XCCD) and $(7.14 \pm 0.5) \times 10^{-4}$ (HOPG). The yield was a factor of 2 higher for the wedges reaching $(1.38 \pm 0.10) \times 10^{-3}$ (XCCD) and $(1.34 \pm 0.09) \times 10^{-3}$ (HOPG) for p -polarization. The data may indicate a slight increase in signal for smaller wedge angles.

Using targets that were in the refluxing regime made it possible to infer the fast-electron coupling efficiency (CE) from an absolute measurement of the K_α emission.^{18,19,22} Reference 18 describes the model that was used to infer CE from the K_α yield. The data from the three diagnostics were averaged and used to infer CE using a fixed laser intensity of $1 \times 10^{19} \text{ W/cm}^2$. The Cu inner-shell line emission depended weakly on the laser intensity in the range of 1×10^{18} to 10^{20} W/cm^2 (Refs. 19 and 22), so that intensity variations were not significant. Figure 122.13(a) shows the experimental CE for the wedge-shaped-cavity targets and for flat foils. The square symbols refer to p -polarization and the triangles show the efficiency of s -polarization. A p -polarized laser beam interacting with a narrow cavity converted significantly more short-pulse

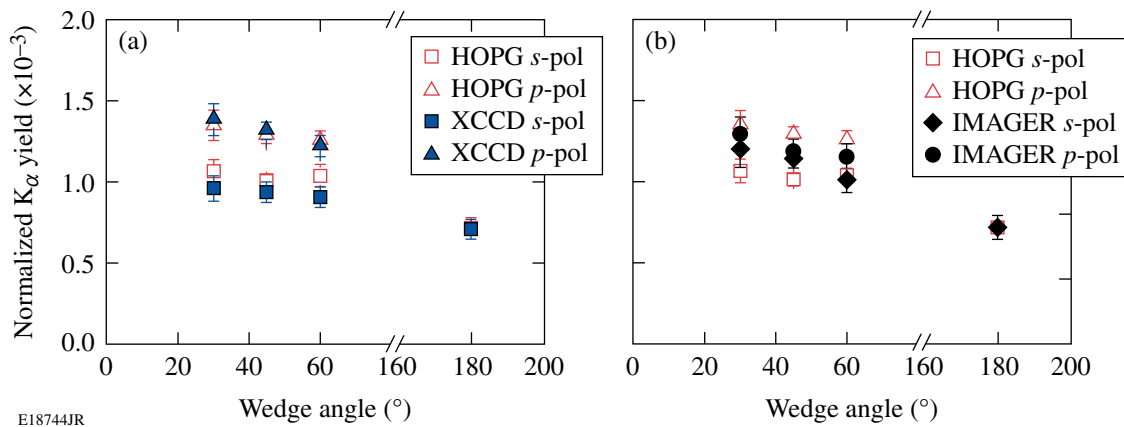


Figure 122.12 Measured K_α yield normalized to the laser energy on target from different diagnostics: (a) HOPG (open) and XCCD (solid) and (b) HOPG (open) and IMAGER (solid).

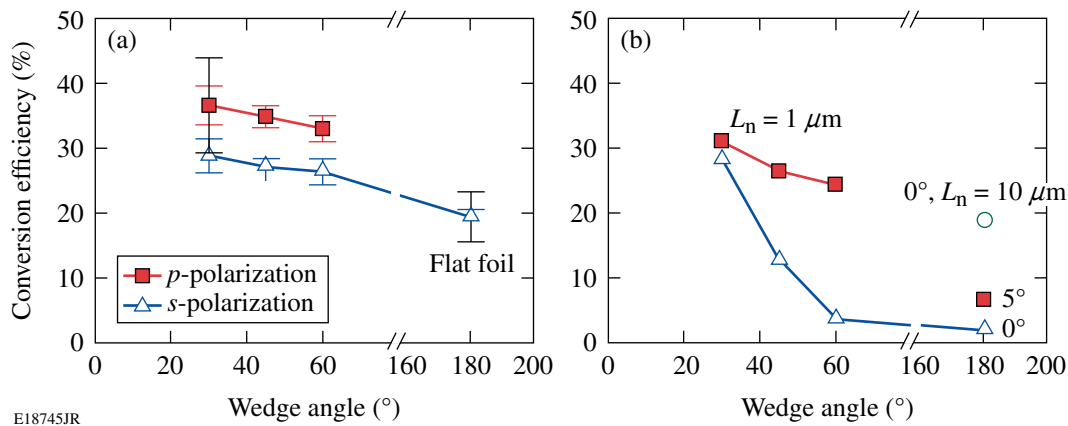


Figure 122.13

(a) Experimental and (b) theoretical conversion efficiency of short-pulse laser energy into fast electrons. The two error bars at 30° and 180° in (a) are representative absolute error bars of the measured conversion efficiency. The green circle in (b) represents a planar target with an overall target tilt of 5° relative to the beam axis. The red square at 180° in (b) was calculated using $L_n = 10 \mu\text{m}$, rather than $1 \mu\text{m}$.

energy (up to ~36%) into fast electrons than a flat foil of similar mass (20%). The absolute uncertainty of the conversion efficiency, ΔCE , was estimated at 20% relative to the CE, which gave an absolute ΔCE between $\pm 4\%$ and $\pm 7\%$ based on the calibration errors of the diagnostics. Two representative absolute error bars at 30° and 180° are included in Fig. 122.13(a).

2-D PIC Simulations and Discussion

To elucidate on the absorption mechanism, 2-D PIC simulations were performed with the code OSIRIS.³² The theoretical CE is defined as the fraction of the calculated total kinetic energy of all the electrons above 9 keV to the total laser energy. Only electrons with kinetic energy above 9 keV can contribute to the K_α production in the Cu target since the binding energy for K-shell electrons is approximately 9 keV. The calculated absorption fraction taking all the electrons into account was significantly higher. Wedge-shaped-cavity targets of 30°, 45°, and 60° full opening angle were used in the calculations, assuming a fully ionized Cu target with an electron density of $10\times$ the nonrelativistic critical electron density n_c . The initial target temperature was set to room temperature (~ 0.1 eV). The plasma density ramped linearly from zero to peak density over a $1\text{-}\mu\text{m}$ distance at the target boundary. Some simulations were performed for different density scale lengths. The simulation box of $\sim 10 \times 14 \mu\text{m}$ was divided into 600×900 cells giving a spatial resolution of $0.1 c/\omega_1 = 0.016 \mu\text{m}$, where ω_1 is the laser frequency and c is the speed of light in vacuum. There were 49 particles of each species per cell. The boundary condition in the longitudinal direction that coincides with the laser propagation direction was thermal for particles and open for the electromagnetic field. Periodic boundary conditions for

both particles and fields were chosen in the transverse direction. The $1\text{-}\mu\text{m}$ -wavelength laser pulse propagated along the symmetry axis of the cavity and was focused into the vertex to an intensity of $1 \times 10^{19} \text{ W/cm}^2$. Gaussian profiles were assumed both in time and space with a 0.5-ps (FWHM) pulse duration and a $4\text{-}\mu\text{m}$ (FWHM) focal spot.

The square and triangle symbols in Fig. 122.13(b) represent the calculations for p - and s -polarization, respectively. The calculated conversion efficiency for p -polarization slightly increased with narrower angle and reached up to 30%. Within the calibration error, simulations and experiments were in agreement for p -polarization. The PIC code showed reasonable agreement with experiment for 30° and s -polarization but calculated significantly less absorption for larger angles. The calculated strong dependence on opening angle for s -polarization was not observed in the measurement. This discrepancy may be due to imperfect polarization in the experiment. Target-alignment errors were of the order of $\sim 5^\circ$, and microstructures observed on the target surface under a light microscope might have affected the interaction. Both effects probably contributed partially p -polarized laser light. The PIC simulations calculated only 2% absorption for flat foils under normal incidence, which is much lower than measured in the experiment ($\sim 20\%$). The theoretical CE increased to 7% when the foil was tilted by 5° in the plane of incidence [see the red square at 180° in Fig. 122.13(b)]. The plasma density scale length also has a strong effect on the absorption fraction. The calculated absorption increased to 20% assuming a $10\text{-}\mu\text{m}$ density ramp on the boundary of a flat target for normal incidence [see the green circle in Fig. 122.13(b)]. Target alignment

errors, target microstructures, and density scale length have a significant effect on CE, which could explain the discrepancy of the calculated and measured absorption for flat foils.

The principal laser-absorption mechanisms responsible for the production of suprathermal electrons in this experiment are the Brunel effect,³³ resonance absorption,³⁴ and $\mathbf{j} \times \mathbf{B}$ heating.³⁵ The Brunel mechanism, or vacuum heating, describes the process when electrons are dragged out of the target surface into the vacuum by strong p -polarized fields and accelerated back into the overdense plasma, where the electrons deposit their kinetic energy. This mechanism probably explains the measured increased absorption for p -polarization. It does not, however, explain why for s -polarization the absorption in narrow cavities was larger than for flat foils that were irradiated under normal incidence. This effect was probably due to the target geometry. Despite the tight focus, the majority of the laser beam interacted with a flat target surface at a large angle of incidence. The laser absorption of obliquely irradiated flat foils generally decreases with larger angle of incidence,³⁶ while here maximum absorption was measured for the narrowest wedge cavity with a corresponding angle of incidence of 75° . The light that is reflected from one surface reaches the opposite target surface where it has another chance to be absorbed. The narrower the cavity, the more reflections the light undergoes so that the overall absorption increases, although the absorption per reflection is small due to the shallow interaction angle. A narrow wedge with reflecting walls forms a cavity where the laser field reflects multiple times between opposite walls before reaching the tip. Interference of the electromagnetic field in the vicinity of the tip then leads to a standing wave pattern that might result in higher laser intensities than for comparable laser irradiation onto a flat target at normal incidence.

Lasinski *et al.* reported 2-D PIC simulations with flat-top cones and wedge-shaped-cavity targets¹² under similar conditions ($1\text{-}\mu\text{m}$ wavelength, intensity of 1×10^{19} W/cm²). Compared to simple slab interactions, cone targets resulted in increased laser light absorption and higher temperatures of the fast-electron population, which is in general agreement with the PIC simulations shown in this article. Higher absorption was calculated for p -polarized laser light in agreement with the results presented here. The absorption reached up to 75%, which was defined in Ref. 12 as the total kinetic energy in all the electrons divided by the total light energy that had entered the simulation. The absorption fraction in this work reached $\sim 70\%$ when all the electrons were taken into account.

The ions were kept immobile in most of the simulation runs, but some runs were performed with mobile ions. No significant difference in absorption and fast-electron energy distribution was observed between fixed- and mobile-ion runs. This is similar to simulations in Ref. 12 with mobile and fixed ions that produced no significant difference in absorption and heated-electron-density distribution for a 26° full opening angle wedge cavity. In contrast, mobile ion runs for flat foils and flattop cones calculated significantly more absorption than with immobile ions. In these target geometries, the deformation of the relativistic critical-density surface by ponderomotive effects is important, especially for flat foils irradiated under normal incidence and for cones with a central flattop portion. Rippling of the plasma surface leads to an enhanced absorption through the Brunel effect³³ and resonance absorption.³⁴ The relativistic critical surface deformation is less important for wedge cavities (or cones with pointed tips) since the laser is very efficiently absorbed along the upper side walls of the target, showing insignificant difference in mobile- and fixed-ion runs.

Conclusions

High-intensity laser-plasma interaction experiments were performed with wedge-shaped-cavity Cu targets with various opening angles at a laser intensity of 1×10^{19} W/cm². Absolute measurements with three independent diagnostics viewing the target from different observation locations provided spatially and spectrally resolved measurements of the $\sim 8\text{-keV}$ K_α emission from these targets. The diagnostics measured an isotropic emission. The coupling efficiency of short-pulse laser energy into fast electrons with kinetic energy >9 keV was inferred for wedge opening angles between 30° and 60° and for s - and p -polarized laser light irradiation. An increased coupling efficiency of up to 36% was measured for the narrowest wedge and for p -polarization compared to 20% for flat foils. The experimental results are in reasonable agreement with predictions from 2-D PIC simulations for p -polarized laser light and for the narrowest cavity for s -polarization. For s -polarization and wider cavities, the calculated absorption is significantly lower than in the experiment.

ACKNOWLEDGMENT

The authors are indebted to the Target Fabrication Groups at General Atomics and LLE and to C. Mileham for experimental support. This work was supported by the U.S. Department of Energy Office of Inertial Confinement Fusion under Cooperative Agreement No. DE-FC52-08NA28302, the OFES Fusion Science Center grant No. DE-FC02-04ER54789, the OFES ACE grant No. DE-FG02-05ER54839, the University of Rochester, and the New York State Energy Research and Development Authority. The support of DOE does not constitute an endorsement by DOE of the views expressed in this article.

REFERENCES

1. M. Tabak *et al.*, *Phys. Plasmas* **1**, 1626 (1994).
2. K. A. Flippo *et al.*, *Phys. Plasmas* **15**, 056709 (2008).
3. T. Nakamura *et al.*, *Phys. Plasmas* **14**, 103105 (2007).
4. N. Renard-Le Galloudec *et al.*, *Phys. Rev. Lett.* **102**, 205003 (2009).
5. B. I. Cho *et al.*, *Phys. Plasmas* **15**, 052701 (2008).
6. P. M. Nilson, W. Theobald, J. F. Myatt, C. Stoeckl, M. Storm, J. D. Zuegel, R. Betti, D. D. Meyerhofer, and T. C. Sangster, *Phys. Rev. E* **79**, 016406 (2009).
7. L. Van Woerkom *et al.*, *Phys. Plasmas* **15**, 056304 (2008).
8. J. A. King, K. U. Akli, R. R. Freeman, J. Green, S. P. Hatchett, D. Hey, P. Jaanimagi, M. H. Key, J. Koch, K. L. Lancaster, T. Ma, A. J. MacKinnon, A. MacPhee, P. A. Norreys, P. K. Patel, T. Phillips, R. B. Stephens, W. Theobald, R. P. J. Town, L. Van Woerkom, B. Zhang, and F. N. Beg, *Phys. Plasmas* **16**, 020701 (2009).
9. S. D. Baton *et al.*, *Phys. Plasmas* **15**, 042706 (2008).
10. J. Rassuchine *et al.*, *Phys. Rev. E* **79**, 036408 (2009).
11. F. Beg, *Bull. Am. Phys. Soc.* **54**, 299 (2009); A. G. MacPhee *et al.*, *Phys. Rev. Lett.* **104**, 055002 (2010).
12. B. F. Lasinski, *Phys. Plasmas* **16**, 012705 (2009).
13. Y. Sentoku *et al.*, *Phys. Plasmas* **11**, 3083 (2004).
14. T. Nakamura *et al.*, *Phys. Rev. Lett.* **93**, 265002 (2004).
15. V. Bagnoud, I. A. Begishev, M. J. Guardalben, J. Puth, and J. D. Zuegel, *Opt. Lett.* **30**, 1843 (2005).
16. C. Dorrer, A. V. Okishev, I. A. Begishev, J. D. Zuegel, V. I. Smirnov, and L. B. Glebov, *Opt. Lett.* **32**, 2378 (2007).
17. A. J. MacKinnon *et al.*, *Phys. Rev. Lett.* **88**, 215006 (2002).
18. J. Myatt, W. Theobald, J. A. Delettrez, C. Stoeckl, M. Storm, T. C. Sangster, A. V. Maximov, and R. W. Short, *Phys. Plasmas* **14**, 056301 (2007).
19. P. M. Nilson, W. Theobald, J. Myatt, C. Stoeckl, M. Storm, O. V. Gotchev, J. D. Zuegel, R. Betti, D. D. Meyerhofer, and T. C. Sangster, *Phys. Plasmas* **15**, 056308 (2008).
20. J. D. Zuegel, V. Bagnoud, I. A. Begishev, M. J. Guardalben, J. Keegan, J. Puth, and L. J. Waxer, presented at the Conference on Lasers and Electro Optics (CLEO 2003), Baltimore, MD, 1–6 June 2003 (Paper CME3).
21. H. Chen, B. Soom, B. Yaakobi, S. Uchida, and D. D. Meyerhofer, *Phys. Rev. Lett.* **70**, 3431 (1993).
22. W. Theobald, K. Akli, R. Clarke, J. Delettrez, R. R. Freeman, S. Glenzer, J. Green, G. Gregori, R. Heathcote, N. Izumi, J. A. King, J. A. Koch, J. Kuba, K. Lancaster, A. J. MacKinnon, M. Key, C. Mileham, J. Myatt, D. Neely, P. A. Norreys, H.-S. Park, J. Pasley, P. Patel, S. P. Regan, H. Sawada, R. Shepherd, R. Snavelly, R. B. Stephens, C. Stoeckl, M. Storm, B. Zhang, and T. C. Sangster, *Phys. Plasmas* **13**, 043102 (2006).
23. K. U. Akli, M. H. Key, H. K. Chung, S. B. Hansen, R. R. Freeman, M. H. Chen, G. Gregori, S. Hatchett, D. Hey, N. Izumi, J. King, J. Kuba, P. Norreys, A. J. MacKinnon, C. D. Murphy, R. Snavelly, R. B. Stephens, C. Stoeckel, W. Theobald, and B. Zhang, *Phys. Plasmas* **14**, 023102 (2007).
24. Spectral Instruments, Tucson, AZ 85745 (http://www.specinst.com/Products/800s_datasheet.pdf).
25. Momentive Performance Materials, Albany, NY 12211 (<http://www.momentive.com/momentiveInternetDoc/Internet/Static%20Files/Documents/4%20Color%20Brochures/85508.pdf>).
26. B. Yaakobi and A. J. Burek, *IEEE J. Quantum Electron.* **QE-19**, 1841 (1983).
27. CCD42–40 Ceramic AIMO Back Illuminated Compact Package High Performance CCD Sensor, e2v technologies (uk) limited, Chelmsford, Essex CM1 2QU, UK.
28. B. R. Maddox *et al.*, *Rev. Sci. Instrum.* **79**, 10E924 (2008).
29. H.-S. Park, D. M. Chambers, H.-K. Chung, R. J. Clarke, R. Eagleton, E. Giraldez, T. Goldsack, R. Heathcote, N. Izumi, M. H. Key, J. A. King, J. A. Koch, O. L. Landen, A. Nikroo, P. K. Patel, D. F. Price, B. A. Remington, H. F. Robey, R. A. Snavelly, D. A. Steinman, R. B. Stephens, C. Stoeckl, M. Storm, M. Tabak, W. Theobald, R. P. J. Town, J. E. Wickersham, and B. B. Zhang, *Phys. Plasmas* **13**, 056309 (2006).
30. M. J. Berger, in *Methods in Computational Physics: Advances in Research and Applications*, edited by B. Alder, S. Fernbach, and M. Rotenberg, Volume 1: Statistical Physics (Academic Press, New York, 1963), pp. 135–215.
31. B. L. Henke, E. M. Gullikson, and J. C. Davis, *At. Data Nucl. Data Tables* **54**, 181 (1993).
32. R. A. Fonseca *et al.*, in *Computational Science—ICCS 2002*, edited by P. M. A. Sloot *et al.*, Lecture Notes in Computer Science (Springer, Berlin, 2002), Vol. 2331, pp. 342–351.
33. F. Brunel, *Phys. Rev. Lett.* **59**, 52 (1987).
34. P. Gibbon and A. R. Bell, *Phys. Rev. Lett.* **68**, 1535 (1992).
35. S. C. Wilks and W. L. Kruer, *IEEE J. Quantum Electron.* **33**, 1954 (1997).
36. T. Feurer, W. Theobald, R. Sauerbrey, I. Uschmann, D. Altenbernd, U. Teubner, P. Gibbon, E. Förster, G. Malka, and J. L. Miquel, *Phys. Rev. E* **56**, 4608 (1997).

Crossed-Beam Energy Transfer in Inertial Confinement Fusion Implosions on OMEGA

Inertial confinement fusion (ICF) uses the energy of multiple laser beams to implode a millimeter-scale capsule containing nuclear fuel.¹ Direct-drive implosions are driven by heat that is generated by the absorption of laser light ($I \sim 10^{14}$ to 10^{15} W/cm²) in a plasma corona surrounding the capsule.² The crossed-beam energy transfer (CBET) caused by stimulated Brillouin scattering (SBS)³ reduces the laser absorption, making it possible for incoming light to bypass the highest absorption region near the critical radius, at which the electron number density n_e equals the critical density $n_{cr} = \pi c^2 m_e / \lambda_L^2 e^2$, where λ_L is the laser wavelength in vacuum. Under certain conditions, the CBET may be large and significantly reduce the performance of ICF implosions.^{4–6}

In this article, the effect of SBS in implosion experiments on the OMEGA Laser System,⁷ operating at $\lambda_L = 351$ nm, is investigated. The results of a new CBET model coupled to the one-dimensional radiative hydrodynamic code *LILAC*⁸ are presented and quantitatively compared with experimental results. It is shown that the best agreement between simulations and scattered-light⁹ and bang-time¹⁰ measurements can be obtained by simultaneously employing the CBET and non-local thermal transport.^{11,12} *LILAC* simulations show that using two-color laser light with a wavelength separation $\Delta\lambda \sim 5$ to 8 Å can reduce the CBET and increase the absorption, thereby improving the implosion efficiency.

The CBET model considers the propagation of two crossing laser beams (probe and pump) in a moving plasma and the interaction of these beams with an ion-acoustic wave (IAW) that they excite.^{4,13,14} Assuming *s*-polarized light and steady state, the probe beam intensity $I^{(1)}$ along the path ℓ can be calculated as follows:

$$I^{(1)} = I_0^{(1)} \exp \left\{ \int \left[\eta L_{CBET}^{-1} - L_{IB}^{-1} \right] d\ell \right\}, \quad (1)$$

where L_{IB} is the inverse bremsstrahlung absorption scale length,³ L_{CBET} is the scale length of energy loss or gain caused by CBET, and η is an adjustment parameter $0 \leq \eta \leq 1$. The scale length L_{CBET} is defined by

$$L_{CBET}^{-1} = 0.0585 \frac{n_e/n_{cr}}{\sqrt{1 - n_e/n_{cr}}} \times \frac{\lambda_{L,\mu m} I_{14}^{(2)}}{(1 + 3T_i/ZT_e) T_{e,keV}} \frac{P(\chi)}{\tilde{\nu}_a} \mu m^{-1}, \quad (2)$$

where $\lambda_{L,\mu m}$ is the laser wavelength in microns, $I_{14}^{(2)}$ is the pump-beam intensity in units of 10^{14} W/cm², T_e and T_i are the electron and ion temperatures ($T_{e,keV}$ in keV), Z is the average ionization, ν_a is the damping coefficient for IAW's, $\tilde{\nu}_a = \nu_a/k_a c_a$ is the dimensionless damping,

$$P(\chi) = \frac{\tilde{\nu}_a^2 \chi}{\tilde{\nu}_a^2 \chi^2 - (1 - \chi^2)} \quad (3)$$

is the resonance function,⁴ $\chi = -\omega_a/k_a c_a + (\mathbf{k}_a \cdot \mathbf{u})/k_a c_a$, \mathbf{u} is the velocity vector, c_a is the ion-acoustic velocity, $\omega_a = \omega_1 - \omega_2$ and $\mathbf{k}_a = \mathbf{k}_1 - \mathbf{k}_2$ are the IAW frequency and wave vector, respectively, and ω and \mathbf{k} with the lower indexes 1 and 2 are the frequencies and wave vectors of the probe and pump light, respectively.

The CBET model has been incorporated into the laser absorption algorithm in *LILAC*. The algorithm calculates the integral in Eq. (1) along various light-ray paths, accounting for all possible beam crossings in three dimensions. Doppler shift of the light frequencies is calculated using the equation $\Delta\omega = \omega_L (\partial\tau/\partial t)$ (Ref. 15), where τ is the light-wave flight time and $\omega_L = 2\pi c/\lambda_L$. The damping is approximately $\tilde{\nu}_a \approx 0.2$ for CH plasma under the considered conditions.¹⁶ Simulations, however, showed a weak dependence on $\tilde{\nu}_a$ over the interval $0.1 < \tilde{\nu}_a < 0.5$.

The energy is not conserved exactly in Eq. (1) because pump-light depletion is neglected. To enforce this conservation, the algorithm normalizes the total energy gain (or loss) for outgoing light to the total energy loss (or gain) for incoming

light at each radius. Calculations were significantly simplified assuming a uniform illumination of implosion capsules (but the intensity profile inside the beams is retained). Test simulations using this simplified assumption and the illumination by all 60 OMEGA beams showed good agreement between the two approaches. The random polarization of light on OMEGA is accounted for by reducing the numerical factor in Eq. (2) by 0.5.

Typical implosion targets on OMEGA are room-temperature-D₂- or DT-gas-filled plastic shells and cryogenic D₂- or DT-ice shells with a thin plastic overcoat. The outer diameter is about 840 to 880 μm. Laser pulses can have various shapes with pickets and pedestals, have durations from 0.1 to 4 ns, and deliver on target up to 30 kJ. LILAC simulations of OMEGA implosions have revealed the importance of CBET at laser intensities $I \gtrsim 10^{14}$ W/cm². At $I > 5 \times 10^{14}$ W/cm², the energy transfer can reach a significant level $\gtrsim 30\%$ of the incident energy. The CBET is most efficient in a radially extended plasma corona, which develops after the first 100 to 200 ps of a pulse. The transfer occurs in a relatively wide radial interval ~ 50 μm, in which n_e is in the range of 0.2 to 0.3 n_{cr} (see Fig. 122.14). As a result, the absorption is spatially redistributed, shifting outward, and its integrated value can be changed [see black and blue lines in Fig. 122.14(a)]. The most-energetic transfers involve the incoming light with small impact parameters (at the beam center) and outgoing light, which is inclined at $\sim 20^\circ$ to 30° with respect to the radial direction. The former light

loses some energy and the latter gains the energy. The nonzero angles between interacting light rays explain our finding that the energy transfer is maximized at the supersonic region of the corona, at $u_r/c_a \approx 1.4$ [see the red line in Fig. 122.14(a) and the blue dashed line in Fig. 122.14(b)], instead of at the transonic point, $u_r/c_a = 1$, if the angles were close to zero.⁵ Here, u_r is the radial component of the velocity. Fortunately, most CBET interaction occurs at moderate angles ($\lesssim 25^\circ$), where the paraxial approximation used in Eq. (2) is valid.

The CBET redistributes the energy inside the laser beams from light rays with small impact parameters to light rays with larger ones. This redistribution and corresponding modification of the absorption can be emulated using the effective profile in which the beam's central intensity is decreased and the beam's edge intensity is increased (see Fig. 122.15). Such effective profiles may be useful in multidimensional simulations in which the direct employment of the CBET model is highly impractical.¹⁷

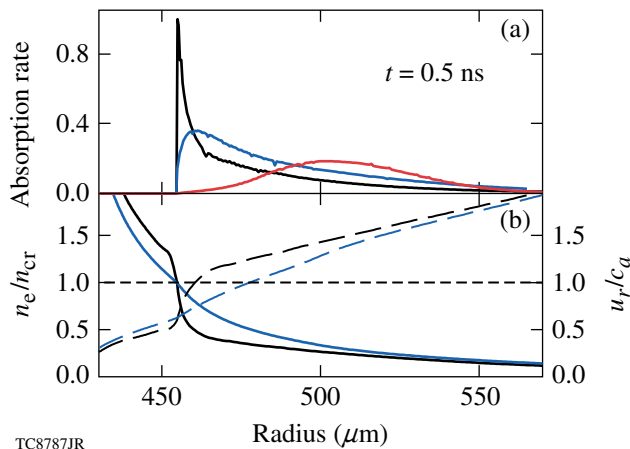


Figure 122.14 Simulated (a) absorption rate per unit volume (in relative units, black and blue lines) and (b) relative electron density n_e/n_{cr} (solid lines) and Mach number u_r/c_a (dashed lines), at $t = 0.5$ ns for an 880-μm-diam plastic shell (20-μm CH wall) imploded with a 1-ns square pulse at $I \sim 10^{15}$ W/cm². The simulations with flux-limited transport ($f = 0.06$) are shown in black and nonlocal transport and CBET ($\eta = 0.75$) in blue. The CBET rate (in relative units) from incoming to outgoing light is shown in (a) in red.

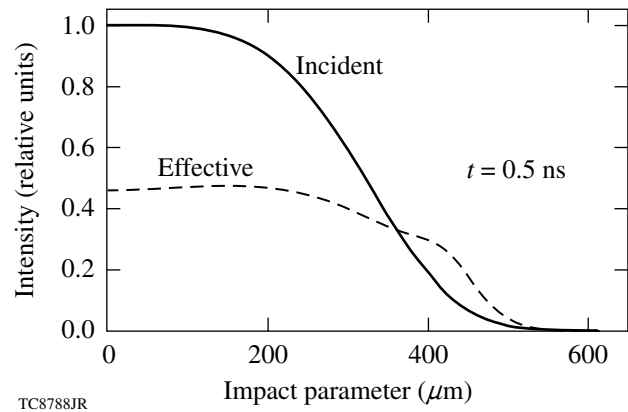


Figure 122.15 Incident (super-Gaussian with an index $n = 4$) and effective beam profiles at $t = 0.5$ ns for the same simulation with nonlocal transport and CBET as shown in Fig. 122.14. The effective profile emulates the loss ($\approx 26\%$) and redistribution of the energy inside the beam caused by CBET.

OMEGA planar and implosion experiments are typically simulated by employing the Spitzer thermal transport¹⁸ with flux limitation, in which the phenomenological constant-value flux-limiting parameter f is used.¹⁹ Assuming $f = 0.06$, the model can explain reasonably well planar shock-timing experiments²⁰ and implosion experiments with short (≤ 1 ns), square pulses.¹¹ In the case of long, shaped pulses, however, the flux-limited transport experiences difficulties in consistently explaining the whole range of experimental data, including

bang-time and scattered-light measurements.¹¹ The inaccuracy of the flux-limited transport becomes especially apparent in adiabat-shaped designs^{21,22} in which a time-dependent flux limiting was proposed.^{11,23}

A step-up from the Spitzer transport is the nonlocal transport model,^{11,12} which calculates heat fluxes by solving the simplified Boltzmann equation and employing the Krook approximation.²⁴ This transport introduces two major improvements. First, the flux in regions with steep temperature gradients is reduced from the Spitzer value, eliminating the need for flux limitation. Second, the heating by long-range hot electrons is accounted for. The latter introduces changes in the density scale length near n_{cr} , making this length longer by a factor of ~ 10 [Fig. 122.14(b)]. The longer scale length significantly reduces the prediction for resonance absorption²⁵ and reduces the strong bremsstrahlung absorption peak near critical density [Fig. 122.14(a)]. Simulations using the nonlocal transport predict well the shock-timing experiments with short picket pulses (~ 100 to 200 ps), but they over-predict the laser drive in implosions with long pulses.⁹

The agreement between simulations and experiments is significantly improved when the nonlocal transport and CBET are used simultaneously. As an example, Fig. 122.16 compares

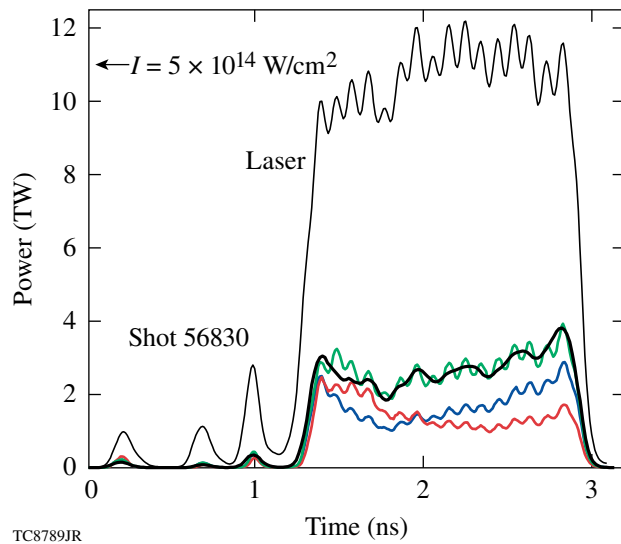


Figure 122.16

Scattered-light power for an $830\text{-}\mu\text{m}$ -diam plastic shell (9 atm of D_2 -gas fill, $26\text{-}\mu\text{m}$ CH wall) imploded with 18.3 kJ. The incident laser power and experimental scattered power (within $\pm 5\%$ accuracy) are shown by the thin and thick black lines, respectively. The *LILAC* predictions with flux-limited ($f = 0.06$) and nonlocal transports are shown in red and blue, respectively, and with nonlocal transport and CBET ($\eta = 0.75$) in green.

the measurement and various simulations of time-resolved scattered-light power for a plastic-shell implosion (OMEGA shot 56830). The simulated power, using nonlocal transport and CBET (green line), shows very good agreement with the scattered-light measured power (thick black line) for $\eta = 0.75$. The models without CBET, which use flux-limited or nonlocal transport (red and blue lines, respectively), clearly underestimate the scattered power. Similar results were found in simulations of different warm and cryogenic implosions.

Figure 122.17 shows the neutron-production history for the implosion in Fig. 122.16. Again, the bang time inferred from the neutron data predicted in the model with CBET (thin solid line) shows very good agreement with the bang time inferred from the measured neutron data (thick solid line). In contrast, the bang times inferred from the results of the models without CBET (dashed and dotted lines in Fig. 122.17) are about 150 ps earlier. The reduction of the measured neutron rate with respect to the predicted rates in Fig. 122.17 is due to the growth of perturbations from laser imprint, which affects the implosion performance¹ and is not considered in *LILAC* simulations.

Based on simulations of warm and cryogenic implosions with different laser energies and pulses, one concludes that bang-time and scattered-light measurements can typically

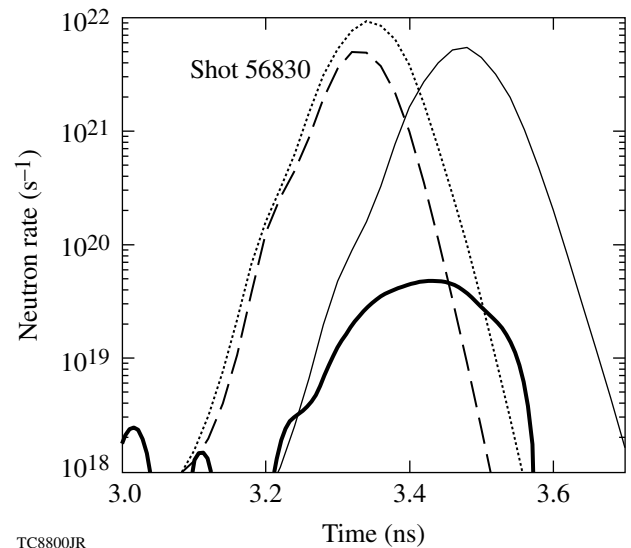


Figure 122.17

Neutron-production history for the same implosion as in Fig. 122.16. The measured history (thick solid line) is determined with ~ 50 -ps uncertainty. The *LILAC* predictions with flux-limited ($f = 0.06$) and nonlocal transports are shown by the dashed and dotted lines, respectively, and with nonlocal transport and CBET ($\eta = 0.75$) by the thin solid line.

be explained using a somewhat-reduced CBET, in which η is assumed between 0.5 and 1. This relatively wide uncertainty interval of η can be partially attributed to the uncertainties of experimental results. It is apparent, however, that the experimentally suggested mean value $\eta \sim 0.75$ is smaller than the theoretical prediction $\eta = 1$. This suggests the inaccuracy of the simplified CBET model [Eqs. (1)–(3)] is of the order of $\sim 25\%$.

Since the light refraction and frequency shift are sensitive to the corona's spatial structure, the simulated coronal structure can be validated using time-dependent scattered-light spectral measurements.⁹ Figure 122.18 shows an example of the measurement and simulations for an 843- μm -diam plastic shell (20- μm CH wall) imploded with 1-ns square pulse at $I \sim 8 \times 10^{14} \text{ W/cm}^2$ (OMEGA shot 50601). Two simulations are compared using (1) flux-limited transport [Fig. 122.18(b)] and (2) nonlocal transport and CBET [Fig. 122.18(c)]. Both simulated spectra reproduce reasonably well the basic structure of the measured spectrum [Fig. 122.18(a)]. The initial (at $t \lesssim 0.5 \text{ ns}$) blue shift is attributed to the Doppler shift of light reflected in the expanding part of the corona and the late-time (at $t \gtrsim 0.5 \text{ ns}$) red-shifted “fan tails” are produced by light reflected in the inward-moving part. However, these simulations reveal important differences. The flux-limited model predicts an insufficient initial blue shift [Ref. 26, feature A in Fig. 122.18(b)], which clearly deviates from the measured spectrum. The blue shift predicted by the model with nonlocal transport [Fig. 122.18(c)] shows much closer agreement to the experiment. The insufficient blue shift in the flux-limited model can be explained by a more-diluted corona [see Fig. 122.14(b)],

and, consequently, a deeper location of the light-ray turning points toward the critical radius, where the coronal outflow velocity is reduced.

The structure of the fan tails is less susceptible to the choice of a thermal-transport model but depends more on the presence of CBET. The most-red-shifted parts of the fan tail are produced by light rays that penetrate deeply into the corona, almost reaching the critical-density region. The larger the fraction of the incident light that reaches the critical radius, the more intense the red-shifted spectrum. Such red-shifted fan tails were found in simulations without CBET [Ref. 26, feature B in Fig. 122.18(b)]. In contrast and in agreement with measurements, simulations with CBET predict a less-red-shifted fan tail [Fig. 122.18(c)].

Splitting the incident laser light into two or more colors can reduce the CBET by shifting and suppressing the coupling resonances [Eq. (3)]. This color-splitting technique can be employed to increase the laser absorption in direct-drive implosions. Figure 122.19 shows the predicted variation of the absorption fraction (solid line) for two-color light with a wavelength separation $\Delta\lambda$. Here, the same implosion was assumed as in Fig. 122.16 and the laser energy is equally distributed between the colors. The dashed line in Fig. 122.19 shows the absorption fraction for the model with the expected asymptotic 50% reduction of CBET at $\Delta\lambda \gg \lambda_L (c_a/c)$, which corresponds to $\Delta\lambda = 0$ and η reduced by 0.5 (i.e., $\eta = 0.375$). The increase in the absorption is moderate ($\approx 5\%$) for $\Delta\lambda \sim 5 \text{ \AA}$ and takes the maximum ($\approx 8\%$) for $\Delta\lambda \sim 8$ to 10 \AA . There is

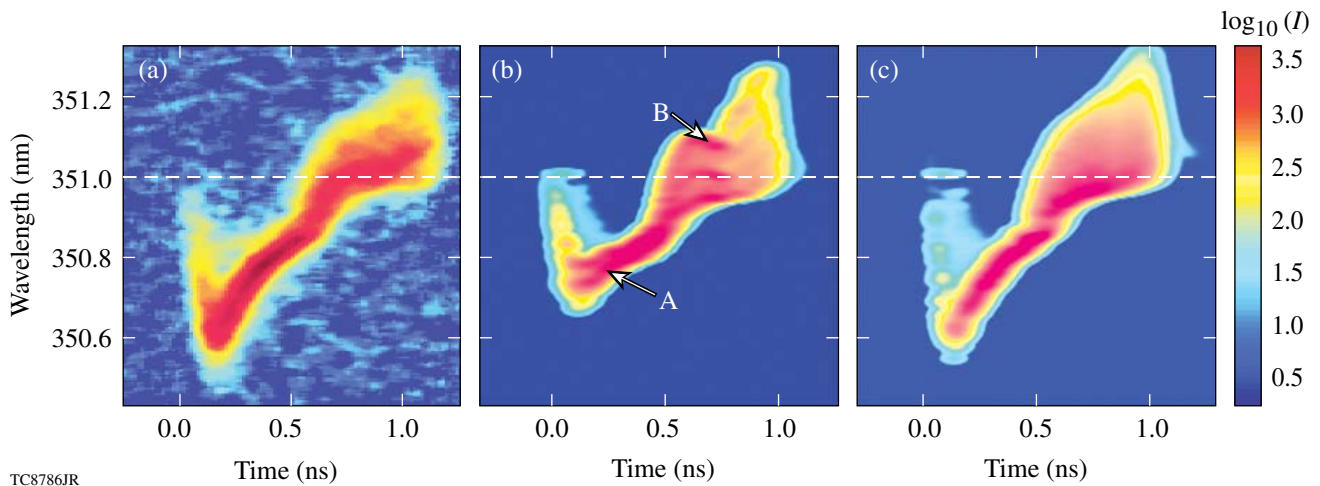
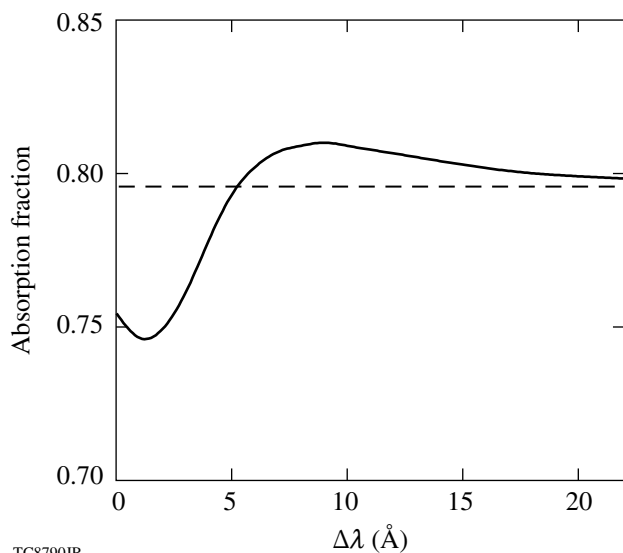


Figure 122.18

(a) Measured and [(b),(c)] simulated scattered-light spectra for a plastic-shell implosion (OMEGA shot 50601). *LILAC* predictions with flux-limited transport are shown in (b), and nonlocal transport with CBET ($\eta = 0.75$) in (c). The laser wavelength is indicated by the dashed lines.



TC8790JR

Figure 122.19

Absorption fraction (solid line) as a function of the wavelength separation $\Delta\lambda$ in two-color laser light. The dashed line corresponds to $\Delta\lambda = 0$ and 50%-reduced CBET.

little change in the absorption for $\Delta\lambda < 4 \text{ \AA}$, which confirms the experimental finding that the absorption is insensitive to the use of 1-THz smoothing by special dispersion (SSD),²⁷ which widens the laser bandwidth by ~ 3 to 4 \AA . It should be noted that this color-splitting technique may be more efficient in direct-drive implosions at the National Ignition Facility²⁸ because of larger CBET in larger-scale targets.

In summary, it has been shown that the effect of CBET in direct-drive ICF implosions on OMEGA is significant and results in the reduced laser absorption (by $\sim 20\%$ to 30%). *LILAC* simulations using CBET and nonlocal thermal transport show good agreement with bang-time and scattered-light measurements for warm and cryogenic implosions using different pulse shapes and plastic (CH or CD) as an ablator. The simulations, using flux-limited transport ($f=0.06$) and without CBET, overpredict the absorption for long pulses ($>1 \text{ ns}$), resulting in earlier bang-time predictions. The absorption can be increased by employing two-color laser light with a wavelength separation of $\Delta\lambda \sim 5$ to 8 \AA .

ACKNOWLEDGMENT

This work was supported by the U.S. Department of Energy Office of Inertial Confinement Fusion under Cooperative Agreement No. DE-FC52-08NA28302, the University of Rochester, and the New York State Energy Research and Development Authority. The support of DOE does not constitute an endorsement by DOE of the views expressed in this article.

REFERENCES

1. J. D. Lindl, *Inertial Confinement Fusion: The Quest for Ignition and Energy Gain Using Indirect Drive* (Springer-Verlag, New York, 1998), Chap. 6, pp. 39, 61.
2. R. L. McCrory, J. M. Soures, C. P. Verdon, F. J. Marshall, S. A. Letzring, S. Skupsky, T. J. Kessler, R. L. Kremens, J. P. Knauer, H. Kim, J. Delettrez, R. L. Keck, and D. K. Bradley, *Nature* **335**, 225 (1988).
3. W. L. Kruer, *The Physics of Laser-Plasma Interactions, Frontiers in Physics*, Vol. 73, edited by D. Pines (Addison-Wesley, Redwood City, CA, 1988), Chap. 4, pp. 45, 87.
4. C. J. Randall, J. R. Albritton, and J. J. Thomson, *Phys. Fluids* **24**, 1474 (1981).
5. J. Myatt, A. V. Maximov, W. Seka, R. S. Craxton, and R. W. Short, *Phys. Plasmas* **11**, 3394 (2004).
6. W. Seka, H. A. Baldis, J. Fuchs, S. P. Regan, D. D. Meyerhofer, C. Stoeckl, B. Yaakobi, R. S. Craxton, and R. W. Short, *Phys. Rev. Lett.* **89**, 175002 (2002).
7. T. R. Boehly, D. L. Brown, R. S. Craxton, R. L. Keck, J. P. Knauer, J. H. Kelly, T. J. Kessler, S. A. Kumpan, S. J. Loucks, S. A. Letzring, F. J. Marshall, R. L. McCrory, S. F. B. Morse, W. Seka, J. M. Soures, and C. P. Verdon, *Opt. Commun.* **133**, 495 (1997).
8. J. Delettrez, R. Epstein, M. C. Richardson, P. A. Jaanimagi, and B. L. Henke, *Phys. Rev. A* **36**, 3926 (1987).
9. W. Seka, D. H. Edgell, J. P. Knauer, J. F. Myatt, A. V. Maximov, R. W. Short, T. C. Sangster, C. Stoeckl, R. E. Bahr, R. S. Craxton, J. A. Delettrez, V. N. Goncharov, I. V. Igumenshchev, and D. Shvarts, *Phys. Plasmas* **15**, 056312 (2008).
10. R. A. Lerche, D. W. Phillion, and G. L. Tietbohl, *Rev. Sci. Instrum.* **66**, 933 (1995).
11. V. N. Goncharov, O. V. Gotchev, E. Vianello, T. R. Boehly, J. P. Knauer, P. W. McKenty, P. B. Radha, S. P. Regan, T. C. Sangster, S. Skupsky, V. A. Smalyuk, R. Betti, R. L. McCrory, D. D. Meyerhofer, and C. Cherfils-Cl  rouin, *Phys. Plasmas* **13**, 012702 (2006).
12. V. N. Goncharov, T. C. Sangster, P. B. Radha, R. Betti, T. R. Boehly, T. J. B. Collins, R. S. Craxton, J. A. Delettrez, R. Epstein, V. Yu. Glebov, S. X. Hu, I. V. Igumenshchev, J. P. Knauer, S. J. Loucks, J. A. Marozas, F. J. Marshall, R. L. McCrory, P. W. McKenty, D. D. Meyerhofer, S. P. Regan, W. Seka, S. Skupsky, V. A. Smalyuk, J. M. Soures, C. Stoeckl, D. Shvarts, J. A. Frenje, R. D. Petrasso, C. K. Li, F. S  guin, W. Manheimer, and D. G. Colombant, *Phys. Plasmas* **15**, 056310 (2008).
13. J. A. F. Hittinger *et al.*, *J. Comput. Phys.* **209**, 695 (2005).
14. P. Michel *et al.*, *Phys. Rev. Lett.* **102**, 025004 (2009).
15. T. Dewandre, J. R. Albritton, and E. A. Williams, *Phys. Fluids* **24**, 528 (1981).

16. E. A. Williams, R. L. Berger, R. P. Drake, A. M. Rubenchik, B. S. Bauer, D. D. Meyerhofer, A. C. Gaeris, and T. W. Johnston, *Phys. Plasmas* **2**, 129 (1995).
17. A. Shvydky, P. W. McKenty, J. A. Delettrez, I. V. Igumenshchev, D. H. Edgell, S. Skupsky, and R. L. McCrory, *Bull. Am. Phys. Soc.* **54**, 307 (2009).
18. L. Spitzer, Jr. and R. Härm, *Phys. Rev.* **89**, 977 (1953).
19. R. C. Malone, R. L. McCrory, and R. L. Morse, *Phys. Rev. Lett.* **34**, 721 (1975).
20. T. R. Boehly, E. Vianello, J. E. Miller, R. S. Craxton, T. J. B. Collins, V. N. Goncharov, I. V. Igumenshchev, D. D. Meyerhofer, D. G. Hicks, P. M. Celliers, and G. W. Collins, *Phys. Plasmas* **13**, 056303 (2006).
21. V. N. Goncharov, J. P. Knauer, P. W. McKenty, P. B. Radha, T. C. Sangster, S. Skupsky, R. Betti, R. L. McCrory, and D. D. Meyerhofer, *Phys. Plasmas* **10**, 1906 (2003).
22. K. Anderson and R. Betti, *Phys. Plasmas* **11**, 5 (2004).
23. A. Sunahara, J. A. Delettrez, C. Stoeckl, R. W. Short, and S. Skupsky, *Phys. Rev. Lett.* **91**, 095003 (2003).
24. N. A. Krall and A. W. Trivelpiece, *Principles of Plasma Physics* (San Francisco Press, Inc., San Francisco, 1986), p. 316.
25. I. V. Igumenshchev, V. N. Goncharov, W. Seka, D. Edgell, and T. R. Boehly, *Phys. Plasmas* **14**, 092701 (2007).
26. D. Edgell, W. Seka, J. A. Delettrez, R. S. Craxton, V. N. Goncharov, I. V. Igumenshchev, J. Myatt, A. V. Maximov, R. W. Short, T. C. Sangster, and R. E. Bahr, *Bull. Am. Phys. Soc.* **52**, 195 (2007); *ibid.*, *Bull. Am. Phys. Soc.* **53**, 168 (2008); *ibid.*, *Bull. Am. Phys. Soc.* **54**, 145 (2006).
27. S. Skupsky and R. S. Craxton, *Phys. Plasmas* **6**, 2157 (1999).
28. S. W. Haan, S. M. Pollaine, J. D. Lindl, L. J. Suter, R. L. Berger, L. V. Powers, W. E. Alley, P. A. Amendt, J. A. Futterman, W. K. Levedahl, M. D. Rosen, D. P. Rowley, R. A. Sacks, A. I. Shestakov, G. L. Strobel, M. Tabak, S. V. Weber, G. B. Zimmerman, W. J. Krauser, D. C. Wilson, S. V. Coggeshall, D. B. Harris, N. M. Hoffman, and B. H. Wilde, *Phys. Plasmas* **2**, 2480 (1995).

Characterization of Highly Stable, Mid-IR, GaSb-Based Laser Diodes

Introduction

Mid-IR, 3000- to 3500-nm laser sources are important for various applications including gas sensing, spectral analysis, infrared illumination, countermeasures, medical diagnostics, and others. One particular application is layering cryogenic targets for inertial confinement fusion (ICF) implosions at the Omega Laser Facility.¹ Careful layering of cryogenic targets is important to maximize the fuel density in ICF implosions. These targets consist of $\sim 900\text{-}\mu\text{m}$ -diam microcapsules that contain frozen D_2 (deuterium–deuterium) gas. The frozen deuterium is “layered” so that it is uniformly distributed around the inner surface of the capsule.^{2,3} The layering process relies on the target being in a spherical isotherm that is uniformly illuminated by mid-IR light. The wavelength is tuned to the absorption peak in the fuel material (3160 nm with $\sim 20\text{-nm}$ FWHM for D_2 targets⁴). Since thicker regions of ice will have a longer path length, they absorb more radiation, so they will be relatively hot spots. Fuel material sublimates from the hotter regions and condenses and refreezes on the thinner, colder regions, leading to a uniform distribution of fuel material. For this process to produce layers with the required uniformity, the

temperature must be held very close to the material’s melting point. As a result, the mid-IR source’s output power and spectrum must be temporally stable to avoid over- or underheating.

Currently a mid-IR optical parametric oscillator (OPO) is used to layer the targets.⁵ It was shown in Ref. 6 that mid-IR, GaSb-based quantum-well laser diodes can be used for target layering. Here we report on selection and characterization of a mid-IR laser diode that performs optimally for the cryogenic target layering.

Laser-Diode Selection

Three laser diodes emitting at ~ 3160 nm have been grown and assembled as described in Ref. 6. During the selection process, the output power versus driver current and spectral shape at 3160 nm were measured (see Fig. 122.20).

Diode #1 delivered the highest output power of >50 mW at 2400 mA of driver current. Its spectrum was centered at 3160 nm and had a compact envelope with $<20\text{-nm}$ FWHM. Diode #2 had the same slope efficiency as diode #1 with lower

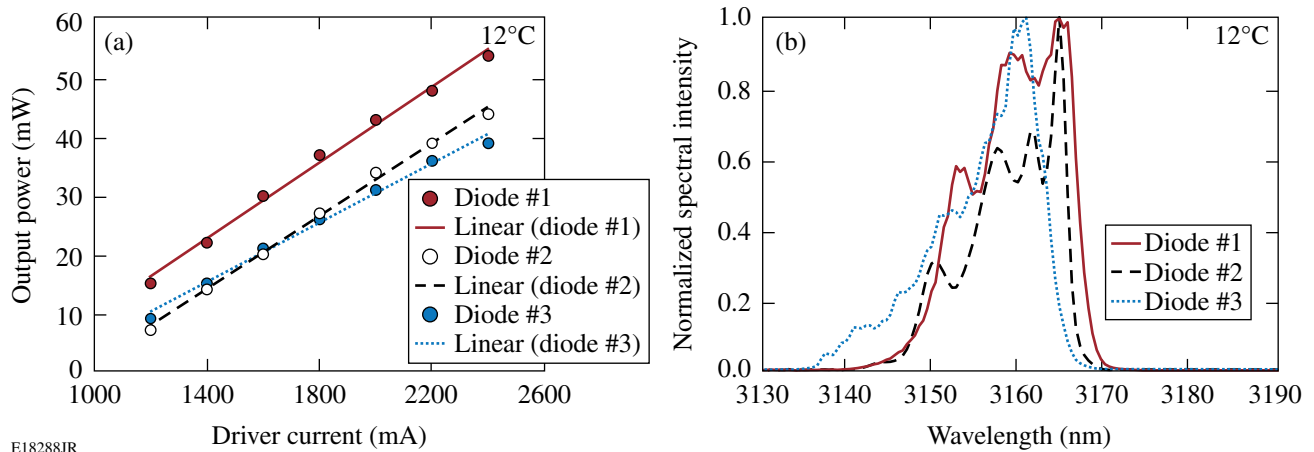


Figure 122.20

(a) Output power versus driver current and (b) spectra at 3160 nm for three tested laser diodes.

output power. Its spectrum had more-pronounced intensity variations than diode #1. Diode #3 had lower slope efficiency and output power than both diodes #1 and #2. Its spectrum was asymmetric and had a wide short-wavelength wing. Diode #1 has been selected for further characterization.

Laser-Diode Characterization

The output power of diode #1 was measured at various driver currents and heatsink temperatures (see Fig. 122.21). The highest power—54 mW—was produced at 12°C and 2400 mA of the driver current. A further temperature decrease might cause condensation and higher current might damage the diode. The output-power variations over 24 h of operation were ~1.3% rms and might be reduced by improving temperature stabilization of the diode.

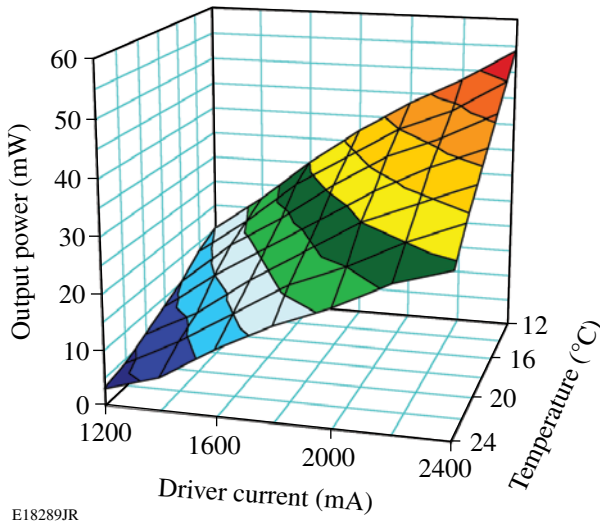


Figure 122.21
Output power versus driver current at various temperatures for diode #1.

The spectral position and shape were measured at various temperatures and currents (Fig. 122.22). The output spectrum moved toward a longer wavelength at a rate of ~2 nm per °C of temperature increase and at a rate of ~2.5 nm per 100 mA of current increase.

Providing constant absorbed power and preventing target melting require irradiation with a highly stable spectrum that matches the D₂ absorption band. The 3160-nm-centered, 20-nm FWHM D₂ absorption band⁴ is well represented by a fourth-order super-Gaussian shown in Fig. 122.23 (red). The diode #1 spectra at various diode temperatures and driver currents were multiplied by the D₂ absorption curve to find

a relative power absorbed by D₂. After integration over the wavelength, the absorbed power, plotted in Fig. 122.24, showed optimal temperature and current settings for the maximum absorbed power –12°C and 1800 mA, which correspond to ~37 mW of absorbed power. Figure 122.23 shows spectral

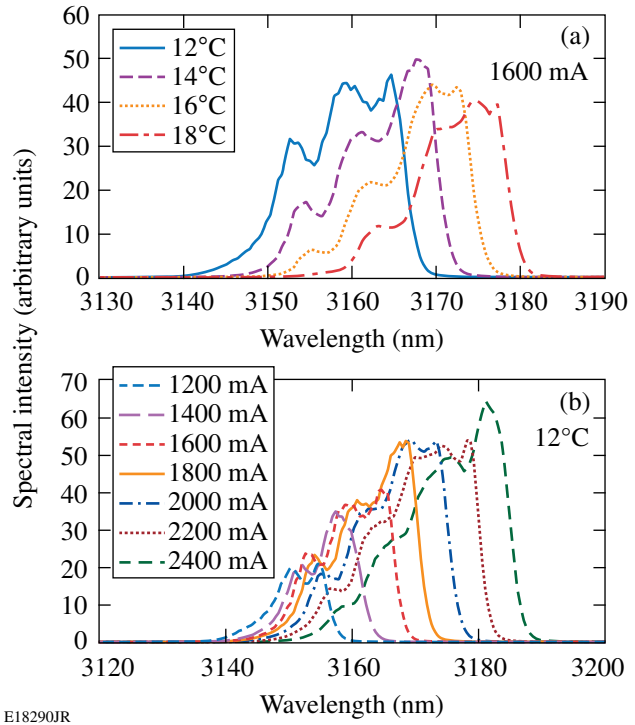


Figure 122.22
Output spectral shape and positions for various (a) temperatures and (b) currents for diode #1.

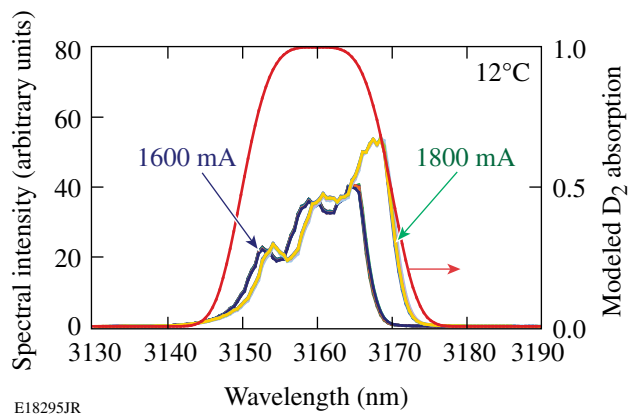
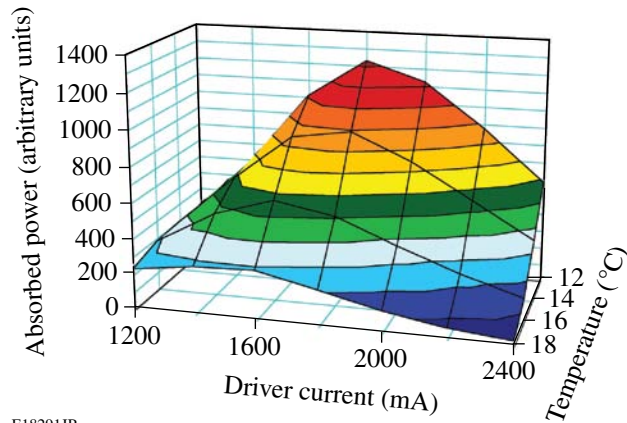


Figure 122.23
Diode #1 spectral stability at 1600- and 1800-mA driver currents. The D₂ absorption band is shown in red.



E18291JR

Figure 122.24
Diode #1 output power absorbed by the D₂ target at various diode temperatures and driver currents.

diode #1 stability at 12°C and 1600- and 1800-mA current settings. Plotted for each current setting are nine spectra that were taken at 15-min intervals over 2 h. Diode #1 represents high spectral stability and a compact spectral envelope over optimal temperature and current settings.

Conclusion

We demonstrated and characterized a highly spectrally stable, mid-IR, GaSb-based laser diode with a 3160-nm-centered, <20-nm FWHM spectrum and >35-mW output power at room temperature for cryogenic target layering at the Omega Laser Facility. A highly stable operation with output-power variations of ~1.3% rms has been demonstrated over 24 h. Future research will consist of optimizing the growing process to achieve consistent laser-diode performance with >100 mW of output power to meet the mid-IR layering-source requirement.

ACKNOWLEDGMENT

This work was supported by the U.S. Department of Energy Office of Inertial Confinement Fusion under Cooperative Agreement No. DE-FC52-08NA28302, the University of Rochester, and the New York State Energy Research and Development Authority. The support of DOE does not constitute an endorsement by DOE of the views expressed in this article. SUNY work was supported by US Air Force Office of Scientific Research under grant FA9550-08-1-0458.

REFERENCES

1. T. R. Boehly, D. L. Brown, R. S. Craxton, R. L. Keck, J. P. Knauer, J. H. Kelly, T. J. Kessler, S. A. Kumpan, S. J. Loucks, S. A. Letzring, F. J. Marshall, R. L. McCrory, S. F. B. Morse, W. Seka, J. M. Soures, and C. P. Verdon, *Opt. Commun.* **133**, 495 (1997).
2. T. C. Sangster, R. Betti, R. S. Craxton, J. A. Delettrez, D. H. Edgell, L. M. Elasky, V. Yu. Glebov, V. N. Goncharov, D. R. Harding, D. Jacobs-Perkins, R. Janezic, R. L. Keck, J. P. Knauer, S. J. Loucks, L. D. Lund, F. J. Marshall, R. L. McCrory, P. W. McKenty, D. D. Meyerhofer, P. B. Radha, S. P. Regan, W. Seka, W. T. Shmayda, S. Skupsky, V. A. Smalyuk, J. M. Soures, C. Stoeckl, B. Yaakobi, J. A. Frenje, C. K. Li, R. D. Petrasso, F. H. Séguin, J. D. Moody, J. A. Atherton, B. D. MacGowan, J. D. Kilkenny, T. P. Bernat, and D. S. Montgomery, *Phys. Plasmas* **14**, 058101 (2007).
3. D. R. Harding, D. D. Meyerhofer, T. C. Sangster, S. J. Loucks, R. L. McCrory, R. Betti, J. A. Delettrez, D. H. Edgell, L. M. Elasky, R. Epstein, V. Yu. Glebov, V. N. Goncharov, S. X. Hu, I. V. Igumenshchev, D. Jacobs-Perkins, R. J. Janezic, J. P. Knauer, L. D. Lund, J. R. Marciante, F. J. Marshall, D. N. Maywar, P. W. McKenty, P. B. Radha, S. P. Regan, R. G. Roides, W. Seka, W. T. Shmayda, S. Skupsky, V. A. Smalyuk, C. Stoeckl, B. Yaakobi, J. D. Zuegel, D. Shvarts, J. A. Frenje, C. K. Li, R. D. Petrasso, and F. H. Séguin, *J. Phys., Conf. Ser.* **112**, 022001 (2008).
4. A. Crane and H. P. Gush, *Can. J. Phys.* **44**, 373 (1966).
5. L. M. Elasky, D. J. Lonobile, W. A. Bittle, D. R. Harding, A. V. Okishev, and J. D. Zuegel, presented at the 15th Target Fabrication Specialists' Meeting, Glendon Beach, OR, 1–5 June 2003.
6. A. V. Okishev, D. Westerfeld, L. Shterengas, and G. Belenky, *Opt. Express* **17**, 15760 (2009).

A Reduced Particle-in-Cell Model for Two-Plasmon-Decay Instability

Introduction

Two-plasmon-decay (TPD) instability [the parametric decay of a laser (photon) into two Langmuir waves (plasmons)] has recently experienced renewed experimental and theoretical interest, largely based on recent experimental results obtained at the Omega Laser Facility.^{1–4} The TPD instability has been the subject of previous theoretical^{5,6} and experimental⁷ studies. Recent experiments using the OMEGA laser¹ have produced unambiguous evidence that TPD is driven in both spherical and planar targets. The diagnostic evidence includes the simultaneous emission of odd half-harmonic radiation and hard x rays.^{1,8} There is also some evidence^{2–4} that these hot electrons may be inhibiting the efficient implosion of spherical targets by preheating the core to a higher adiabat.

Although effort has been devoted to the linearized theory of the TPD instability in various regimes,^{5,6} it is clear, *a priori*, that a nonlinear theory is necessary to describe its evolution beyond the subpicosecond time to be relevant to experiments. This article is devoted to the development of a new theoretical tool for the study of the nonlinear development of TPD. It describes initial results from the implementation of the reduced particle-in-cell (RPIC) technique to treat the nonlinear evolution of TPD in homogeneous plasmas. The RPIC model is not limited to homogeneous plasma, and future work will include inhomogeneous plasma densities and flow velocities, which are present in experiments. The RPIC modeling and the closely related extended Zakharov (ZAK) modeling⁹ are useful tools for studying the nonlinear regimes of parametric instabilities. The RPIC and ZAK models have been previously applied to the nonlinear development of stimulated Raman scattering (SRS)¹⁰ and to the nonlinear development of the parametric decay instability (PDI).¹¹ In these studies, nonlinear processes such as the Langmuir decay instability (LDI) [the parametric decay of a Langmuir wave (LW) into another LW and an ion-acoustic wave (IAW)], Langmuir cavitation, and electron trapping have been observed to compete. Several predictions of this modeling have been experimentally verified.¹²

The RPIC model, while fully kinetic in regards to both electron and ion dynamics, shares certain features with the

reduced, fluid-like ZAK modeling.¹³ Both models represent the transverse fields, longitudinal fields, and density fields in terms of slowly varying envelopes of rapidly oscillating phase factors. This approach assumes a well-defined separation of time scales between the laser, LW, and IAW oscillations. This representation of field quantities stands in contrast with the standard particle-in-cell (PIC) technique in which the full-time variations are followed explicitly.¹⁴ In **Appendix B** (p. 103), a derivation of the extended Zakharov model directly from the RPIC equations of motion is presented. This derivation provides a direct theoretical connection between the kinetic RPIC and the fluid-like ZAK models. Furthermore, such a theoretical connection provides guidance on how one should proceed with *quantitative* comparison of the two models.

In the RPIC simulations, unique signatures of LDI are found that are suggestive of LDI as one of the primary saturation processes. Spectral signatures of LDI processes are strikingly similar, at least semi-quantitatively, to those found from ZAK modeling. In addition, the RPIC model also predicts heated-electron velocity distributions in the quasi-stationary nonlinear regime. Previous RPIC modeling has been extremely successful in modeling the nonlinear behavior of parametric instabilities involving the Langmuir decay instability, largely because RPIC eliminates the often unphysically high electron–ion collision rate present in explicit PIC codes, while at the same time allowing for the use of a modest number of simulation particles per simulation cell. For instance, for a plasma in quasi-thermodynamic equilibrium with $T_e/T_i \gg 1$, RPIC will preserve the temperature ratio perfectly over an extended time, whereas in standard PIC codes, this ratio will become unity prematurely because of the unphysically rapid electron–ion energy equilibration rate.¹⁵ This is problematic when ion modes are involved, such as in LDI, since the IAW damping rate is sensitive to this ratio (cf. Ref. 16). Additional effects expected from the strong electron–ion collisions (even when $T_{e0} = T_{i0}$) include unphysically large collisional damping of LW’s and IAW’s. Elimination of unphysical electron–ion collisions makes it possible for RPIC simulations to operate with fewer particles per simulation cell than standard PIC codes. It is important to

observe that the earliest application of PIC codes to TPD by Langdon *et al.*⁵ and more recently by Yan *et al.*¹⁴ observed a high level of ion-density fluctuations. It is not clear in retrospect that these can be interpreted as resulting from IAW fluctuations excited by LDI as found in this work.

In previous work using ZAK modeling⁹ it was found, among other things, that LDI produces a distinct, rich Fourier spectrum of electron- and ion-density fluctuations. Furthermore, this modeling provided an explanation for the well-known problem that the primary, i.e., most linearly unstable, TPD Langmuir waves cannot couple locally to the (observed) radiation at $3\omega_0/2$, where ω_0 is the laser frequency. In Russell *et al.*,¹⁷ it was shown that there is an efficient local coupling of the secondary LDI-produced LW's to the $3\omega_0/2$ emission and this coupling in turn produced, in an inhomogeneous plasma, a distinctive double-peaked $3\omega_0/2$ frequency spectrum. RPIC has the advantage that the envelope fields can be used directly to compute the currents for the $3\omega_0/2$ radiation, as was done in Russell *et al.*¹⁷ and also more recently for the $\omega_0/2$ radiation current as shown in DuBois *et al.*¹⁸ The latter application of RPIC to $\omega_0/2$ radiation is proposed for future work.

The article is organized as follows: (1) The equations for the physical model underlying RPIC are discussed. This involves expressing the electromagnetic vector potential, the longitudinal scalar potential, and the plasma density in temporal envelope representations (the primary objective of the RPIC formulation is to eliminate the laser time scale from the electron equation of motion and the laser and LW time scales from the ion equation of motion). (2) A sketch of the derivation of the RPIC model for TPD is given, with the details provided in **Appendix A**, p. 101. An important element in this derivation (as in previous implementations of RPIC¹⁵) is the closure of the model set of equations with an auxiliary electron equation of state. (3) Results of both RPIC and ZAK simulations of TPD in a homogeneous plasma are presented (including the standard problem of a single coherent laser beam) along with simulations of oblique overlapped beams propagating at angles of $\pm 23^\circ$ relative to the x axis common in OMEGA geometry.¹ Finally, a summary and conclusions are presented.

Physical Model

The vector potential, scalar potential, and electron density are written as¹⁹

$$\mathbf{A}(\mathbf{x}, t) = \frac{1}{2}[\mathbf{a}_0 \exp(-i\omega_0 t) + \text{c.c.}], \quad (1)$$

$$\phi(\mathbf{x}, t) = \phi_S + \frac{1}{2}[\phi_F \exp(-i\omega_{LW} t) + \text{c.c.}], \quad (2)$$

$$n(\mathbf{x}, t) = n_S + \frac{1}{2}[n_F \exp(-i\omega_{LW} t) + \text{c.c.}], \quad (3)$$

where ω_0 is the laser frequency and ω_{LW} is the carrier frequency of the LW density and electric-field perturbations. In the RPIC model, ω_{LW} is an input parameter and is typically chosen to be $\omega_{LW} = \omega_{pe0}$ (where $\omega_{pe0}^2 = 4\pi e^2 n_{e0}/m_e$), e is the unsigned electronic charge, n_{e0} is the electron number density, and m_e is the mass of an electron. The subscripts S and F refer to the slow (ion-acoustic wave and profile modification) and fast (Langmuir wave) time scales, respectively. It is assumed that the density is at, or near, quarter-critical density so that $\omega_0 \approx 2\omega_{LW}$. The model is also restricted to two spatial dimensions (x, y), with z the ignorable coordinate.

The goal of the RPIC formulation is to eliminate the laser time scale from the electron equations of motion and the laser and Langmuir wave time scales from the ion equations of motion. The particle velocities and positions in RPIC, by necessity, are measured in an oscillating and, therefore, non-inertial frame.

1. Single-Particle Equation in an Oscillating Frame

The nonrelativistic equation of motion for the single-particle velocity $\mathbf{u} [= u_x(x, y)\hat{\mathbf{x}} + u_y(x, y)\hat{\mathbf{y}}]$ is given by

$$m \frac{d\mathbf{u}}{dt} = q \left(-\nabla \phi - \frac{1}{c} \frac{\partial \mathbf{A}}{\partial t} + \frac{\mathbf{u} \times \nabla \times \mathbf{A}}{c} \right). \quad (4)$$

Rewriting the above equation with the change of variable $\mathbf{u} \equiv \tilde{\mathbf{u}} - q\mathbf{A}/mc$, one obtains

$$\begin{aligned} m \left(\frac{d\tilde{\mathbf{u}}}{dt} - \frac{q}{mc} \frac{\partial \mathbf{A}}{\partial t} - \frac{q}{mc} \mathbf{u} \cdot \nabla \mathbf{A} \right) \\ = q \left(-\nabla \phi - \frac{1}{c} \frac{\partial \mathbf{A}}{\partial t} + \frac{\mathbf{u} \times \nabla \times \mathbf{A}}{c} \right) \end{aligned} \quad (5a)$$

and

$$\begin{aligned} m \frac{d\tilde{\mathbf{u}}}{dt} = -\nabla \left(q\phi + \frac{q^2}{2mc^2} \mathbf{A} \cdot \mathbf{A} \right) \\ + \frac{q}{c} (\tilde{\mathbf{u}} \times \nabla \times \mathbf{A} + \tilde{\mathbf{u}} \cdot \nabla \mathbf{A}). \end{aligned} \quad (5b)$$

Note that the operators ∇ and d/dt in the above equation are measured in the laboratory frame. The above equation can be written in the oscillating frame $(\tilde{\mathbf{x}}, \tilde{t})$, which moves with velocity $-q\mathbf{A}/mc$ relative to the lab frame (\mathbf{x}, t) by using the following coordinate transformation:

$$\mathbf{u} = \tilde{\mathbf{u}} - \frac{q\mathbf{A}(\mathbf{x}, t)}{mc}, \quad (6)$$

$$\mathbf{x} = \tilde{\mathbf{x}} - \frac{q}{mc} \int_0^t \mathbf{A}[\mathbf{x}(\tau), \tau] d\tau, \quad (7)$$

$$t = \tilde{t}. \quad (8)$$

The various partial derivatives required for the transformation $(\mathbf{x}, t) \rightarrow (\tilde{\mathbf{x}}, \tilde{t})$ are

$$\frac{\partial \tilde{t}}{\partial t} = 1, \quad (9)$$

$$\frac{\partial \tilde{t}}{\partial \mathbf{x}} = 0, \quad (10)$$

$$\frac{\partial \tilde{\mathbf{x}}}{\partial t} = \frac{q\mathbf{A}}{mc}, \quad (11)$$

$$\frac{\partial \tilde{\mathbf{x}}}{\partial \mathbf{x}} = \mathbf{I}. \quad (12)$$

By using the chain rule and the partial derivatives shown above, one obtains

$$\frac{\partial}{\partial t} = \frac{\partial \tilde{t}}{\partial t} \frac{\partial}{\partial \tilde{t}} + \frac{\partial \tilde{\mathbf{x}}}{\partial t} \cdot \frac{\partial}{\partial \tilde{\mathbf{x}}} = \frac{\partial}{\partial \tilde{t}} + \frac{q\mathbf{A}}{mc} \cdot \frac{\partial}{\partial \tilde{\mathbf{x}}}, \quad (13)$$

$$\frac{\partial}{\partial \mathbf{x}} = \frac{\partial \tilde{t}}{\partial \mathbf{x}} \frac{\partial}{\partial \tilde{t}} + \frac{\partial \tilde{\mathbf{x}}}{\partial \mathbf{x}} \cdot \frac{\partial}{\partial \tilde{\mathbf{x}}} = \frac{\partial}{\partial \tilde{\mathbf{x}}}. \quad (14)$$

The transformation from (\mathbf{x}, t) to $(\tilde{\mathbf{x}}, \tilde{t})$ proceeds as

$$\begin{aligned} \frac{d}{dt} &= \frac{\partial}{\partial t} + \mathbf{u} \cdot \frac{\partial}{\partial \mathbf{x}}, \\ &= \frac{\partial}{\partial \tilde{t}} + \frac{q\mathbf{A}}{mc} \cdot \frac{\partial}{\partial \tilde{\mathbf{x}}} + \mathbf{u} \cdot \frac{\partial}{\partial \tilde{\mathbf{x}}}, \\ &= \frac{\partial}{\partial \tilde{t}} + \tilde{\mathbf{u}} \cdot \frac{\partial}{\partial \tilde{\mathbf{x}}}, \\ \frac{d}{dt} &= \frac{d}{d\tilde{t}}. \end{aligned} \quad (15)$$

Equation (5) can now be rewritten as

$$\begin{aligned} m \frac{d\tilde{\mathbf{u}}}{d\tilde{t}} &= -\tilde{\nabla} \left(q\phi + \frac{q^2}{2mc^2} \mathbf{A} \cdot \mathbf{A} \right) \\ &+ \frac{q}{c} [\tilde{\nabla} (\tilde{\mathbf{u}} \cdot \mathbf{A}) - \mathbf{A} \times \tilde{\nabla} \times \tilde{\mathbf{u}} - \mathbf{A} \cdot \tilde{\nabla} \tilde{\mathbf{u}}], \end{aligned} \quad (16)$$

$$\frac{d\tilde{\mathbf{x}}}{d\tilde{t}} = \tilde{\mathbf{u}}, \quad (17)$$

where the vector identity

$$\tilde{\nabla} (\tilde{\mathbf{u}} \cdot \mathbf{A}) = \tilde{\mathbf{u}} \times \tilde{\nabla} \times \mathbf{A} + \mathbf{A} \times \tilde{\nabla} \times \tilde{\mathbf{u}} + \mathbf{A} \cdot \tilde{\nabla} \tilde{\mathbf{u}} + \tilde{\mathbf{u}} \cdot \tilde{\nabla} \mathbf{A}$$

has been used. Note that Eqs. (16) and (17), which are valid for both electrons and ions, are exact.

2. Fluid Equations

The electron fluid momentum equation is obtained by integrating Eq. (16) (the single-particle equation of motion) over the distribution function, writing explicitly $d/d\tilde{t} \equiv \partial/\partial\tilde{t} + \tilde{\mathbf{U}} \cdot \tilde{\nabla}$,

$$\begin{aligned} mn \left(\frac{\partial \tilde{\mathbf{U}}}{\partial \tilde{t}} + \tilde{\mathbf{U}} \cdot \tilde{\nabla} \tilde{\mathbf{U}} \right) &= -n \tilde{\nabla} \left(q\phi + \frac{q^2}{2mc^2} \mathbf{A} \cdot \mathbf{A} \right) \\ &+ \frac{qn}{c} [\tilde{\nabla} (\tilde{\mathbf{U}} \cdot \mathbf{A}) - \mathbf{A} \times \tilde{\nabla} \times \tilde{\mathbf{U}} - \mathbf{A} \cdot \tilde{\nabla} \tilde{\mathbf{U}}] - \tilde{\nabla} p, \end{aligned} \quad (18)$$

where n , $\tilde{\mathbf{U}}$, and p are the electron density, fluid velocity, and fluid pressure in the oscillating frame. For an isotropic background electron-velocity distribution f ,

$$n \equiv \int f(|\tilde{\mathbf{u}}|) d^3\tilde{\mathbf{u}},$$

$$n\tilde{\mathbf{U}} \equiv \int \tilde{\mathbf{u}} f(|\tilde{\mathbf{u}}|) d^3\tilde{\mathbf{u}},$$

$$p \equiv \int m|\tilde{\mathbf{u}} - \tilde{\mathbf{U}}|^2 f(|\tilde{\mathbf{u}}|) d^3\tilde{\mathbf{u}}.$$

In the special case of an isotropic Maxwellian distribution function, $p = n_e T_e$.

The RPIC Model

The derivation of the RPIC model for TPD can be divided into three separate tasks: First, the fluid momentum equation [Eq. (18)] is averaged over the fast laser time scale to derive an electron equation of state, which itself provides closure for the RPIC model. Second, Eq. (18) is also used to derive the transverse electron current, which provides the driving sources in the nonlinear Schrödinger equation for the incident EM waves. Third, the single-particle equation [Eq. (16)] is averaged over the fast laser time scale to derive a reduced-description, single-particle equation of motion (only a summary of the RPIC model is given below; detailed derivations of these equations can be found in **Appendix A**, p. 101).

The electrons are advanced using the following reduced-description equations of motion:

$$\begin{aligned} m_e \frac{d\tilde{\mathbf{u}}_e}{d\tilde{t}} &\approx -e\mathbf{E} - \frac{e^2}{4m_e c^2} \tilde{\nabla} |\mathbf{a}_0|^2 \\ &- \frac{e^2}{4cm_e \omega_{LW}} \left\{ i \tilde{\nabla} (\mathbf{E}_F^* \cdot \mathbf{a}_0) \exp[-i(\omega_0 - \omega_{LW})\tilde{t}] + \text{c.c.} \right\} \\ &- \frac{e^2}{4cm_e \omega_{LW}} \left\{ -i(\mathbf{a}_0 \cdot \tilde{\nabla}) \mathbf{E}_F^* \exp[-i(\omega_0 - \omega_{LW})\tilde{t}] + \text{c.c.} \right\}, \end{aligned} \quad (19)$$

$$\frac{d\tilde{\mathbf{x}}_e}{d\tilde{t}} = \tilde{\mathbf{u}}_e,$$

$$\mathbf{E} \equiv -\tilde{\nabla} \phi, \quad (20)$$

$$\mathbf{E}_F \equiv -\tilde{\nabla} \phi_F,$$

and the ions by

$$m_i \frac{d\tilde{\mathbf{u}}_i}{d\tilde{t}} = Z_i e \mathbf{E}_S - \frac{Z_i^2 e^2}{4m_i c^2} \tilde{\nabla} |\mathbf{a}_0|^2,$$

$$\frac{d\tilde{\mathbf{x}}_i}{d\tilde{t}} = \tilde{\mathbf{u}}_i,$$

$$\mathbf{E}_S \equiv -\tilde{\nabla} \phi_S. \quad (21)$$

Here, Z_i and m_i are the ion charge state and ion mass, respectively. The electron and ion charge densities are interpolated from the particle data onto the computational mesh:

$$-en_e(\tilde{\mathbf{x}}, \tilde{t}) = \sum_{p \in e} q_p S[\tilde{\mathbf{x}} - \tilde{\mathbf{x}}_p(\tilde{t})], \quad (22)$$

$$eZ_i n_i(\tilde{\mathbf{x}}, \tilde{t}) = \sum_{p \in i} q_p S[\tilde{\mathbf{x}} - \tilde{\mathbf{x}}_p(\tilde{t})]. \quad (23)$$

The particle shape function $S(\mathbf{x})$ is the bi-quadratic B-spline of compact supports Δx and Δy (Δx and Δy are the discrete grid spacings of the computational mesh).¹⁵ The symbols $\sum_{p \in e}$ and $\sum_{p \in i}$ denote summations over the finite-size electron particles and finite-size ion particles, respectively. The electrostatic potentials ϕ , ϕ_S , and ϕ_F are obtained by solving the Poisson equation in conjunction with the auxiliary electron equation of state:

$$\tilde{\nabla}^2 \phi = 4\pi e \left(n_e - \sum_i Z_i n_i \right), \quad (24)$$

$$\tilde{\nabla}^2 \phi_S = 4\pi e \left(n_{eS} - \sum_i Z_i n_i \right), \quad (25)$$

$$\alpha(t) = e\phi_S - \frac{e^2}{4m_e \omega_{LW}^2} |\mathbf{E}_{\text{eff}}|^2 - \frac{e^2}{4m_e^2 c^2} |\mathbf{a}_0|^2 - f(\gamma, n_{eS}), \quad (26)$$

where

$$f(\gamma, n_{eS}) = \begin{cases} T_{e0} \ln(n_{eS}/n_{e0}) & \text{for } \gamma = 1, \\ T_{e0} \left(\frac{\gamma}{\gamma - 1} \right) (n_{eS}/n_{e0})^{\gamma - 1} & \text{otherwise.} \end{cases} \quad (27)$$

$$\mathbf{E}_{\text{eff}} \equiv \mathbf{E}_F - \frac{e}{2im_e c \omega_{\text{LW}}} \exp(-i\Delta\omega\tilde{t}) \left[\tilde{\nabla} \left(\mathbf{E}_F^* \cdot \mathbf{a}_0 \right) + \mathbf{a}_0 \cdot \tilde{\nabla} \mathbf{E}_F^* \right], \quad (28)$$

$$\phi_F \approx \exp(i\omega_{\text{LW}}\tilde{t}) \left[-\frac{1}{i\omega_{\text{LW}}} \frac{\partial\phi}{\partial\tilde{t}} + (\phi - \phi_S) \right], \quad (29)$$

$$\Delta\omega \equiv \omega_0 - 2\omega_{\text{LW}}. \quad (30)$$

Here, α is the constant of integration chosen to satisfy global charge conservation and γ is the ratio of specific heats (isothermal electrons: $\gamma = 1$; adiabatic electrons: $\gamma = 5/3$), and n_{e0} is the background electron number density. Finally, the incident EM field is advanced self-consistently in time by solving the nonlinear Schrödinger equation

$$\begin{aligned} & i \left(\frac{2\omega_0}{c^2} \right) \frac{\partial \mathbf{a}_0}{\partial \tilde{t}} + \tilde{\nabla}^2 \mathbf{a}_0 + \frac{1}{c^2} \left(\omega_0^2 - \frac{4\pi e^2 n_S}{m_e} \right) \mathbf{a}_0 \\ & = -\frac{4\pi}{c} \tilde{\nabla} \chi_0 + \frac{4\pi e^2 n_{eF}}{2im_e c \omega_{\text{LW}}} \tilde{\mathbf{E}}_{\text{eff}} \exp(i\Delta\omega\tilde{t}), \end{aligned} \quad (31)$$

where

$$\nabla^2 \chi_0 = -\nabla \cdot \mathbf{J}_0, \quad (32)$$

$$\mathbf{J}_0 = -\frac{e^2 n_{eS} \mathbf{a}_0}{m_e c} - \frac{e^2 n_{eF}}{2im_e \omega_{\text{LW}}} \mathbf{E}_{\text{eff}} \exp(i\Delta\omega\tilde{t}). \quad (33)$$

The projection operator in Eq. (32) ensures that the gauge condition $\nabla \cdot \mathbf{a}_0 = 0$ is preserved.

Equations (19)–(33) are solved self-consistently on a rectangular simulation domain with $0 \leq x \leq x_{\text{max}}$ and $0 \leq y \leq y_{\text{max}}$, consisting of $N_x \times N_y$ computational cells of equal size. The EM wave of the laser is permitted to propagate along an arbitrary direction in the x – y plane and is linearly polarized (normal to the direction of wave propagation). The field boundary conditions are periodic in the y direction but are aperiodic in the x direction with $\phi(x=0,y) = \phi(x=x_{\text{max}},y) = 0$. At all boundary

surfaces, i.e., $x=0$, $x=x_{\text{max}}$, $y=0$, and $y=y_{\text{max}}$, particles leaving the domain are absorbed (removed), and new particles are injected consistent with a Maxwellian bath (with a temperature given by the plasma's initial state) surrounding the simulation domain (see Fig. 122.25). Modification of the particle boundary conditions (for example, to account for recirculation of hot electrons²⁰) is an important problem for future research, as discussed in **Summary and Conclusions** (p. 101). Finally, the RPIC code is fully parallel, based on the Message Passing Interface (MPI),¹⁵ and has a number of built-in spectral, hot-electron, and spatial diagnostics.

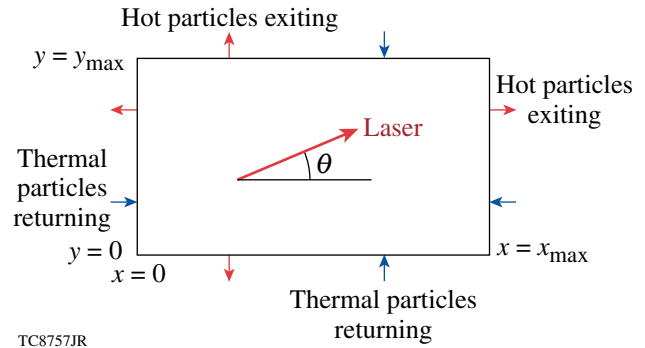


Figure 122.25

The two-dimensional simulation geometry. A Maxwellian bath of electrons at temperature T_{e0} is assumed to surround the rectangular simulation domain. The laser light can be specified as multiple plane-wave sources, propagating at arbitrary angles θ to the x direction.

Simulation Results

Three sets of simulations are presented in this section. For each set, two simulations were performed with identical parameters on the domain $x_{\text{max}} = 20 \mu\text{m}$, $y_{\text{max}} = 10 \mu\text{m}$, and consisting of $N_x \times N_y = 2048 \times 1024$ computational cells of equal size (see Fig. 122.25). In all cases the incident laser light had a vacuum wavelength of $\lambda_0 = 0.351 \mu\text{m}$ and the plasma was fully ionized hydrogen ($Z = 1$). The two simulations highlight the qualitative similarities and quantitative differences between the kinetic RPIC model [Eqs. (19)–(33)] and its (fluid) limiting form that has been derived in Appendix B [Eqs. (B40)–(B41)]. The limiting form, given by Eqs. (B40)–(B41), is solved using the existing extended-Zakharov code “ZAK,” which is described in DuBois *et al.*⁹ The equations solved by ZAK are advanced in time using split steps: spatial gradients are computed in configuration space, and Landau damping of LW’s and IAW’s, which are k dependent, are computed in Fourier space. These results, which are by no means exhaustive, are presented to illustrate the utility and capability of the RPIC code and to motivate further studies.

The first simulation set investigated the decay of a single-plane electromagnetic (EM) wave propagating in the positive x direction. Pump depletion was not considered, i.e., $\mathbf{a}_0 = a_{00}\hat{\mathbf{y}}\exp(ik_0x)$, where a_{00} is a constant [Eq. (31) is not solved]. The pump laser had an intensity of $I_0 = 2 \times 10^{15}$ W/cm², corresponding to a linear (amplitude) growth rate of $\gamma_{\text{TPD}}/\omega_{\text{pe}0} \simeq 6.4 \times 10^{-3}$, which is $50\times$ above the collisional threshold (the collision frequency $\nu_{e0}/\omega_{\text{pe}0}$ was taken to be $\sim 9.1 \times 10^{-4}$). The plasma was of uniform initial density $n_{e0}/n_c = 0.23$ [where $n_c = m_e\omega_0^2/(4\pi e^2)$ is the critical density] and the electron- and ion-plasma temperatures were $T_{e0} = 4$ keV and $T_{i0} = 2$ keV, respectively. This electron temperature was about a factor of 2 higher than typically found in OMEGA experiments and was chosen because the spectral components (e.g., due to LDI) were more widely separated because of the large value of $k\lambda_{\text{De}}$, where $\lambda_{\text{De}} \equiv v_{\text{the}}/\omega_{\text{pe}0}$ is the electron Debye length and $v_{\text{the}} \equiv (T_{e0}/m_e)^{1/2}$ is the electron thermal speed. The electrons and ions were each represented by 16 particles per computational cell. The discrete time step was $\omega_{\text{pe}0}\Delta t = 0.1$ or, alternatively, $\Delta t \approx 3.88 \times 10^{-5}$ ps.

Figure 122.26 shows, from strictly linear-fluid considerations, the locations of frequency- and wave-number-matched LW's (circle),

$$\left(k_x\lambda_{\text{De}} - \frac{1}{2}k_0\lambda_{\text{De}}\right)^2 + (k_y\lambda_{\text{De}})^2 = \kappa^2, \quad (34)$$

and the locations of maximum TPD growth (hyperbola),

$$\left(k_x\lambda_{\text{De}} - \frac{1}{2}k_0\lambda_{\text{De}}\right)^2 - (k_y\lambda_{\text{De}})^2 = \left(\frac{1}{2}k_0\lambda_{\text{De}}\right)^2. \quad (35)$$

Here κ is defined as

$$\kappa \equiv \sqrt{\frac{1}{2}\Omega - \left(\frac{1}{2}k_0\lambda_{\text{De}}\right)^2}, \quad \text{with } \Omega \equiv \frac{2}{3}\left(\frac{\omega_0}{\omega_{\text{pe}0}} - 2\right), \quad (36)$$

and $k_0 = \omega_0/c\sqrt{1 - n_{e0}/n_c}$ is the laser light's wave number in the plasma. The intersections of the circle and the hyperbola are locations where TPD-produced LW's are expected to be the most intense. In Fig. 122.26, the two linear modes indicated by the label "1" and located at

$$\mathbf{k}\lambda_{\text{De}} \equiv (k_x\lambda_{\text{De}}, k_y\lambda_{\text{De}}) = (0.20, \pm 0.087)$$

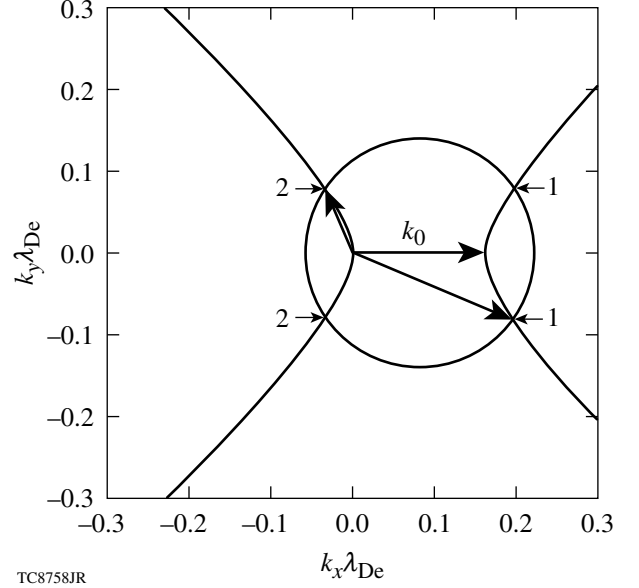


Figure 122.26

The expected wave numbers for plasmons occurring in the TPD instability of a single pump laser propagating in the x direction with parameters $T_{e0} = 4$ keV and $n_e/n_c = 0.23$. The circle represents all possible wave-number- and frequency-matched decay LW's [Eq. (34)], and the hyperbola represents the locations in k space where the TPD growth rate is maximized [Eq. (35)]. The intersections of the circle and the hyperbolae are the spectral locations where TPD LW's are expected to occur. Labels 1 and 2 denote the forward propagating (blue-shifted) and backward propagating (red-shifted) LW's, respectively.

correspond to forward-propagating, blue-shifted LW's and the two modes labeled "2" at $\mathbf{k}\lambda_{\text{De}} = (-0.038, \pm 0.087)$ correspond to backward-propagating, red-shifted plasmons.

Figure 122.27 shows the normalized LW spectra

$$W_k \equiv \frac{x_{\text{max}}}{2\pi} \frac{y_{\text{max}}}{2\pi} \frac{|E_{\text{LW}}(k_x, k_y)|^2}{4\pi n_{e0} T_{e0}},$$

time-averaged over the full 20-ps duration of the simulation, for both the (a) RPIC and (b) ZAK models. The RPIC and ZAK results are displayed on the same color scale to facilitate a direct comparison. The RPIC and ZAK results exhibit good qualitative similarity, with the dominant spectral features falling at exactly the same location in k space. The labels 1 and 2 in Fig. 122.27 refer to the same unstable modes as were identified previously in Fig. 122.26. In addition, two LDI steps of the blue-shifted plasmons are seen in the RPIC calculations [labeled 1' and 1'', respectively, in Fig. 122.27(a)], while only one LDI step is clearly seen in the ZAK calculations [labeled 1' in Fig. 122.27(b)]. As a measure of the level of laser-induced LW

excitation, the integrated value $W \equiv \int d\mathbf{k} W_k$ is defined, where the integration is carried out over the disk $|\mathbf{k}\lambda_{De}| \leq 0.25$. For the RPIC simulation $W = 1.0 \times 10^{-1}$, while the ZAK simulation

gives the almost $2\times$ stronger value of $W = 1.8 \times 10^{-1}$. However, the peak values in the RPIC simulation are narrower and more intense than for the ZAK case.

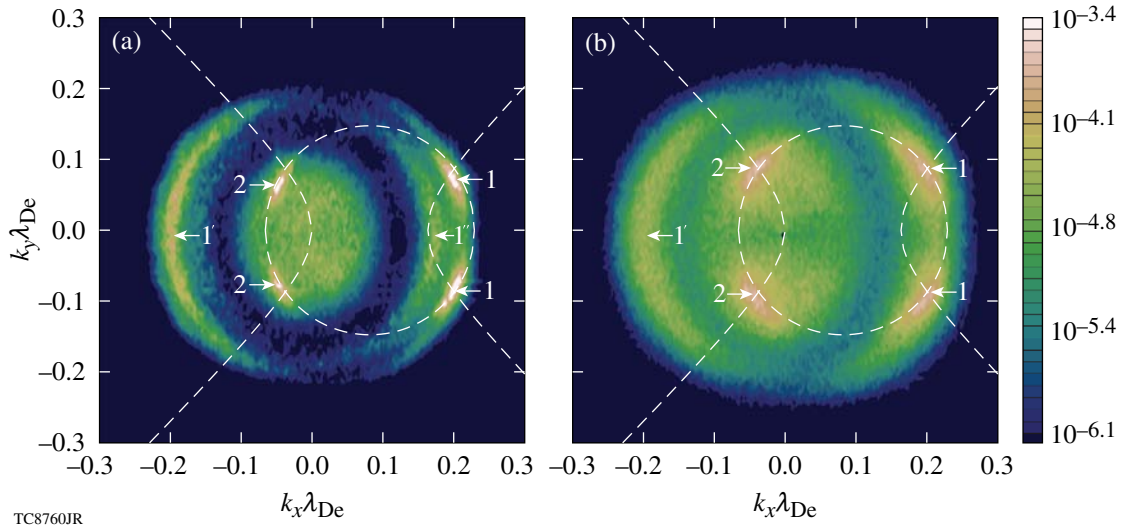


Figure 122.27

The time-averaged LW spectral intensity W_k is shown for both (a) RPIC and (b) ZAK simulations for a single plane-wave pump light wave and the parameters $T_{e0} = 4$ keV and $n_{e0}/n_c = 0.23$. Labels 1 and 2 denote the forward-propagating (blue-shifted) and backward-propagating (red-shifted) TPD LW's, respectively. Label 1' indicates that the LW's wave corresponding to the first LDI step of blue TPD plasmon (1), which is evident in both the RPIC and ZAK calculations. The second decay step (1'') can be seen in (a).

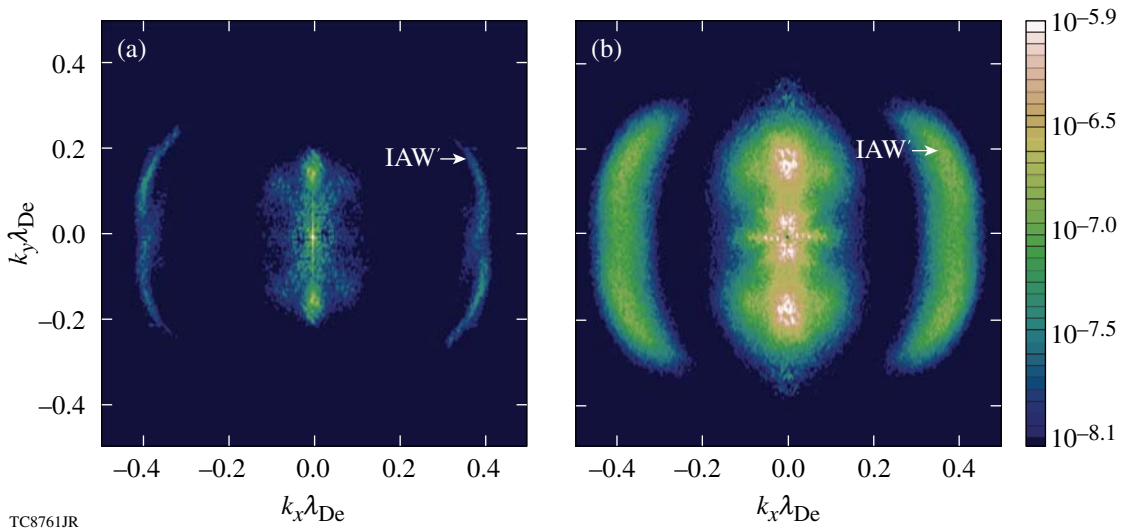


Figure 122.28

The time-averaged IAW density fluctuation spectrum $|\delta N_k|^2$ is shown for (a) RPIC and (b) ZAK simulations of TPD driven by a single plane-wave pump with the parameters $T_{e0} = 4$ keV and $n_{e0}/n_c = 0.23$. IAW's corresponding to the first LDI step of the blue TPD plasmon are evident in both sets of simulations, although narrower and weaker in (a) than in (b), and are indicated by the label IAW'.

The corresponding IAW spectra

$$|\delta N_k|^2 \equiv \frac{x_{\max}}{2\pi} \frac{y_{\max}}{2\pi} \left| \delta n_{eS}(k_x, k_y) / n_{e0} \right|^2$$

are shown in Fig. 122.28. Ion-acoustic waves caused by LDI are clearly visible in both the RPIC and ZAK simulations and are labeled IAW'. The IAW from the second LDI step is very weak and difficult to identify in the displayed spectrum. The integrated LDI density perturbations are estimated by the quantity $\mathcal{N}_{\text{LDI}} \equiv \int d\mathbf{k} |\delta N_k|^2$. In this case, the domain of integration is the annulus $0.3 \leq |\mathbf{k}\lambda_{\text{De}}| \leq 0.5$. The choice of domain is intended to avoid including the structures in $|\delta N_k|^2$ found near $k_x = 0$ that arise from the beating of pairs of LW's with equal and opposite values of k_y and equal values of k_x . Using this criterion, RPIC gives $\mathcal{N}_{\text{LDI}} = 1.4 \times 10^{-4}$, whereas ZAK gives $\mathcal{N}_{\text{LDI}} = 5.3 \times 10^{-4}$. If it is assumed that the ponderomotive drive for the IAW's is proportional to \mathcal{W} , comparing the \mathcal{N}_{LDI} values would indicate that LDI plays a relatively smaller role in the nonlinear saturation in RPIC. Kinetic saturation mechanisms, such as trapping of electrons (and ions) in the LW's (and IAW's) in the case of RPIC, cannot be ruled out. All of the simulations reported here reach saturation after about 15 ps, which is also the time at which LDI features become well established in the spectra.

In the second simulation set, two overlapping incident laser beams, again plane waves, were prescribed at angles θ relative to the x axis of $\theta_{\pm} = \pm 23^\circ$. This type of crossed-beam geometry is generic to direct-drive ICF, where large numbers of beams are overlapped to provide uniform illumination of the target (the precise angles of $\theta_{\pm} = \pm 23^\circ$ are specific to OMEGA¹). The individual beam intensity $I_0 = 1 \times 10^{15}$ W/cm² was chosen such that the crossed-beam overlapped intensity was the same as the previous single-beam case, shown in Figs. 122.26–122.28, and all other parameters were identical, with the exception of the plasma density, which was slightly increased to $n_{e0}/n_c = 0.231$ (the reason for choosing this particular density is given below).

The locations of the most linearly unstable TPD-produced LW waves, for an arbitrary irradiation angle in a homogeneous plasma, can be obtained simply by rotating Eqs. (34) and (35) in k space (see **Appendix C**, p. 109). In general, for two overlapping beams there are eight distinct LW's since each beam will produce four LW's (as previously shown in Fig. 122.26): two corresponding to the forward (blue-shifted) plasmons and two corresponding to the backward (red-shifted) plasmons. In the case of beams symmetrically oriented about the x axis, for a

given set of plasma parameters (T_{e0} and $0.2 \lesssim n_{e0}/n_c \lesssim 0.25$), a particular beam angle θ exists in which two of the forward (blue-shifted) plasmons are degenerate, or common. This overlap, or sharing of a common plasmon, allows for the cooperative nonlinear interaction between the two crossed beams. Conversely, for a prescribed beam angle θ and electron temperature T_{e0} , a particular density n_{e0}/n_c exists that will result in degenerate forward plasmons. In monotonic inhomogeneous plasmas, a location will always exist along the beam path where this degeneracy condition is satisfied, but in homogeneous simulations it must be specially selected, which is the choice made here. The relationship between the beam angle θ , electron density n_{e0}/n_c , and electron temperature T_{e0} for degeneracy to occur is derived in **Appendix C** and is given by Eq. (C8). For an electron temperature $T_{e0} = 4$ keV and angles $\theta_{\pm} = \pm 23^\circ$, Eq. (C8) yields degenerate forward plasmons for an electron density of $n_{e0}/n_c = 0.231$. This is depicted graphically in Fig. 122.29, where two sets of circles and hyperbolae are shown: (1) solid lines for the laser propagating at $\theta_+ (= +23^\circ)$ and (2) dashed lines for the laser propagating at $\theta_- (= -23^\circ)$. As before, the intersections of the circle and the hyperbola for

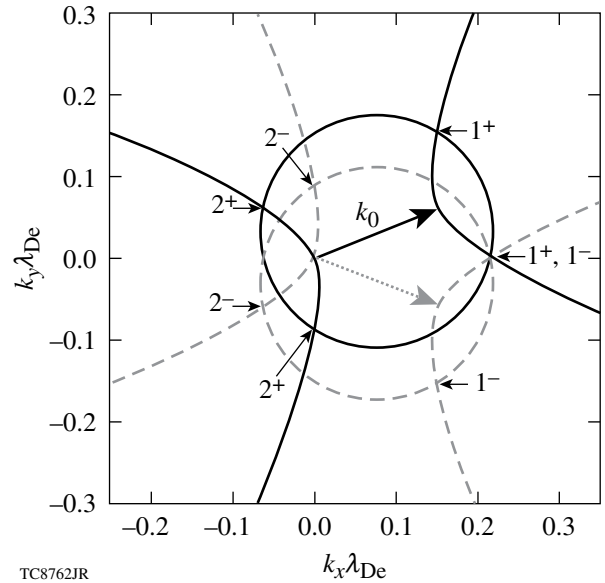


Figure 122.29

Expected wave numbers for TPD LW's resulting from the decay of two EM plane waves propagating with angles $\theta = \pm 23^\circ$ with respect to the x axis (the parameters are $T_e = 4$ keV and $n_e/n_c = 0.231$). Points 1^+ (1^-) and 2^+ (2^-) denote the expected locations of the red- and blue-shifted plasmons from the EM wave propagating with angle $\theta = +23^\circ$ (-23°), respectively. The solid (dashed) circle [Eq. (C1)] represents all frequency- and wave-number-matched LW's for the $\theta = +23^\circ$ (-23°) beam. Likewise, the solid (dashed) hyperbolae [Eq. (C4)] show the maximum growth rate for the $\theta = +23^\circ$ (-23°) beam. The blue-shifted plasmons 1^+ and 1^- are degenerate.

each respective laser beam are the spectral locations where LW's are expected to be observed. These are labeled as in Fig. 122.26, with the superscripts \pm corresponding to decays of the beam incident at angle θ_{\pm} . The on-axis, blue-shifted LW's of both beams (1^+ and 1^-) are degenerate—the common LW wave. This has a wave number $k\lambda_{De} \approx (0.23, 0.0)$ and a phase velocity $v_{\phi}/v_{the} \approx 4.7$. This notion of a “shared” plasma wave,

which can generally occur in cases of multiple-beam irradiation where a symmetry exists, has been discussed by Short *et al.*²¹

Figures 122.30 and 122.31 show the LW spectral intensity W_k and IAW density spectra $|\delta N_k|^2$, respectively, time averaged over the full 20-ps duration of the simulation. Although the RPIC and ZAK results are not in exact quantitative agreement,

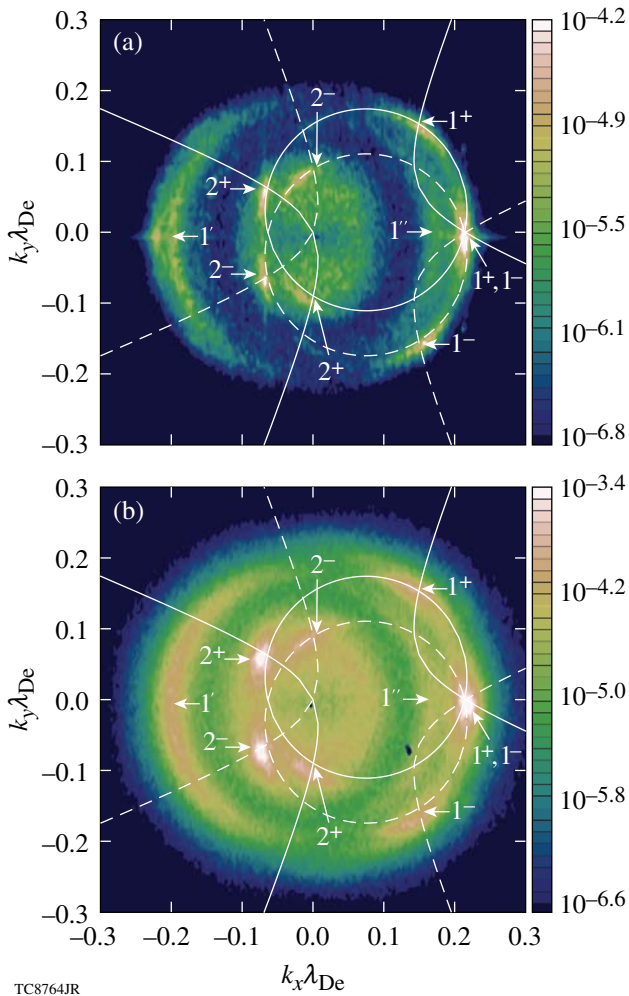


Figure 122.30

The time-averaged LW spectrum W_k is shown for both (a) RPIC and (b) ZAK simulations for the parameters $T_e = 4$ keV and $n_e/n_c = 0.231$. The pump consists of two identical EM plane waves, of intensity $I_0 = 1 \times 10^{15}$ W/cm², propagating obliquely at $\theta = \pm 23^\circ$ with respect to the x axis. Locations 1^+ (1^-) and 2^+ (2^-) denote the blue- and red-shifted LW's produced by the pump laser with angle $\theta = +23^\circ$ (-23°), respectively. The forward-going, blue-shifted LW's from each beam that are on-axis ($k_y = 0$) are degenerate. The waves marked $1'$ and $1''$ are identified as the LW's produced by the first and second LDI steps of the degenerate LW, respectively.

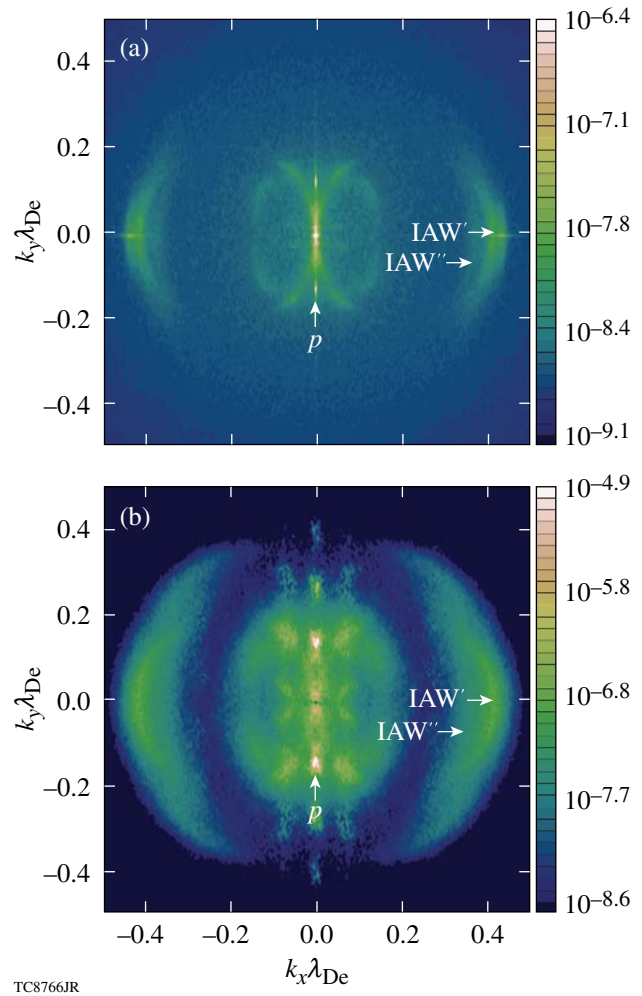


Figure 122.31

The time-averaged IAW spectrum $|\delta N_k|^2$ is shown for (a) RPIC and (b) ZAK simulations with the parameters $T_e = 4$ keV and $n_e/n_c = 0.231$. The pump consists of two EM plane waves, of intensity $I_0 = 1 \times 10^{15}$ W/cm², propagating obliquely with angle $\theta = \pm 23^\circ$ with respect to the x axis. The features labeled IAW' and IAW'' are IAW's generated by the first and second decay steps of the LDI of the common (degenerate) TPD LW. The feature indicated by the label p , with $k_x\lambda_{De} = 0$, is the density response to the ponderomotive force generated by the beating of the two incident plane waves at $k_y\lambda_{De} = \pm 2k_0\lambda_{De} \sin(23^\circ) \sim \pm 0.123$.

their fluctuation spectra have strikingly similar features. The dominant spectral features occur at precisely the same locations in k space. In Figs. 122.30(a) and 122.30(b), all eight of the single-beam decays ($1^\pm, 2^\pm$) can be seen, with the strongest spectral feature that of the degenerate, blue-shifted LW ($1^+, 1^-$). In addition, two LDI decay steps of the forward-TPD-produced LW's can be seen in both the RPIC and the ZAK calculations [indicated by the labels $1'$ at $\mathbf{k}_{1'}\lambda_{De} \approx (-0.20, 0.0)$ and $1''$ at $\mathbf{k}_{1''}\lambda_{De} \approx (0.16, 0.0)$ (Ref. 22)]. For the RPIC simulation, the LW excitation was computed to be $W = 2.7 \times 10^{-2}$, while the ZAK simulation has a significantly stronger level of LW's, $W = 2.8 \times 10^{-1}$. Figure 122.31 shows the IAW's associated with these two LDI decay steps, $\mathbf{k}_{IAW'}\lambda_{De} \approx (0.43, 0)$ and $\mathbf{k}_{IAW''}\lambda_{De} \approx (0.39, 0)$ (Ref. 22), although the IAW from the second decay is relatively weak and not distinctly evident in the ZAK calculations [Fig. 122.31(b)]. As a measure of the strength of the LDI process, RPIC gives $\mathcal{N}_{LDI} = 6.4 \times 10^{-5}$, whereas ZAK gives $\mathcal{N}_{LDI} = 3.7 \times 10^{-4}$. Again these comparisons of the \mathcal{N}_{LDI} values would indicate that LDI plays a relatively smaller role in the nonlinear saturation in RPIC compared to its role in ZAK. Another feature (p) evident in Fig. 122.31, although unrelated to LDI, are fluctuations at $\mathbf{k}\lambda_{De} \approx (0.0, \pm 0.123)$ caused by the ponderomotive force that results from the beating of the two incident light waves in the transverse direction at $k_y\lambda_{De} = \pm 2k_0\lambda_{De} \sin(23^\circ)$. Other features near $k_x = 0$ are caused by the beating of LW's with equal values of k_x and equal and opposite values of k_y .

The electron distribution computed from discrete simulation particles provides information regarding suprathermal electron generation. The energetic electron tails are often noisy, however, because of insufficient particle numbers. To improve the statistics, the electron distribution was time averaged over 20 ps. To provide information regarding the directionality of energetic electron generation, the (time-averaged) 2-D electron distribution function $f(v_x, v_y)$ was collapsed to 1-D as follows: First, the 2-D distribution f' was computed in a rotated (primed) velocity frame, where the v'_x direction is parallel to the desired probe angle θ_{probe} :

$$f'(v'_x, v'_y) = f(v'_x \cos \theta_{\text{probe}} + v'_y \sin \theta_{\text{probe}} \\ - v'_x \sin \theta_{\text{probe}} + v'_y \cos \theta_{\text{probe}}).$$

The distribution f' was then integrated in the perpendicular v'_y direction, within the limits $\pm 2v_{\text{the}}$, to yield a 1-D velocity distribution,

$$f_{1-D}(v'_x) \equiv \int_{-2v_{\text{the}}}^{2v_{\text{the}}} f'(v'_x, v'_y) dv'_y.$$

Typically, the angle θ_{probe} is chosen so that the v'_x axis aligns with the direction of the LW propagation. With this choice of θ_{probe} , $f_{1-D}(v'_x)$ yields a 1-D velocity distribution, and therefore a hot electron temperature, in the direction of LW propagation.

The time-averaged 1-D electron-distribution function f_{1-D} along the common wave direction [$\theta_{\text{probe}} = 0$, shown in Fig. 122.32(a)] indicates a hot-electron temperature of approximately $3 \times$ the initial background electron temperature $T_{\text{hot}} \sim 3T_{e0}$, where $T_{e0} = 4$ keV. Although the electrons have departed from their initial Maxwellian state, the hot-electron temperature is modest. Since our electron distribution was averaged over 20 ps and the simulation required 15 ps to reach saturation, it is possible that if the simulation were continued longer in time, the electron distribution would continue to evolve toward higher hot-electron temperatures. An often-used simple estimate of hot-electron temperature, based on a single-plane LW, is $T/T_{e0} \sim (v_\phi/v_{\text{the}})^2 = 22$ (Ref. 23). This estimate is in excess of our observed hot-electron temperature by a factor of about 7.4, although $v_\phi^2/v_{\text{the}}^2 = 22$ is exactly the place where the distribution function begins to deviate from a Maxwellian [indicated by the arrows in Fig. 122.32]. The probe direction $\theta_{\text{probe}} = 180^\circ$ [see Fig. 122.32(b)] gives a measure of hot-electron generation by the LDI-produced LW, with $T_{\text{hot}}/T_{e0} \sim 3$. Hot-electron temperatures along the other principal directions of $\theta_{\text{probe}} = \pm 23^\circ$ (directions of the non-degenerate forward blue-shifted plasmons; results not shown) also indicate $T_{\text{hot}}/T_{e0} \sim 3$. In this particular case, the hot-electron temperature does not appear to be significantly directional.

One observation to be drawn from the single-beam and overlapping-beam simulations shown above is that while the single-beam and the overlapped intensities are identical ($\Sigma I_0 = 2 \times 10^{15}$ W/cm²), the peak value of the LW spectrum for the overlapping-beams case (Fig. 122.30) is greater than that for the single-beam case (Fig. 122.27), while for the RPIC runs, the integrated spectrum is actually weaker: $W = 1.0 \times 10^{-1}$ for the single-beam case (Figs. 122.26–122.28) while $W = 2.7 \times 10^{-2}$ for the overlapping-beam case (Figs. 122.29–122.32). This is understandable if one considers the single-beam case with $I_0 = 2 \times 10^{15}$ W/cm² (Figs. 122.26–122.28) as two perfectly coincident beams, each with an intensity of 1×10^{15} W/cm². Consequently, each one of the four TPD-produced LW's has a corresponding overlapped LW. In the case of two beams propagating at angles $\theta = \pm 23^\circ$ (Figs. 122.29–122.32), only one

TPD-produced LW has a corresponding overlapped LW (location 1^\pm shown in Fig. 122.29). The fact that the peak intensity is higher is evidence that overlapping LW's enhance the TPD instability by allowing for nonlinear interaction between the crossing laser beams.

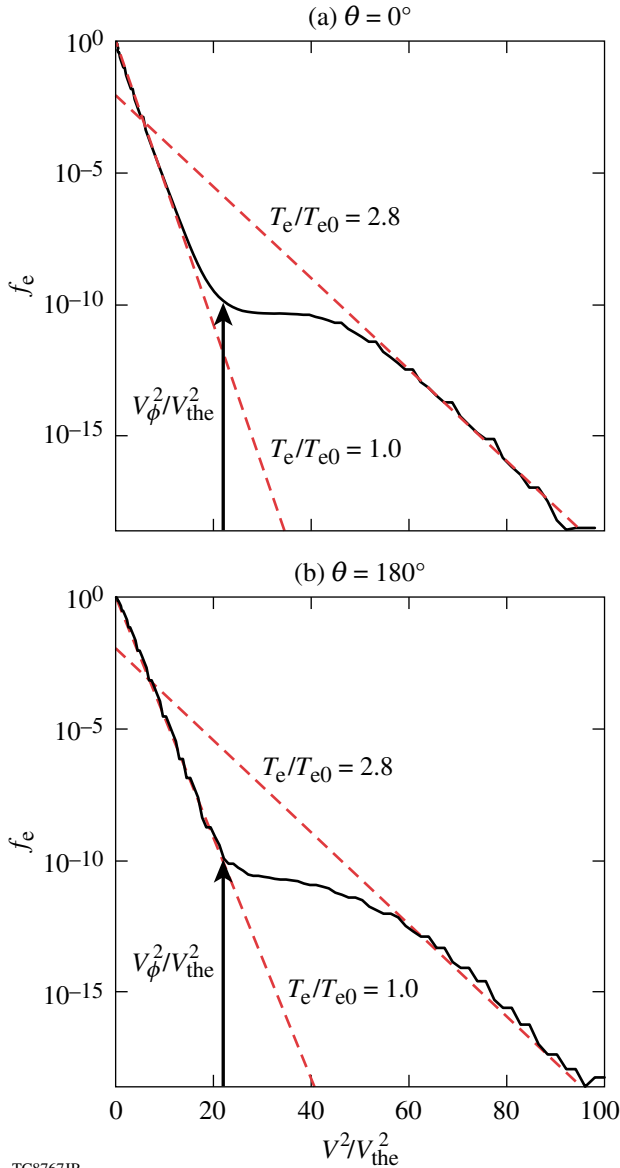


Figure 122.32 The 1-D time-averaged electron distribution shown along two directions ($\theta = 0^\circ, 180^\circ$) for two obliquely incident EM plane waves (at angles $\pm 23^\circ$ with respect to the x axis) with individual intensities of $I_0 = 1 \times 10^{15}$ W/cm² and parameters $T_{e0} = 4$ keV, $n_{e0}/n_c = 0.231$. The angle $\theta = 0^\circ$ (a) corresponds to the direction of the common LW, while the angle $\theta = 180^\circ$ (b) corresponds to the LDI LW direction of the common wave. The arrows indicate the value of v^2/v_{the}^2 corresponding to the phase velocity of the common wave.

In the final simulation set, the electron temperature was reduced to $T_{e0} = 2$ keV, which is typical of current OMEGA implosion experiments.¹ For this electron temperature and beam angle $\theta_\pm = \pm 23^\circ$, Eq. (C8) gives an electron density $n_{e0}/n_c = 0.241$, at which the simulations were performed. This was done to involve the shared plasma wave since it is believed to be important experimentally.¹ The laser geometry and intensity ($I_0 = 1 \times 10^{15}$ W/cm² for each beam) are identical to those corresponding to the previous case in Figs. 122.29–122.32. The individual beam intensity of 1×10^{15} W/cm² corresponds to a linear (amplitude) growth rate $\gamma_{TPD}/\omega_{pe0} \approx 4.3 \times 10^{-3}$, which is 83× above the single-beam collisional threshold (the collisional frequency ν_{e0}/ω_{pe0} is taken to be $\sim 4.7 \times 10^{-4}$). This final case is therefore more strongly driven than the second case, which was 50× the collisional threshold. The linear TPD wave geometry is illustrated in Fig. 122.33, the labels having the same meaning as in previous figures. The common LW now occurs at $\mathbf{k}\lambda_{De} \approx (0.16, 0.0)$ and corresponds to a phase velocity $v_\phi/v_{the} \approx 6.5$.

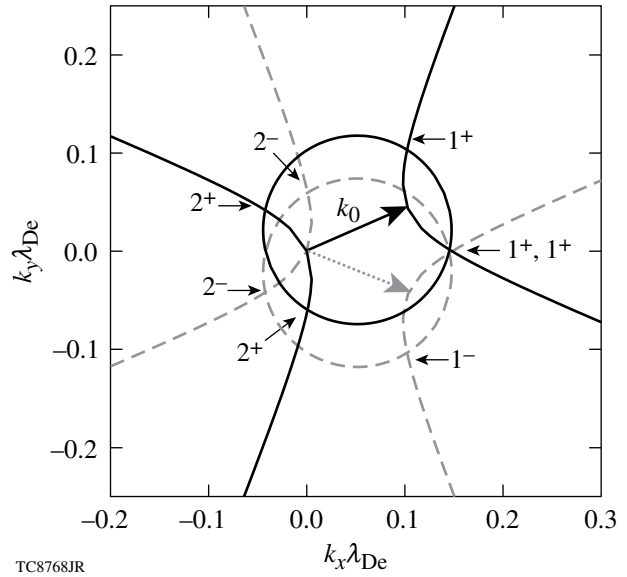


Figure 122.33 Decay diagram for the TPD instability of two EM plane-wave pump beams propagating with angles $\theta = \pm 23^\circ$ relative to the x direction in a plasma with $T_e = 2$ keV and $n_e/n_c = 0.241$. The solid (dashed) curves correspond to the individual decays of the beam with incident angle of $\theta = +23^\circ$ (-23°). The intersections of the circles (which specify frequency and wave-number matching) and the hyperbolae (which are the locations of maximum growth rate) [Eqs. (C1)–(C4)] that are labeled 1 and 2 give the expected location of the blue- and red-shifted TPD LW's, respectively. The on-axis ($k_y\lambda_{De} = 0$) blue-shifted LW's are degenerate.

Figures 122.34 and 122.35 show the normalized LW spectral intensity W_k and the IAW density spectra $|\delta N_k|^2$, respectively, time averaged over 20 ps. The RPIC and ZAK results bear

similar qualitative behavior to the $T_e = 4$ keV case when the reduction of $k\lambda_{De}$ is taken into account. Both the LW and IAW spectral features in the RPIC simulations are significantly nar-

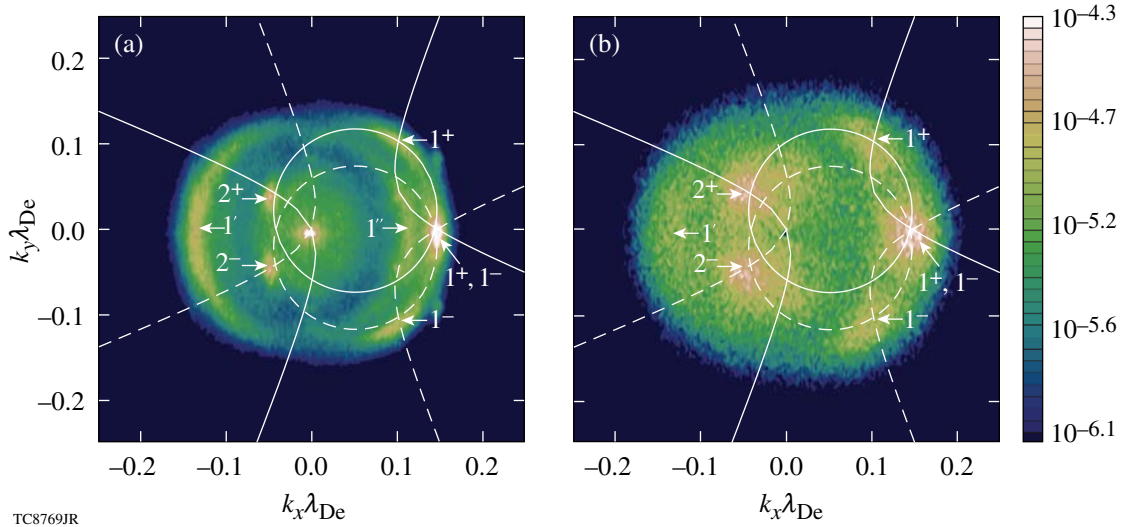


Figure 122.34 The time-averaged LW spectrum W_k is shown for (a) RPIC and (b) ZAK simulations for the parameters $T_e = 2$ keV and $n_e/n_c = 0.241$. The pump consists of two plane EM waves propagating at angles $\theta = \pm 23^\circ$ with respect to the x axis. Each pump laser beam has an intensity of $I_0 = 1 \times 10^{15}$ W/cm². The labels 1^+ (1^-) identify the forward-propagating, blue-shifted LW's resulting from the primary decay of the beam with angle $\theta = +23^\circ$ (-23°), while the labels 2^+ (2^-) mark the corresponding backward-propagating, red-shifted LW's. The degenerate LW is seen to dominate both the (a) RPIC and (b) ZAK spectra. The features marked $1'$ and $1''$ are identified as the first and second decay steps of the LDI of the shared LW. The second step is not seen in the ZAK calculations (b).

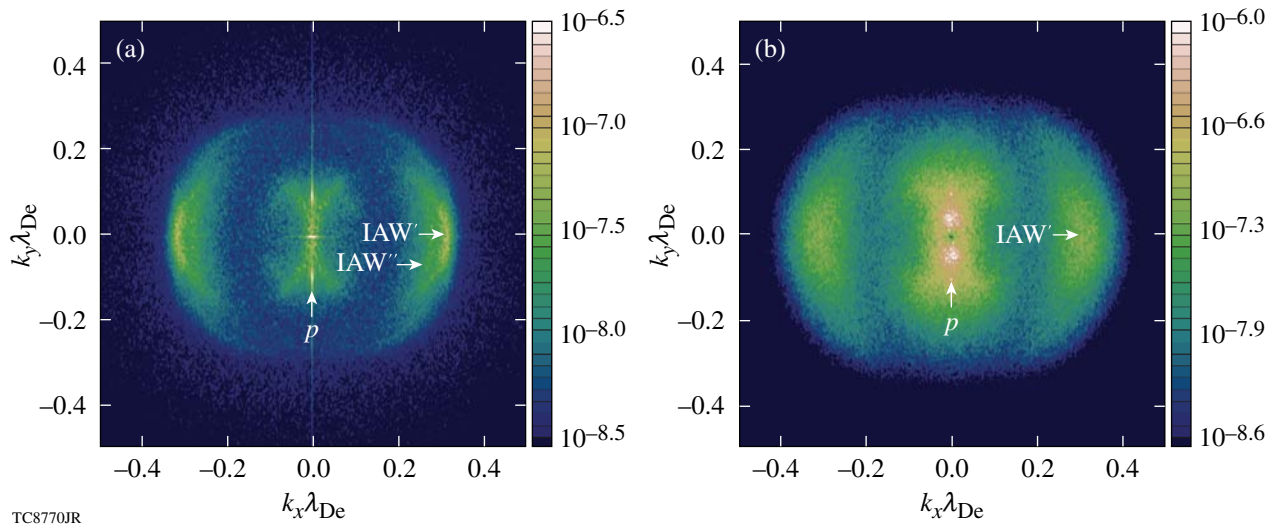


Figure 122.35 The time-averaged IAW spectrum $|\delta N_k|^2$ is shown for (a) RPIC and (b) ZAK simulations for the case with parameters $T_e = 2$ keV and $n_e/n_c = 0.241$. The pump consists of two plane EM waves propagating with angles $\theta = \pm 23^\circ$ with respect to the x axis, each with an intensity of $I_0 = 1 \times 10^{15}$ W/cm². The features labeled IAW' and IAW'' are IAW's generated by the first and second decay steps of the LDI of the common (degenerate) TPD LW. The second step is seen only in the RPIC calculation (a). The feature indicated by the label p , with $k_x\lambda_{De} = 0$, is the density response to the ponderomotive force generated by the beating of the two incident plane waves at $k_y\lambda_{De} = \pm 2k_0\lambda_{De} \sin(23^\circ) \sim \pm 0.09$.

rower and weaker than those of the ZAK simulations (RPIC: $W = 4.5 \times 10^{-2}$, ZAK: $W = 8.6 \times 10^{-2}$; for the LDI process, RPIC: $\mathcal{N} = 1.9 \times 10^{-4}$, ZAK: $\mathcal{N}_{\text{LDI}} = 4.3 \times 10^{-4}$). The RPIC LW spectrum [Fig. 122.34(a)] contains evidence of two LDI decay steps of the common LW: the primary LDI step, marked with the label 1', at $\mathbf{k}_1 \lambda_{\text{De}} \approx (-0.13, 0.0)$ and a second LDI step, marked 1'' at $\mathbf{k}_1 \lambda_{\text{De}} \approx (0.09, 0.0)$ (Ref. 22). The RPIC IAW spectrum [Fig. 122.35(a)] also shows the IAW's corresponding to these two LDI decay steps [$\mathbf{k}_{\text{IAW}} \lambda_{\text{De}} \approx (0.29, 0.0)$ and [$\mathbf{k}_{\text{IAW}} \lambda_{\text{De}} \approx (0.25, 0.0)$ (Ref. 22)], although the IAW from the second decay is relatively weak. Only one LDI step is clearly evident in the ZAK calculations [Figs. 122.34(b) and 122.35(b)]. The distinctive fluctuations in the IAW spectrum $|\delta N_k|^2$ at $\mathbf{k} \lambda_{\text{De}} \approx (0.0, \pm 0.09)$ are again due to ponderomotive force generated by the beating of the two obliquely propagating incident light waves. Although not shown, the difference between the two calculations can be reduced by comparing the ZAK spectra with those of RPIC carried out at a higher intensity. Results (not shown) indicate that the LW and IAW spectra in RPIC simulations broaden significantly. This observation is consistent with past experience.^{11,24}

The time-averaged (over 20 ps), 1-D electron-distribution function along the common-wave direction ($\theta_{\text{probe}} = 0$), shown in Fig. 122.36(a), gives $T_{\text{hot}}/T_{e0} \sim 14$. Again, the simple estimate of hot-electron temperature is $T_{\text{hot}}/T_{e0} \sim (v_\phi/v_{\text{the}})^2 = 42$ (Ref. 23). This estimate is in excess of the observed hot-electron temperature by a factor of ~ 3 . The simple estimate $T_{\text{hot}}/T_{e0} = (v_\phi/v_{\text{the}})^2$, based on a single-plane LW, is not accurate here because the LW spectrum contains a broad and complex spectrum of waves. The phase velocity of the common wave is, however, close to the position where the distribution function first begins to deviate from the initial Maxwellian (shown by the arrows in Fig. 122.36). The hot-electron temperature in the LDI direction of the common LW wave ($\theta_{\text{probe}} = 180^\circ$), shown in Fig. 122.36(b), is cooler with $T_{\text{hot}}/T_{e0} \sim 10$ most likely because the LDI-produced LW's are not as strong as the primary LW. The phase velocities of the primary and LDI LW's differ only slightly. The hot-electron temperatures along the other principal directions $\theta_{\text{probe}} = \pm 23^\circ$ (results not shown) were also determined to be $T_{\text{hot}}/T_{e0} \sim 10$. The hot-electron temperatures for the $T_{e0} = 2$ keV case are significantly higher than that for the $T_{e0} = 4$ keV case. The intensities of the degenerate LW's for the two temperature cases do not differ significantly. The TPD-produced LW's for an electron temperature of $T_{e0} = 2$ keV occur at lower values of $k\lambda_{\text{De}}$ and therefore have greater phase velocities since

$$v_\phi/v_{\text{the}} = \left[1 + (3/2)(k\lambda_{\text{De}})^2 \right] / (k\lambda_{\text{De}}).$$

Waves with greater phase velocity may lead to higher hot-electron temperatures, even though T_{hot} is not seen to scale as strongly as $(v_\phi/v_{\text{the}})^2$, as might be suggested by the simple, single-plane-LW estimate.

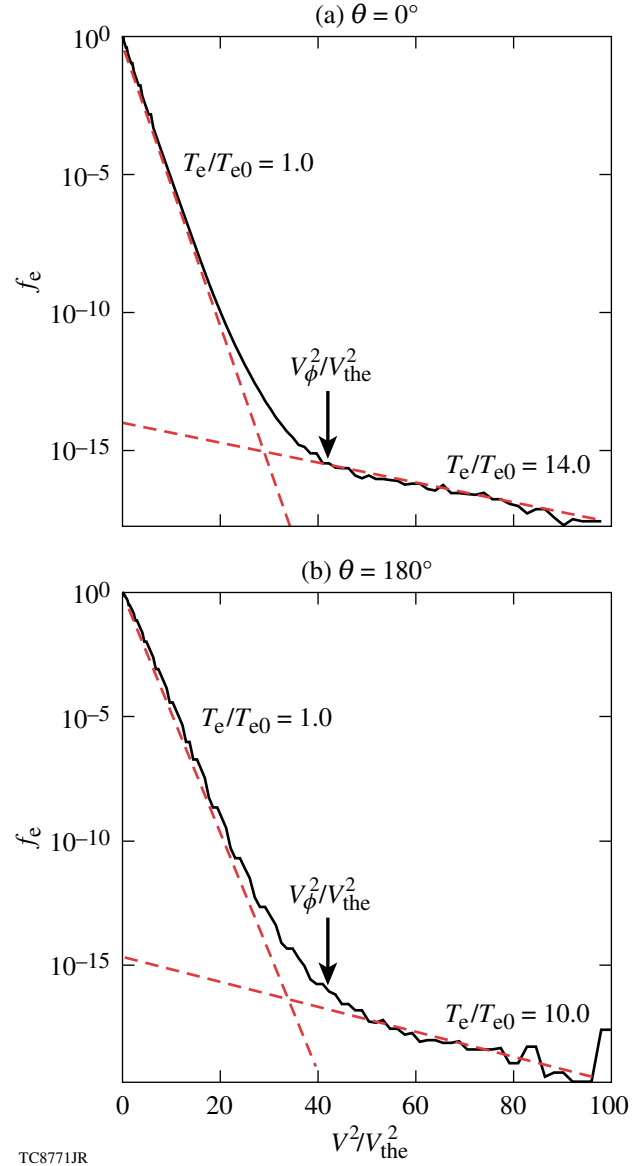


Figure 122.36

The 1-D, time-averaged electron distribution shown along two directions [$\theta = 0^\circ$ (top panel) and $\theta = 180^\circ$ (bottom panel)] for the case of two EM plane waves, each of intensity $I_0 = 1 \times 10^{15}$ W/cm², that are incident at angles of $\theta = \pm 23^\circ$ on a plasma with $T_e = 2$ keV and $n_e/n_c = 0.241$. The temperature in the direction $\theta = 0^\circ$ ($T_{\text{hot}}/T_{e0} = 14$), as determined by the fit shown by the red dashed curves, is greater than that in the direction $\theta = 180^\circ$ ($T_{\text{hot}}/T_{e0} = 10$). The arrows indicate the value of v^2/v_{the}^2 corresponding to the phase velocity of the common LW.

Summary and Conclusions

The purpose of this article has been to present the RPIC model for TPD and to establish it as a useful and reliable model for simulating the nonlinear development of TPD. The simulations were performed in homogeneous plasmas to facilitate comparisons with linear theory. Given the encouraging results in homogeneous plasma, the next step in the development of the RPIC TPD model will be to introduce experimentally relevant density gradients and flow velocities.

The RPIC model and the Zakharov limit were compared for three separate cases. In all three cases, shown in **Simulation Results** (p. 92), the level of LW turbulence excited by TPD was lower in RPIC than in ZAK, although both models displayed qualitatively similar k -space fluctuation spectra. Therefore, kinetic effects—primarily hot-electron generation—are likely a competing saturation mechanism together with LDI. This is consistent with the results of several previous works.^{11,24} Further research is required to determine the relative importance of LDI and hot-electron generation when they act simultaneously.

Two of the three cases investigated TPD excited by crossing laser beams. These simulations show that at a certain density, for a given angle between the beams, the beams can share a common primary LW, thereby enhancing the TPD instability (in an inhomogeneous plasma such a density can always be found, but here it was chosen by design). The saturation of the crossed-beam TPD instability by LDI and modification of the electron-distribution function is also apparent. The heated-electron-distribution function was observed to deviate from the initial Maxwellian at a velocity corresponding to the phase velocity of the common LW. Crossed-beam irradiation also introduced a nonzero ponderomotive force in the electron equation of motion from the transverse electric field. The effects of this term were observed in the perturbed density spectra. A strong feature in the low-frequency density fluctuation spectrum also resulted from the ponderomotive beating of two LW's sharing the same parallel wave number (with respect to the laser direction) but with equal and opposite perpendicular wave numbers.¹⁴ This feature was also evident in our previous ZAK simulations but never noted, which would imply that density channels are produced parallel to the laser direction. Whether this survives in an inhomogeneous plasma remains to be studied.

The semi-quantitative agreement of RPIC modeling and ZAK modeling, for the few survey cases presented here, highlights the similarities and differences between the kinetic RPIC model and its limiting (fluid) form. In this way, the RPIC

modeling provides a bridge to systematically improve upon ZAK modeling. This is desirable because fluid-type codes are much more efficient than PIC codes and can therefore include more of the essential experimental realities (e.g., three spatial dimensions and speckled laser beams). Of particular interest is the possibility, currently under investigation, that the discrepancy between the two models might be recoverable by including modifications of the electron-distribution function in the quasi-linear approximation.¹¹ If possible, this would have the benefit of greatly reduced computational expense, allowing for more-realistic simulations to be made, for example, in three spatial dimensions. The resulting modified electron energy distributions are expected to be strongly dependent on the boundary conditions used for electrons entering and leaving the simulation box (this is consistent with conclusions in Sanbonmatsu *et al.*¹¹). Indeed, the present calculations should not be regarded as predicting experimental hot-electron spectra since it has been argued that the recirculation of hot electrons through the TPD-active region must be accounted for by any physically realistic model of hot-electron generation in spherical implosions.²⁰

Finally, the currents generating experimentally observable EM signatures of TPD (the secondary radiation emissions at $\omega_0/2$ and $3\omega_0/2$), which typically involve a tiny fraction of the LW and IAW energy, can be calculated by postprocessing the high-frequency electric-field envelopes and the low-frequency electron-density fluctuations generated in either the RPIC or the ZAK modeling. This technique is exactly the same as used in Refs. 9 and 17 for the ZAK modeling. This is another advantage of the RPIC modeling, which uses the same envelope representations as ZAK, over standard PIC methods. With this procedure future studies of the correlation of hot-electron effects with $\omega_0/2$ radiation may be possible.

ACKNOWLEDGMENT

We are pleased to acknowledge useful discussions with Drs. A. V. Maximov, W. Seka, R. W. Short, and B. Langdon.

This research was supported by (1) the U.S. Department of Energy, Office of Inertial Confinement Fusion under Cooperative Agreement No. DE-FC52-08NA28302, the University of Rochester, and the New York State Energy Research and Development Authority and (2) the National Nuclear Security Agency through its High-Energy-Density Laboratory Plasmas Grant No. DE-FG52-09NA29545. The support of DOE does not constitute an endorsement by DOE of the views expressed in this article.

Appendix A: Derivation of the RPIC Equations

In this Appendix, a derivation of the RPIC model is presented. One notable difference between standard PIC methods and RPIC is the explicit removal of the laser time scale from

RPIC equations of motion. As a result of removing the laser time scale, it is essential that RPIC equations of motion are expressed in an oscillating, non-inertial frame. There are three major components of the RPIC derivation: the electron equation of state (closure for our RPIC model), the nonlinear Schrödinger equation (EM propagation and pump depletion model), and the reduced-description particle equations of motion.

1. Electron Equation of State

Assume that the velocity $\tilde{\mathbf{U}}$, electrostatic potential ϕ , and pressure p are of the following form:

$$\tilde{\mathbf{U}} = \tilde{\mathbf{U}}_S + \frac{1}{2} [\tilde{\mathbf{U}}_F \exp(-i\omega_{LW}t) + \text{c.c.}].$$

$$\phi = \phi_S + \frac{1}{2} [\phi_F \exp(-i\omega_{LW}t) + \text{c.c.}],$$

$$p \approx p_S.$$

Substituting the above expression for $\tilde{\mathbf{U}}$ into Eq. (18), keeping only terms of frequencies $\omega = 0, \pm\omega_{LW}, \pm(\omega_0 - \omega_{LW}), \pm(\omega_0 - 2\omega_{LW})$, the individual terms in Eq. (18) are approximated as

$$\frac{\partial \tilde{\mathbf{U}}}{\partial t} \approx -\frac{\omega_{LW}}{2} [i\tilde{\mathbf{U}}_F \exp(-i\omega_{LW}t) + \text{c.c.}], \quad (\text{A1})$$

$$\tilde{\mathbf{U}} \cdot \tilde{\nabla} \tilde{\mathbf{U}} \approx \frac{1}{4} \tilde{\nabla} (\tilde{\mathbf{U}}_F \cdot \tilde{\mathbf{U}}_F^*) - \frac{1}{4} (\tilde{\mathbf{U}}_F \times \tilde{\nabla} \times \tilde{\mathbf{U}}_F^* + \text{c.c.}), \quad (\text{A2})$$

$$\mathbf{A} \cdot \mathbf{A} \approx \frac{1}{2} \mathbf{a}_0 \cdot \mathbf{a}_0^*, \quad (\text{A3})$$

$$\tilde{\mathbf{U}} \cdot \mathbf{A} \approx \frac{1}{4} \left\{ \tilde{\mathbf{U}}_F^* \cdot \mathbf{a}_0 \exp[-i(\omega_0 - \omega_{LW})t] + \text{c.c.} \right\}, \quad (\text{A4})$$

$$\mathbf{A} \times \tilde{\nabla} \times \tilde{\mathbf{U}}$$

$$\approx \frac{1}{4} \left\{ \mathbf{a}_0 \times \tilde{\nabla} \times \tilde{\mathbf{U}}_F^* \exp[-i(\omega_0 - \omega_{LW})t] + \text{c.c.} \right\}, \quad (\text{A5})$$

$$\mathbf{A} \cdot \tilde{\nabla} \tilde{\mathbf{U}}$$

$$\approx \frac{1}{4} \left\{ \mathbf{a}_0 \cdot \tilde{\nabla} \tilde{\mathbf{U}}_F^* \exp[-i(\omega_0 - \omega_{LW})t] + \text{c.c.} \right\}, \quad (\text{A6})$$

where it has been assumed that $|\partial \tilde{\mathbf{U}}_F / \partial t| \ll \omega_{LW} |\tilde{\mathbf{U}}_F|$ and $|\mathbf{U}_S| \ll |\mathbf{U}_F|$. Substituting these approximations in Eqs. (A1)–(A6) into Eq. (18), neglecting the second-order convective term $\tilde{\mathbf{U}} \cdot \tilde{\nabla} \tilde{\mathbf{U}}$, and collecting terms of similar frequencies, one obtains

$$\begin{aligned} \tilde{\mathbf{U}}_F = & \frac{q}{im\omega_{LW}} \tilde{\nabla} \left[\phi_F - \frac{1}{2c} \tilde{\mathbf{U}}_F^* \cdot \mathbf{a}_0 \exp(-i\Delta\omega t) \right] \\ & + \frac{q \exp(-i\Delta\omega t)}{2imc\omega_{LW}} (\mathbf{a}_0 \times \tilde{\nabla} \times \tilde{\mathbf{U}}_F^* + \mathbf{a}_0 \cdot \tilde{\nabla} \tilde{\mathbf{U}}_F^*), \end{aligned} \quad (\text{A7})$$

and

$$\begin{aligned} \frac{1}{4} \tilde{\nabla} (\tilde{\mathbf{U}}_F \cdot \tilde{\mathbf{U}}_F^*) = & \frac{1}{4} [\tilde{\mathbf{U}}_F \times \tilde{\nabla} \times \tilde{\mathbf{U}}_F^* + \tilde{\mathbf{U}}_F^* \times \tilde{\nabla} \times \tilde{\mathbf{U}}_F] \\ & - \frac{q}{m} \tilde{\nabla} \phi_S - \frac{\tilde{\nabla} p_S}{n_S m} - \frac{q^2}{4m^2 c^2} \tilde{\nabla} (\mathbf{a}_0 \cdot \mathbf{a}_0^*), \end{aligned} \quad (\text{A8})$$

where $\Delta\omega \equiv \omega_0 - 2\omega_{LW}$. Setting $q = -e$ and $m = m_e$, Eq. (A7) is solved approximately to give

$$\tilde{\mathbf{U}}_F \approx \frac{e}{im_e \omega_{LW}} \mathbf{E}_{\text{eff}}, \quad (\text{A9})$$

where \mathbf{E}_{eff} was previously defined in Eq. (28). Substituting Eq. (A9) into Eq. (A8), neglecting the term in the square brackets on the right-hand side (rhs) of Eq. (A8) and integrating the resulting equation, assuming a pressure profile $p_S = n_0 T_{e0} (n_S/n_0)^\gamma$, with γ being the ratio of specific heats (isothermal electrons: $\gamma = 1$; adiabatic electrons: $\gamma = 5/3$), one obtains the electron equation of state, Eq. (26). This provides closure for the RPIC model.

2. Field Equations

The driving current \mathbf{J} resulting from self-consistent electron motion is

$$\begin{aligned}\mathbf{J} &= -en\mathbf{U}, \\ &= -en\left(\tilde{\mathbf{U}} - \frac{q\mathbf{A}}{mc}\right), \\ &= -en\left(\tilde{\mathbf{U}} + \frac{e\mathbf{A}}{m_e c}\right).\end{aligned}$$

The components of \mathbf{J} with frequencies $\pm\omega_0$ and $\pm 2\omega_{\text{LW}}$ (since $\omega_0 \approx 2\omega_{\text{LW}}$ for TPD) are of importance:

$$\begin{aligned}\mathbf{J} &\approx -\frac{1}{2}\left\{\left[\frac{e^2 n_{eS}\mathbf{a}_0}{m_e c} + \frac{en_{eF}\tilde{\mathbf{U}}_F}{2}\exp(i\Delta\omega\tilde{t})\right]\exp(-i\omega_0\tilde{t}) + \text{c.c.}\right\}, \\ \mathbf{J} &\equiv \frac{1}{2}\left[\mathbf{J}_0\exp(-i\omega_0\tilde{t}) + \text{c.c.}\right],\end{aligned}\quad (\text{A10})$$

$$\mathbf{J}_0 = -\left[\frac{e^2 n_{eS}\mathbf{a}_0}{m_e c} + \frac{en_{eF}\tilde{\mathbf{U}}_F}{2}\exp(i\Delta\omega\tilde{t})\right],$$

where $\tilde{\mathbf{U}}_F$ is given in Eq. (A9). On substituting Eq. (A9) into Eq. (A10), an equation for \mathbf{J}_0 is obtained [Eq. (33)], from which the transverse current \mathbf{J}_{0T} can be computed:

$$\mathbf{J}_{0T} \equiv \mathbf{J}_0 + \tilde{\nabla}\chi_0,$$

$$\tilde{\nabla}^2\chi_0 = -\tilde{\nabla}\cdot\mathbf{J}_0,$$

$$-\frac{1}{c^2}\frac{\partial^2\mathbf{A}}{\partial\tilde{t}^2} + \tilde{\nabla}^2\mathbf{A} = -\frac{4\pi}{c}\frac{1}{2}\left[\mathbf{J}_{0T}\exp(-i\omega_0\tilde{t}) + \text{c.c.}\right]. \quad (\text{A11})$$

A substitution of the above expression for \mathbf{J}_T into the second-order wave equation, assuming slowly varying envelopes and separating frequency components, results in a nonlinear Schrödinger equation for the evolution of the incident EM-wave envelope [Eq. (31)].

3. Time-Averaged Single-Particle Equations of Motion

The exact single-particle equation of motion is time averaged to obtain the RPIC single-particle equation of motion. Recall that Eq. (16) is exact and is applicable to both electrons and ions.

The electron particle velocity can be conveniently cast in the form

$$\tilde{\mathbf{u}}_e = \tilde{\mathbf{u}}_{e0} + \tilde{\mathbf{u}}_{eS} + \frac{1}{2}\left[\tilde{\mathbf{u}}_{eF}\exp(-i\omega_{\text{LW}}\tilde{t}) + \text{c.c.}\right], \quad (\text{A12})$$

where $\tilde{\mathbf{u}}_{e0}$ is the initial electron velocity, $\tilde{\mathbf{u}}_{eS}$ the low-frequency velocity perturbation, and $\tilde{\mathbf{u}}_{eF}$ is the high-frequency velocity perturbation. Equation (16) is solved approximately as follows: First, neglecting contributions from the laser pump and assuming $|\partial\tilde{\mathbf{u}}_{eS}/\partial\tilde{t}| \ll \omega_{\text{LW}}|\tilde{\mathbf{u}}_{eF}|$, Eq. (16) yields

$$\begin{aligned}\tilde{\mathbf{u}}_{eF} &\approx -\frac{e}{im_e\omega_{\text{LW}}}\tilde{\nabla}\phi_F, \\ &= \frac{e}{im_e\omega_{\text{LW}}}\mathbf{E}_F.\end{aligned}$$

Then, substituting the above approximate expression for $\tilde{\mathbf{u}}_{eF}$ into Eqs. (A12) and (16) and keeping only electron responses at the ion-acoustic and Langmuir time scales, i.e., $\omega \sim 0, \pm\omega_{\text{LW}}, \pm(\omega_0 - \omega_{\text{LW}})$, Eq. (19) is obtained, the electron reduced-description equation of motion in the oscillating frame.

Specifying these results to 2-D, assuming polarization in the y direction and a fixed pump wave $a_0 = a_{00}\exp(ik_0x)$, Eq. (19) further reduces to give

$$\begin{aligned}m_e\frac{d\tilde{\mathbf{u}}_e}{d\tilde{t}} &\approx -e\mathbf{E} - \frac{e^2}{4m_e c^2}\tilde{\nabla}\left|\mathbf{a}_0\right|^2 \\ &+ \hat{\mathbf{x}}\frac{e^2 k_0}{4cm_e\omega_{\text{LW}}}\left\{\mathbf{a}_0 \cdot \mathbf{E}_F^* \exp[-i(\omega_0 - \omega_{\text{LW}})\tilde{t}] + \text{c.c.}\right\}.\end{aligned}\quad (\text{A13})$$

The ion-particle equations of motion follow similarly to yield Eq. (21).

Appendix B: Derivation of the Zakharov Equations from RPIC

In this Appendix, it will be shown how the Zakharov equations may be obtained from the RPIC model under certain approximations. This connection ensures that the RPIC

equations have the correct limiting form (since the Zakharov equations may also be shown to be a consequence of the Vlasov equations on which the RPIC model is based), and that the Zakharov and RPIC models predict the same physical behavior in the linear regime.

It is noted that while the RPIC equations are more conveniently written in the oscillating frame, the Zakharov equations are customarily written in the laboratory frame of reference. To begin, Eq. (19) is transformed back into the laboratory frame of reference:

$$\begin{aligned}
m_e \frac{d\tilde{\mathbf{u}}_e}{dt} &\approx -e\mathbf{E} - \frac{e^2}{4m_e c^2} \nabla |\mathbf{a}_0|^2 \\
&- \frac{e^2}{4cm_e \omega_{LW}} \left[i\nabla(\mathbf{E}_F^* \cdot \mathbf{a}_0) \exp(-i\Delta\omega t) \exp(-i\omega_{LW}t) + \text{c.c.} \right] \\
&- \frac{e^2}{4cm_e \omega_{LW}} \left[-i(\mathbf{a}_0 \cdot \nabla) \mathbf{E}_F^* \exp(-i\Delta\omega t) \right. \\
&\times \left. \exp(-i\omega_{LW}t) + \text{c.c.} \right], \tag{B1}
\end{aligned}$$

since $\tilde{\nabla} = \tilde{\nabla}$, $\tilde{t} = t$, and $d/d\tilde{t} = d/dt$, as shown previously. Here, \mathbf{E} is the physical electric field reconstituted from the envelope representation

$$\mathbf{E} = \mathbf{E}_s + \frac{1}{2} \left[\mathbf{E}_1 \exp(-i\omega_{LW}t) + \mathbf{E}_2 \exp(-2i\omega_{LW}t) + \text{c.c.} \right]. \tag{B2}$$

Using the definition $\mathbf{u}_e = \tilde{\mathbf{u}}_e + e\mathbf{A}/m_e c$, one obtains from Eq. (B1)

$$\begin{aligned}
\frac{d\mathbf{u}_e}{dt} &= -\frac{e\mathbf{E}}{m_e} - \frac{e^2}{4m_e^2 c^2} \nabla |\mathbf{a}_0|^2 + \frac{e^2}{4m_e^2 c^2} (\mathbf{a}_0^* \cdot \nabla \mathbf{a}_0 + \text{c.c.}) \\
&- \frac{e^2}{4m_e^2 c \omega_{LW}} \left\{ \left[\nabla(\mathbf{E}_F^* \cdot \mathbf{a}_0) - \mathbf{a}_0 \cdot \nabla \mathbf{E}_F^* \right. \right. \\
&- \left. \left. \mathbf{E}_F^* \cdot \nabla \mathbf{a}_0 \right] i \exp[-i(\omega_{LW} + \Delta\omega)t] + \text{c.c.} \right\} \\
&- \frac{e}{m_e} \frac{\omega_0}{2c} \left\{ i\mathbf{a}_0 \exp[-i(2\omega_{LW} + \Delta\omega)t] + \text{c.c.} \right\}.
\end{aligned}$$

Changing to conventional Zakharov nomenclature, $\mathbf{E}_1 \equiv \mathbf{E}_F$ and $\mathbf{E}_2 \equiv i\omega_0 \mathbf{a}_0/c$, the above equation becomes

$$\frac{d\mathbf{u}_e}{dt} = \mathcal{A}, \tag{B3}$$

$$\begin{aligned}
\mathcal{A} &\equiv \mathcal{A}_0 + \frac{1}{2} \left[\mathcal{A}_1 \exp(-i\omega_{LW}t) + \text{c.c.} \right] \\
&+ \frac{1}{2} \left[\mathcal{A}_2 \exp(-2i\omega_{LW}t) + \text{c.c.} \right], \tag{B4}
\end{aligned}$$

$$\begin{aligned}
\mathcal{A}_0 &= -\frac{e\mathbf{E}_s}{m_e} - \frac{e^2}{4m_e^2 \omega_0^2} \nabla |\mathbf{E}_2|^2 \\
&+ \frac{e^2}{4m_e^2 \omega_0^2} (\mathbf{E}_2^* \cdot \nabla \mathbf{E}_2 + \text{c.c.}), \tag{B5}
\end{aligned}$$

$$\begin{aligned}
\mathcal{A}_1 &= -\frac{e\mathbf{E}_1}{2m_e} \\
&- \frac{e^2}{2m_e^2 \omega_0 \omega_{LW}} \left[\nabla(\mathbf{E}_1^* \cdot \mathbf{E}_2) - \mathbf{E}_2 \cdot \nabla \mathbf{E}_1^* \right. \\
&- \left. \mathbf{E}_1^* \cdot \nabla \mathbf{E}_2 \right] \exp(-i\Delta\omega t), \tag{B6}
\end{aligned}$$

$$\mathcal{A}_2 = -\frac{e\mathbf{E}_2}{2m_e} \exp(-i\Delta\omega t), \tag{B7}$$

where $\Delta\omega$ was defined previously [see Eq. (30)]. The Vlasov equation corresponding to the acceleration \mathcal{A} is

$$(\partial_t + \mathbf{v} \cdot \partial_{\mathbf{x}})F + \mathcal{A} \cdot \partial_{\mathbf{v}}F = 0, \tag{B8}$$

where the distribution function F can be written in terms of slowly varying envelopes

$$\begin{aligned}
F(\mathbf{x}, t; \mathbf{v}) &= f_0 + \frac{1}{2} \left[f_1 \exp(-i\omega_{LW}t) + \text{c.c.} \right] \\
&+ \frac{1}{2} \left[f_2 \exp(-2i\omega_{LW}t) + \text{c.c.} \right], \tag{B9}
\end{aligned}$$

$$f_0(\mathbf{x}, t; \mathbf{v}) = f_M(\mathbf{v}) + \delta f_0(\mathbf{x}, t; \mathbf{v}). \quad (\text{B10})$$

Here, $f_M(\mathbf{v})$ is the time-stationary, spatially uniform background Maxwellian distribution. Substituting Eqs. (B4)–(B7) and (B9)–(B10) into Eq. (B8) and separating frequency components, one obtains the coupled equations

$$\begin{aligned} (\partial_t + \mathbf{v} \cdot \partial_{\mathbf{x}}) \delta f_0 &= \frac{e}{m_e} \mathbf{E}_s \cdot \partial_{\mathbf{v}} (f_M + \delta f_0) \\ &+ \frac{e}{4m_e} (\mathbf{E}_1 \cdot \partial_{\mathbf{v}} f_1^* + \text{c.c.}) + \frac{e}{4m_e} (\tilde{\mathbf{E}}_2 \cdot \partial_{\mathbf{v}} f_2^* + \text{c.c.}), \end{aligned} \quad (\text{B11})$$

$$\begin{aligned} (-i\omega_{\text{LW}} + \partial_t + \mathbf{v} \cdot \partial_{\mathbf{x}}) f_1 &= \frac{e}{m_e} (\mathbf{E}_1 + \mathbf{h}_1) \cdot \partial_{\mathbf{v}} (f_M + \delta f_0) \\ &+ \frac{e}{m_e} \mathbf{E}_s \cdot \partial_{\mathbf{v}} f_1 + \frac{e}{2m_e} \tilde{\mathbf{E}}_2 \cdot \partial_{\mathbf{v}} f_1^* + \frac{e}{2m_e} (\mathbf{E}_1^* + \mathbf{h}_1^*) \cdot \partial_{\mathbf{v}} f_2, \end{aligned} \quad (\text{B12})$$

$$\begin{aligned} (-2i\omega_{\text{LW}} + \partial_t + \mathbf{v} \cdot \partial_{\mathbf{x}}) f_2 &= \frac{e}{m_e} \tilde{\mathbf{E}}_2 \cdot \partial_{\mathbf{v}} (f_M + \delta f_0) \\ &+ \frac{e}{2m_e} (\mathbf{E}_1 + \mathbf{h}_1) \cdot \partial_{\mathbf{v}} f_1 + \frac{e}{m_e} \mathbf{E}_s \cdot \partial_{\mathbf{v}} f_2, \end{aligned} \quad (\text{B13})$$

$$\tilde{\mathbf{E}}_2 \equiv \exp(-i\Delta\omega t) \mathbf{E}_2, \quad (\text{B14})$$

$$\begin{aligned} \mathbf{h}_1 &\equiv \frac{e}{2m_e \omega_0 \omega_{\text{LW}}} \left[\nabla (\mathbf{E}_1^* \cdot \tilde{\mathbf{E}}_2) \right. \\ &\left. - \tilde{\mathbf{E}}_2 \cdot \nabla \mathbf{E}_1^* - \mathbf{E}_1^* \cdot \nabla \tilde{\mathbf{E}}_2 \right], \end{aligned} \quad (\text{B15})$$

where terms that are not linear in \mathbf{E}_1 or linear in $\mathbf{E}_2 \cdot \mathbf{E}_1^*$ are neglected since only the linear parametric dispersion is of interest.

Fourier transforming Eqs. (B11)–(B13) in space and time, one obtains

$$\begin{aligned} -i(\omega - \mathbf{k} \cdot \mathbf{v}) \delta f_0(\mathbf{k}, \omega, \mathbf{v}) &= \frac{e}{m_e} \iint d\mathbf{k}' d\omega' \mathbf{E}'_s \cdot \partial_{\mathbf{v}} \delta f_0'' \\ &+ \frac{e}{4m_e} \iint d\mathbf{k}' d\omega' \mathbf{E}'_1 \cdot \partial_{\mathbf{v}} [f_1^*]'' + \text{c.c.} \\ &+ \frac{e}{4m_e} \iint d\mathbf{k}' d\omega' \mathbf{E}'_2 \cdot \partial_{\mathbf{v}} [f_2^*]'' + \text{c.c.}, \end{aligned} \quad (\text{B16})$$

$$\begin{aligned} &-i(\omega_{\text{LW}} + \omega - \mathbf{k} \cdot \mathbf{v}) f_1(\mathbf{k}, \omega, \mathbf{v}) \\ &= \frac{e}{m_e} [\mathbf{E}_1(\mathbf{k}, \omega) + \mathbf{h}_1(\mathbf{k}, \omega)] \cdot \partial_{\mathbf{v}} f_M(\mathbf{v}) \\ &+ \frac{e}{m_e} \iint d\mathbf{k}' d\omega' \mathbf{E}'_s \cdot \partial_{\mathbf{v}} f_1'' \\ &+ \frac{e}{m_e} \iint d\mathbf{k}' d\omega' \mathbf{E}'_1 \cdot \partial_{\mathbf{v}} \delta f_0'' \\ &+ \frac{e}{2m_e} \iint d\mathbf{k}' d\omega' \tilde{\mathbf{E}}'_2 \cdot [\partial_{\mathbf{v}} f_1^*]'' \\ &+ \frac{e}{2m_e} \iint d\mathbf{k}' d\omega' [\mathbf{E}'_1]^* \cdot \partial_{\mathbf{v}} f_2'', \end{aligned} \quad (\text{B17})$$

$$\begin{aligned} -i(2\omega_{\text{LW}} + \omega - \mathbf{k} \cdot \mathbf{v}) f_2(\mathbf{k}, \omega, \mathbf{v}) &= \frac{e}{m_e} \tilde{\mathbf{E}}_2(\mathbf{k}, \omega) \cdot \partial_{\mathbf{v}} f_M(\mathbf{v}) \\ &+ \frac{e}{m_e} \iint d\mathbf{k}' d\omega' \mathbf{E}'_2 \cdot \partial_{\mathbf{v}} \delta f_0'' \\ &+ \frac{e}{2m_e} \iint d\mathbf{k}' d\omega' (\mathbf{E}'_1 + \mathbf{h}'_1) \cdot \partial_{\mathbf{v}} f_1'' \\ &+ \frac{e}{m_e} \iint d\mathbf{k}' d\omega' \mathbf{E}'_s \cdot \partial_{\mathbf{v}} f_2'', \end{aligned} \quad (\text{B18})$$

where

$$\tilde{\mathbf{E}}'_2 \equiv \tilde{\mathbf{E}}_2(\mathbf{k}', \omega'),$$

$$[\tilde{\mathbf{E}}_1^*]^\prime \equiv [\tilde{\mathbf{E}}_1(-\mathbf{k}', -\omega')]^*,$$

$$f_2'' \equiv f_2(\mathbf{k} - \mathbf{k}', \omega - \omega', \mathbf{v}),$$

$$[f_1^*]'' \equiv [f_1(\mathbf{k} - \mathbf{k}', \omega - \omega', \mathbf{v})]^*.$$

Equations (B16)–(B18) can be solved approximately. First, retaining only first-order terms in the electric fields \mathbf{E}_1 and \mathbf{E}_2 , Eqs. (B16)–(B18) give

$$\delta f_0(\mathbf{k}, \omega, \mathbf{v}) = \frac{e}{m_e} \frac{\mathbf{E}_s(\mathbf{k}, \omega) \cdot \partial_{\mathbf{v}} f_M(\mathbf{v})}{-i(\omega - \mathbf{k} \cdot \mathbf{v})}, \quad (\text{B19})$$

$$f_1(\mathbf{k}, \omega, \mathbf{v}) = \frac{e}{m_e} \frac{\mathbf{E}_1(\mathbf{k}, \omega) \cdot \partial_{\mathbf{v}} f_M(\mathbf{v})}{-i(\omega_{LW} + \omega - \mathbf{k} \cdot \mathbf{v})}, \quad (\text{B20})$$

$$f_2(\mathbf{k}, \omega, \mathbf{v}) = \frac{e}{m_e} \frac{\tilde{\mathbf{E}}_2(\mathbf{k}, \omega) \cdot \partial_{\mathbf{v}} f_M(\mathbf{v})}{-i(2\omega_{LW} + \omega - \mathbf{k} \cdot \mathbf{v})}. \quad (\text{B21})$$

Substituting the above approximate expressions for $\delta f_0(\mathbf{k}, \omega, \mathbf{v})$, $f_1(\mathbf{k}, \omega, \mathbf{v})$, and $f_2(\mathbf{k}, \omega, \mathbf{v})$ into the right-hand side (rhs) of Eq. (B17), one obtains

$$\begin{aligned} f_1(\mathbf{k}, \omega, \mathbf{v}) &= \frac{e}{m_e} \frac{[\mathbf{E}_1(\mathbf{k}, \omega) + \mathbf{h}_1(\mathbf{k}, \omega)] \cdot \partial_{\mathbf{v}} f_0(\mathbf{v})}{-i(\omega_{LW} + \omega - \mathbf{k} \cdot \mathbf{v})} \\ &- \frac{e^2}{m_e} \frac{1}{(\omega_{LW} + \omega - \mathbf{k} \cdot \mathbf{v})} \\ &\times \iint d\mathbf{k}' d\omega' \mathbf{E}_s(\mathbf{k}', \omega') \cdot \partial_{\mathbf{v}} \left[\frac{\mathbf{E}_1(\mathbf{k}' - \mathbf{k}, \omega' - \omega) \cdot \partial_{\mathbf{v}} f_M}{[\omega_{LW} + \omega' - \omega - (\mathbf{k}' - \mathbf{k}) \cdot \mathbf{v}]} \right] \\ &- \frac{e^2}{2m_e^2} \frac{1}{(\omega_{LW} + \omega - \mathbf{k} \cdot \mathbf{v})} \\ &\times \iint d\mathbf{k}' d\omega' \mathbf{E}_1(\mathbf{k}', \omega') \cdot \partial_{\mathbf{v}} \left[\frac{\mathbf{E}_s(\mathbf{k}' - \mathbf{k}, \omega' - \omega) \cdot \partial_{\mathbf{v}} f_M}{[\omega' - \omega - (\mathbf{k}' - \mathbf{k}) \cdot \mathbf{v}]} \right] \\ &+ \frac{e^2}{2m_e^2} \frac{1}{(\omega_{LW} + \omega - \mathbf{k} \cdot \mathbf{v})} \\ &\times \iint d\mathbf{k}' d\omega' \tilde{\mathbf{E}}_2(\mathbf{k}', \omega') \cdot \partial_{\mathbf{v}} \left[\frac{\mathbf{E}_1^*(\mathbf{k}' - \mathbf{k}, \omega' - \omega) \cdot \partial_{\mathbf{v}} f_M}{[\omega_{LW} + \omega' - \omega - (\mathbf{k}' - \mathbf{k}) \cdot \mathbf{v}]} \right] \\ &- \frac{e^2}{2m_e^2} \frac{1}{(\omega_{LW} + \omega - \mathbf{k} \cdot \mathbf{v})} \\ &\times \iint d\mathbf{k}' d\omega' \mathbf{E}_1^*(-\mathbf{k}', -\omega') \\ &\cdot \partial_{\mathbf{v}} \left[\frac{\tilde{\mathbf{E}}_2(\mathbf{k} - \mathbf{k}', \omega - \omega') \cdot \partial_{\mathbf{v}} f_M}{[2\omega_{LW} + \omega - \omega' - (\mathbf{k} - \mathbf{k}') \cdot \mathbf{v}]} \right]. \quad (\text{B22}) \end{aligned}$$

In order to solve Eq. (B22), $\mathbf{E}_1(\mathbf{k}, \omega)$ must first be computed. The Poisson equation, in conjunction with the continuity equation and the gauge condition $\nabla \cdot \mathbf{A} = 0$, gives

$$\mathbf{k} \cdot \mathbf{E}_1(\mathbf{k}, \omega) = \frac{4\pi \mathbf{k} \cdot \mathbf{J}_1(\mathbf{k}, \omega)}{i\omega_{LW}}, \quad (\text{B23})$$

$$\mathbf{J}_1(\mathbf{k}, \omega) = -e \int d^3 \mathbf{v} \mathbf{v} f_1(\mathbf{k}, \omega, \mathbf{v}), \quad (\text{B24})$$

where, consistent with the envelope approximation, $|\omega| \ll \omega_{LW}$.

Substituting Eq. (B22) into Eq. (B24) leads to

$$\mathbf{J}_1 = \mathbf{J}_1^0 + \delta \mathbf{J}_1^0 + \delta \mathbf{J}_1^1 + \delta \mathbf{J}_1^2, \quad (\text{B25})$$

$$\mathbf{J}_1^0 = \frac{e^2}{m_e} \int d^3 \mathbf{v} \left[\frac{\mathbf{v} \mathbf{E}_1(\mathbf{k}, \omega) \cdot \partial_{\mathbf{v}} f_0}{i(\omega_{LW} + \omega - \mathbf{k} \cdot \mathbf{v})} \right], \quad (\text{B26})$$

$$\begin{aligned} \delta \mathbf{J}_1^0 &= \frac{e^2}{m_e} \int d^3 \mathbf{v} \left[\frac{\mathbf{v} \mathbf{h}_1(\mathbf{k}, \omega) \cdot \partial_{\mathbf{v}} f_0}{i(\omega_{LW} + \omega - \mathbf{k} \cdot \mathbf{v})} \right] \\ &+ \frac{e^3}{m_e^2} \int d\mathbf{k}' \int d\omega' \int d^3 \mathbf{v} \frac{\mathbf{v} \mathbf{E}_s(\mathbf{k}', \omega')}{(\omega_{LW} + \omega - \mathbf{k} \cdot \mathbf{v})} \\ &\cdot \partial_{\mathbf{v}} \left[\frac{\mathbf{E}_1(\mathbf{k}' - \mathbf{k}, \omega' - \omega) \cdot \partial_{\mathbf{v}} f_M}{[\omega_{LW} + \omega' - \omega - (\mathbf{k}' - \mathbf{k}) \cdot \mathbf{v}]} \right] \\ &+ \frac{e^3}{m_e^2} \int d\mathbf{k}' \int d\omega' \int d^3 \mathbf{v} \frac{\mathbf{v} \mathbf{E}_1(\mathbf{k}', \omega')}{(\omega_{LW} + \omega - \mathbf{k} \cdot \mathbf{v})} \\ &\cdot \partial_{\mathbf{v}} \left[\frac{\mathbf{E}_s(\mathbf{k}' - \mathbf{k}, \omega' - \omega) \cdot \partial_{\mathbf{v}} f_M}{[\omega' - \omega - (\mathbf{k}' - \mathbf{k}) \cdot \mathbf{v}]} \right], \quad (\text{B27}) \end{aligned}$$

$$\begin{aligned} \delta \mathbf{J}_1^1 &= -\frac{e^3}{2m_e^2} \int d\mathbf{k}' \int d\omega' \int d^3 \mathbf{v} \frac{\mathbf{v} \tilde{\mathbf{E}}_2(\mathbf{k}', \omega')}{(\omega_{LW} + \omega - \mathbf{k} \cdot \mathbf{v})} \\ &\cdot \partial_{\mathbf{v}} \left[\frac{\mathbf{E}_1^*(\mathbf{k}' - \mathbf{k}, \omega' - \omega) \cdot \partial_{\mathbf{v}} f_0}{[\omega_{LW} + \omega' - \omega - (\mathbf{k}' - \mathbf{k}) \cdot \mathbf{v}]} \right], \quad (\text{B28}) \end{aligned}$$

$$\delta \mathbf{J}_1^2 = \frac{e^3}{2m_e^2} \int d\mathbf{k}' \int d\omega' \int d^3\mathbf{v} \frac{\mathbf{v} \mathbf{E}_1^*(-\mathbf{k}', -\omega')}{(\omega_{\text{LW}} + \omega - \mathbf{k} \cdot \mathbf{v})} \cdot \partial_{\mathbf{v}} \left[\frac{\tilde{\mathbf{E}}_2(\mathbf{k} - \mathbf{k}', \omega - \omega') \cdot \partial_{\mathbf{v}} f_0}{2\omega_{\text{LW}} + \omega - \omega' - (\mathbf{k} - \mathbf{k}') \cdot \mathbf{v}} \right]. \quad (\text{B29})$$

Note that since \mathbf{E}_1 is a longitudinal field,

$$\mathbf{E}_1(\mathbf{k}, \omega) = \frac{\mathbf{k} [\mathbf{k} \cdot \mathbf{E}_1(\mathbf{k}, \omega)]}{k^2}. \quad (\text{B30})$$

Equation (B26) is evaluated, using the approximation $|\omega| \ll \omega_{\text{LW}}$ to give

$$\frac{4\pi \mathbf{k} \cdot \mathbf{J}_1^0}{i\omega_{\text{LW}}} = -\chi_e(\mathbf{k}, \omega + \omega_{\text{LW}}) \mathbf{k} \cdot \mathbf{E}_1(\mathbf{k}, \omega), \quad (\text{B31})$$

where

$$\chi_e(\mathbf{k}, \omega) \equiv \frac{4\pi e^2}{m_e k^2} \int d^3\mathbf{v} \left[\frac{\mathbf{k} \cdot \partial_{\mathbf{v}} f_0}{\omega - \mathbf{k} \cdot \mathbf{v}} \right].$$

Equation (B27) is evaluated similarly to yield

$$\frac{4\pi \mathbf{k} \cdot \delta \mathbf{J}_1^0(\mathbf{k}, \omega)}{i\omega_{\text{LW}}} = -\chi_e(\mathbf{k}, \omega + \omega_{\text{LW}}) \mathbf{k} \cdot \mathbf{h}_1(\mathbf{k}, \omega) + i \int d\mathbf{k}' \int d\omega' \left[\mathbf{k} \cdot \mathbf{E}_1(\mathbf{k}', \omega') \frac{\delta n_{eS}(\mathbf{k}' - \mathbf{k}, \omega' - \omega)}{n_{e0}} \right]. \quad (\text{B32})$$

To obtain the right-hand side of Eq. (B32), it was assumed that $|\omega|, |\omega'| \ll \omega_{\text{LW}}$,

$$|\omega' - \omega| \leq |\mathbf{k}' - \mathbf{k}| c_s \ll |(\mathbf{k}' - \mathbf{k}) \cdot \mathbf{v}| \sim |\mathbf{k}' - \mathbf{k}| v_{\text{the}},$$

and the relation

$$\delta n_{eS}(\mathbf{k}, \omega) = -e\phi_{eS}(\mathbf{k}, \omega)/T_{e0},$$

where $\mathbf{E}_s(\mathbf{k}, \omega) = -i\mathbf{k}\phi_{eS}(\mathbf{k}, \omega)$ was used.

Using the approximations $|\omega - \mathbf{k} \cdot \mathbf{v}| \ll \omega_{\text{LW}}$ and

$$|\omega' - \omega - (\mathbf{k}' - \mathbf{k}) \cdot \mathbf{v}| \ll \omega_{\text{LW}},$$

neglecting smaller terms of the order $\mathbf{k} \cdot \mathbf{v}/\omega_{\text{LW}} \sim k\lambda_{\text{De}} \ll 1$, and applying two successive integration by parts in velocity space, Eq. (B28) is evaluated:

$$\begin{aligned} \delta \mathbf{J}_1^1(\mathbf{k}, \omega) &= -\frac{e^3 n_{e0}}{2m_e^2 \omega_{\text{LW}}^3} \int d\mathbf{k}' \int d\omega' [\mathbf{E}_1^*(\mathbf{k}' - \mathbf{k}, \omega' - \omega) \cdot \mathbf{k}] \tilde{\mathbf{E}}_2(\mathbf{k}', \omega') \\ &\quad - \frac{e^3 n_{e0}}{2m_e^2 \omega_{\text{LW}}^3} \int d\mathbf{k}' \int d\omega' \mathbf{E}_1^*(\mathbf{k}' - \mathbf{k}, \omega' - \omega) [\tilde{\mathbf{E}}_2(\mathbf{k}', \omega') \cdot \mathbf{k}] \\ &\quad - \frac{e^3 n_{e0}}{2m_e^2 \omega_{\text{LW}}^3} \int d\mathbf{k}' \int d\omega' \tilde{\mathbf{E}}_2(\mathbf{k}', \omega') \\ &\quad \times [\mathbf{E}_1^*(\mathbf{k}' - \mathbf{k}, \omega' - \omega) \cdot (\mathbf{k}' - \mathbf{k})]. \end{aligned} \quad (\text{B33})$$

Similarly, using the same approximations and integration by parts, Eq. (B30) is evaluated:

$$\begin{aligned} \delta \mathbf{J}_1^2(\mathbf{k}, \omega) &= \frac{e^3 n_{e0}}{4m_e^2 \omega_{\text{LW}}^3} \int d\mathbf{k}' \int d\omega' \mathbf{E}_1^*(-\mathbf{k}', -\omega') [\tilde{\mathbf{E}}_2(\mathbf{k} - \mathbf{k}', \omega - \omega') \cdot \mathbf{k}] \\ &\quad + \frac{e^3 n_{e0}}{4m_e^2 \omega_{\text{LW}}^3} \int d\mathbf{k}' \int d\omega' [\mathbf{E}_1^*(-\mathbf{k}', -\omega') \cdot \mathbf{k}] \\ &\quad \times \tilde{\mathbf{E}}_2(\mathbf{k} - \mathbf{k}', \omega - \omega'). \end{aligned} \quad (\text{B34})$$

Equation (B34) is recast using the change of variables $\mathbf{k}'' = \mathbf{k} - \mathbf{k}'$ and $\omega'' = \omega - \omega'$:

$$\begin{aligned} & \delta \mathbf{J}_1^2(\mathbf{k}, \omega) \\ &= \frac{e^3 n_{e0}}{4m_e^2 \omega_{LW}^3} \int d\mathbf{k}'' \int d\omega'' \mathbf{E}_1^*(\mathbf{k}'' - \mathbf{k}, \omega'' - \omega) [\tilde{\mathbf{E}}_2(\mathbf{k}'', \omega'') \cdot \mathbf{k}] \\ &+ \frac{e^3 n_{e0}}{4m_e^2 \omega_{LW}^3} \int d\mathbf{k}'' \int d\omega'' [\mathbf{E}_1^*(\mathbf{k}'' - \mathbf{k}, \omega'' - \omega) \cdot \mathbf{k}] \\ &\times \tilde{\mathbf{E}}_2(\mathbf{k}'', \omega''). \end{aligned} \quad (\text{B35})$$

Summing Eqs. (B33) and (B35), rearranging the resulting equation, and using the fact that $\tilde{\mathbf{E}}_2$ is a transverse field, i.e., $\tilde{\mathbf{E}}_2(\mathbf{k}', \omega') \cdot \mathbf{k}' = 0$, one obtains

$$\begin{aligned} & \delta \mathbf{J}_1^1 + \delta \mathbf{J}_1^2 \\ &= \frac{ie^3 n_{e0}}{4m_e^2 \omega_{LW}^3} \int d\mathbf{k}' \int d\omega' [\mathbf{E}_1^*(\mathbf{k}' - \mathbf{k}, \omega' - \omega) \cdot i\mathbf{k}'] \tilde{\mathbf{E}}_2(\mathbf{k}', \omega') \\ &- \frac{ie^3 n_{e0}}{4m_e^2 \omega_{LW}^3} \int d\mathbf{k}' \int d\omega' [\mathbf{E}_1^*(\mathbf{k}' - \mathbf{k}, \omega' - \omega) \cdot i(\mathbf{k} - \mathbf{k}')] \tilde{\mathbf{E}}_2(\mathbf{k}', \omega') \\ &+ \frac{ie^3 n_{e0}}{4m_e^2 \omega_{LW}^3} \int d\mathbf{k}' \int d\omega' [\tilde{\mathbf{E}}_2(\mathbf{k}', \omega') \cdot i(\mathbf{k} - \mathbf{k}')] \\ &\times \mathbf{E}_1^*(\mathbf{k}' - \mathbf{k}, \omega' - \omega). \end{aligned} \quad (\text{B36})$$

Using the approximations $\chi_e(\mathbf{k}, \omega + \omega_{LW}) \approx -\omega_{pe0}^2 / \omega_{LW}^2$ and $\omega_0 \sim 2\omega_{LW}$, and transforming Eq. (B32) back to configuration space with $i\mathbf{k} \rightarrow \nabla$, results in

$$\begin{aligned} \nabla \cdot \delta \mathbf{J}_0^1 &= \frac{ie^3 n_{e0}}{4m_e^2 \omega_{LW}^3} \nabla \cdot \left[\nabla (\mathbf{E}_1^* \cdot \tilde{\mathbf{E}}_2) \right. \\ &\left. - (\tilde{\mathbf{E}}_2 \cdot \nabla) \mathbf{E}_1^* - (\mathbf{E}_1^* \cdot \nabla) \tilde{\mathbf{E}}_2 \right]. \end{aligned} \quad (\text{B37})$$

Transforming Eq. (B36) back to configuration space, one obtains

$$\begin{aligned} \nabla \cdot (\delta \mathbf{J}_1^1 + \delta \mathbf{J}_1^2) &= \frac{ie^3 n_{e0}}{4m_e^2 \omega_{LW}^3} \nabla \cdot \left[(\mathbf{E}_1^* \cdot \nabla) \tilde{\mathbf{E}}_2 \right. \\ &\left. - \tilde{\mathbf{E}}_2 (\nabla \cdot \mathbf{E}_1^*) - (\tilde{\mathbf{E}}_2 \cdot \nabla) \mathbf{E}_1^* \right]. \end{aligned} \quad (\text{B38})$$

Substituting Eqs. (B25), (B31), (B32), and (B36) into Eq. (B23) and transforming back to configuration space with $i\mathbf{k} \rightarrow \nabla$, one finds

$$\begin{aligned} & \mathcal{F}^{-1} \left[i\mathbf{k} \cdot \mathbf{E}_1(\mathbf{k}, \omega) \epsilon(k, \omega + \omega_{LW}) \right] \\ &+ \mathcal{F}^{-1} \left\{ i \int d\mathbf{k}' \int d\omega' \left[\mathbf{k} \cdot \mathbf{E}_1(\mathbf{k}', \omega') \frac{\delta n_{eS}(\mathbf{k}' - \mathbf{k}, \omega' - \omega)}{n_{e0}} \right] \right\} \\ &= \frac{e\omega_{pe0}^2}{4m_e \omega_{LW}^4} \nabla \cdot \left[\nabla (\mathbf{E}_1^* \cdot \tilde{\mathbf{E}}_2) - \tilde{\mathbf{E}}_2 (\nabla \cdot \mathbf{E}_1^*) \right], \end{aligned} \quad (\text{B39})$$

where the operator \mathcal{F}^{-1} denotes the inverse Fourier transform in space and time, and

$$\begin{aligned} \epsilon(\mathbf{k}, \omega + \omega_{LW}) &= 1 + \chi_e(\mathbf{k}, \omega + \omega_{LW}), \\ &\approx \frac{2\omega_{pe0} [\omega(k) + i\gamma_L(k)] - 3k^2 v_{the}^2}{-\omega_{pe0}^2}. \end{aligned}$$

In this approximation, Eq. (B39) can then be evaluated explicitly to yield the well-known Zakharov equation

$$\begin{aligned} \nabla \cdot \left\{ \left[2i\omega_{pe0} (\partial_t + \gamma_L \circ) + 3v_{the}^2 \nabla^2 + \omega_{pe0}^2 \frac{\delta n_{eS}}{n_{e0}} \right] \mathbf{E}_1 \right\} \\ = \frac{e}{4m_e} \nabla \cdot \left[\nabla (\mathbf{E}_1^* \cdot \tilde{\mathbf{E}}_2) - \tilde{\mathbf{E}}_2 (\nabla \cdot \mathbf{E}_1^*) \right], \end{aligned} \quad (\text{B40})$$

where the operator “ \circ ” is used to denote a convolution in configuration space (see DuBois *et al.*⁹). The iterative procedure

leading to Eq. (B22) is based on the assumption that the perturbations of the distribution function are small compared to the background distribution function f_M . This leads to the validity estimates for the Zakharov model: $|\mathbf{E}_1|^2/4\pi n_{e0}T_{e0} \ll 1$, $|\mathbf{E}_2|^2/4\pi n_{e0}T_{e0} \ll 1$, $|e\phi_{eS}/T_{e0}| \ll 1$, $|\delta n_{eS}/n_{e0}| \ll 1$, and $k_{LW}\lambda_{De} \ll 1$. These involve qualitative arguments, and the quantitative strengths of the inequalities are not known *a priori*. Furthermore, this derivation does not account for the evolution of the background electron-velocity distribution function, which is here taken to be a fixed Maxwellian, $f_M(v)$. This is why detailed quantitative comparison of the ZAK model with RPIC is desirable.

The equation for the low-frequency density fluctuation can be derived in a similar way. The result is

$$\begin{aligned} & \left[\partial_t^2 + 2iv_i \circ \partial_t - c_s^2 \nabla^2 \right] \delta n \\ &= \frac{1}{16\pi m_i} \nabla^2 \left[|\mathbf{E}_1|^2 + \frac{1}{4} |\mathbf{E}_2|^2 \right]. \end{aligned} \quad (\text{B41})$$

In the simulations reported in the text where the laser is a uniform plane wave, the ponderomotive pressure of the pump [the second term on the right-hand side of Eq. (41)] does not contribute.

Appendix C: Degenerate LW's with Overlapping Beams

In the presence of two identical beams propagating at angles $\theta = \pm\theta_b$ with respect to the x axis, the locations of the most linearly unstable LW are given by algebraic solutions of the following two sets of equations:

$$\begin{aligned} & \left(k_{x1} \cos \theta_b + k_{y1} \sin \theta_b - \frac{1}{2} k_0 \lambda_{De} \right)^2 \\ & + \left(-k_{x1} \sin \theta_b + k_{y1} \cos \theta_b \right)^2 = \kappa^2, \end{aligned} \quad (\text{C1})$$

$$\begin{aligned} & \left(k_{x1} \cos \theta_b + k_{y1} \sin \theta_b - \frac{1}{2} k_0 \lambda_{De} \right)^2 - \left(-k_{x1} \sin \theta_b + k_{y1} \cos \theta_b \right)^2 \\ & = \left(\frac{1}{2} k_0 \lambda_{De} \right)^2, \end{aligned} \quad (\text{C2})$$

$$\begin{aligned} & \left(k_{x2} \cos \theta_b - k_{y2} \sin \theta_b - \frac{1}{2} k_0 \lambda_{De} \right)^2 \\ & + \left(k_{x2} \sin \theta_b + k_{y2} \cos \theta_b \right)^2 = \kappa^2, \end{aligned} \quad (\text{C3})$$

$$\begin{aligned} & \left(k_{x2} \cos \theta_b - k_{y2} \sin \theta_b - \frac{1}{2} k_0 \lambda_{De} \right)^2 \\ & - \left(k_{x2} \sin \theta_b + k_{y2} \cos \theta_b \right)^2 = \left(\frac{1}{2} k_0 \lambda_{De} \right)^2, \end{aligned} \quad (\text{C4})$$

where κ is defined by

$$\begin{aligned} \kappa^2 &\equiv \frac{1}{2} \Omega - \left(\frac{1}{2} k_0 \lambda_{De} \right)^2, \\ \Omega &\equiv \frac{2}{3} \left(\frac{\omega_0}{\omega_{pe0}} - 2 \right). \end{aligned}$$

Equations (C1)–(C4) are obtained by rotating Eqs. (34) and (35) through angles $\pm\theta_b$. For arbitrary temperature T_{e0} and density n_{e0} , the solutions of Eqs. (C1)–(C2) and (C3)–(C4) result in eight distinct modes since each set of circles and hyperbolae will have four distinct intersections. There exists, however, a combination of temperature and density such that two of the eight solutions become degenerate, i.e., there will be only seven distinct solutions for (k_{x1}, k_{y1}) and (k_{x2}, k_{y2}) . By symmetry, this special condition occurs when $k_{y1} = k_{y2} = 0$, in which case the location $k_x = k_{x1} = k_{x2}$ of the degenerate mode is given by

$$\begin{aligned} & \left(k_x \cos \theta_b - \frac{1}{2} k_0 \lambda_{De} \right)^2 + k_x^2 \sin^2 \theta_b \\ & = \frac{1}{3} \left(\frac{\omega_0}{\omega_{pe0}} - 2 \right) - \left(\frac{1}{2} k_0 \lambda_{De} \right)^2, \end{aligned} \quad (\text{C5})$$

$$\left(k_x \cos \theta_b - \frac{1}{2} k_0 \lambda_{De} \right)^2 - k_x^2 \sin^2 \theta_b = \left(\frac{1}{2} k_0 \lambda_{De} \right)^2. \quad (\text{C6})$$

Equations (C5) and (C6) are augmented by the electromagnetic dispersion relation

$$\omega_0^2 = \omega_{pe0}^2 + k_0^2 c^2. \quad (C7)$$

Equations (C5)–(C7) are solved for the background electron density given by

$$\frac{n_{e0}}{n_c} = 4 \left[-\sigma + (\sigma^2 - 8\sigma + 4)^{1/2} \right]^{-2},$$

$$\sigma \equiv \frac{2}{3} \left[\frac{511}{T_e(\text{keV})} \right] \cos^2(2\theta_b). \quad (C8)$$

REFERENCES

1. W. Seka, D. H. Edgell, J. F. Myatt, A. V. Maximov, R. W. Short, V. N. Goncharov, and H. A. Baldis, *Phys. Plasmas* **16**, 052701 (2009).
2. J. A. Delettrez, V. N. Goncharov, P. B. Radha, C. Stoeckl, A. V. Maximov, T. C. Sangster, J. A. Frenje, and D. Shvarts, *Bull. Am. Phys. Soc.* **53**, 248 (2008).
3. V. A. Smalyuk, D. Shvarts, R. Betti, J. A. Delettrez, D. H. Edgell, V. Yu. Glebov, V. N. Goncharov, R. L. McCrory, D. D. Meyerhofer, P. B. Radha, S. P. Regan, T. C. Sangster, W. Seka, S. Skupsky, C. Stoeckl, B. Yaakobi, J. A. Frenje, C. K. Li, R. D. Petrasso, and F. H. Séguin, *Phys. Rev. Lett.* **100**, 185005 (2008).
4. B. Yaakobi, T. R. Boehly, T. C. Sangster, D. D. Meyerhofer, B. A. Remington, P. G. Allen, S. M. Pollaine, H. E. Lorenzana, K. T. Lorenz, and J. A. Hawreliak, *Phys. Plasmas* **15**, 062703 (2008).
5. M. V. Goldman, *Ann. Phys.* **38**, 117 (1966); C. S. Liu and M. N. Rosenbluth, *Phys. Fluids* **19**, 967 (1976); A. B. Langdon, B. F. Lasinski, and W. L. Kruer, *Phys. Rev. Lett.* **43**, 133 (1979); S. J. Karttunen, *Plasma Phys.* **22**, 151 (1980); A. M. Rubenchik, *Sov. Phys.-JETP* **41**, 498 (1975); B. Bezzerides and D. F. DuBois, *Phys. Rev. Lett.* **36**, 729 (1976); R. Z. Sagdeev *et al.*, *Sov. Phys.-JETP* **55**, 74 (1982); H. H. Chen and C. S. Liu, *Phys. Rev. Lett.* **39**, 881 (1977); J. Meyer, *Phys. Fluids B* **4**, 2934 (1992).
6. A. Simon, R. W. Short, E. A. Williams, and T. Dewandre, *Phys. Fluids* **26**, 3107 (1983); B. B. Afeyan and E. A. Williams, *Phys. Rev. Lett.* **75**, 4218 (1995).
7. H. A. Baldis and C. J. Walsh, *Phys. Rev. Lett.* **47**, 1658 (1981); D. M. Villeneuve, H. A. Baldis, and C. J. Walsh, *Phys. Fluids* **28**, 1454 (1985); K. A. Tanaka, B. Boswell, R. S. Craxton, L. M. Goldman, F. Guglielmi, W. Seka, R. W. Short, and J. M. Soures, *Phys. Fluids* **28**, 2910 (1985); W. Seka, B. B. Afeyan, R. Boni, L. M. Goldman, R. W. Short, K. Tanaka, and T. W. Johnston, *Phys. Fluids* **28**, 2570 (1985); P. E. Young *et al.*, *Phys. Rev. Lett.* **61**, 2766 (1988); W. Seka, R. E. Bahr, R. W. Short, A. Simon, R. S. Craxton, D. S. Montgomery, and A. E. Rubenchik, *Phys. Fluids B* **4**, 2232 (1992).
8. Hard x rays are signatures for hot-electron generation and preheat.
9. D. F. DuBois, D. A. Russell, and H. A. Rose, *Phys. Rev. Lett.* **74**, 3983 (1995).
10. H. X. Vu, D. F. DuBois, and B. Bezzerides, *Phys. Rev. Lett.* **86**, 4306 (2001); *ibid.*, *Phys. Plasmas* **14**, 012702 (2007).
11. K. Y. Sanbonmatsu *et al.*, *Phys. Rev. Lett.* **82**, 932 (1999); *ibid.*, *Phys. Plasmas* **7**, 1723 (2000).
12. J. L. Kline *et al.*, *Phys. Rev. Lett.* **94**, 175003 (2005); J. L. Kline *et al.*, *Phys. Plasmas* **13**, 055906 (2006).
13. In point of fact, we show in Appendix B that the ZAK model can be derived from the basic equations of the RPIC model under certain conditions.
14. R. Yan *et al.*, *Phys. Rev. Lett.* **103**, 175002 (2009).
15. H. X. Vu, B. Bezzerides, and D. F. DuBois, *J. Comput. Phys.* **156**, 12 (1999).
16. H. X. Vu, J. M. Wallace, and B. Bezzerides, *Phys. Plasmas* **1**, 3542 (1994).
17. D. A. Russell and D. F. DuBois, *Phys. Rev. Lett.* **86**, 428 (2001).
18. D. F. DuBois, D. A. Russell, H. X. Vu, J. F. Myatt, and W. Seka, “The Nonlinear Source for Radiation, from the Two-Plasmon-Decay Instability, at One-Half of the Laser Frequency,” in preparation (2010).
19. In the absence of SRS, the vector potential envelopes \mathbf{a}_{-1} and \mathbf{a}_1 (with carrier frequencies $\omega_0 - \omega_{pe0}$ and $\omega_0 + \omega_{pe0}$, respectively) are set to 0.
20. J. F. Myatt, J. A. Delettrez, W. Seka, D. H. Edgell, A. V. Maximov, R. W. Short, D. F. DuBois, D. A. Russell, and H. X. Vu, *Bull. Am. Phys. Soc.* **54**, 145 (2009).
21. R. W. Short, *Bull. Am. Phys. Soc.* **54**, 144 (2009).
22. If above the LDI threshold, a Langmuir wave with wave number $k_{LW}\lambda_{De}$ will decay into a pair of LW and IAW with $k_{LW1}\lambda_{De} = -k_{LW}\lambda_{De} + \Delta k\lambda_{De}$ and $k_{IAW1}\lambda_{De} = 2k_{LW}\lambda_{De} - \Delta k\lambda_{De}$, where $\Delta k\lambda_{De} = 1.5(m_e/m_i)^{1/2}$ (cf. Ref. 11). This process can continue where the LW resulting from the primary LDI step can result in a secondary LDI decay step. Repeated LDI decays may occur until the resulting LW’s are of sufficiently long wavelengths that LW cavitation can be nucleated.⁹
23. W. L. Kruer, *The Physics of Laser-Plasma Interactions*, *Frontiers in Physics*, Vol. 73, edited by D. Pines (Addison-Wesley, Redwood City, CA, 1988), p. 133.TM
24. The Workshop on SRS/SBS Non-Linear Saturation at Wente Vineyards, Livermore, CA, University of California Report UCRL-JC-148983-SUM (2002).

Publications and Conference Presentations

Publications

- T. R. Boehly, R. E. Olson, P. M. Celliers, D. H. Munro, W. Seka, O. L. Landen, G. W. Collins, L. J. Suter, T. C. Sangster, and D. D. Meyerhofer, "The Effect of Condensates and Inner Coatings on Vacuum Hohlraum Targets," *Phys. Plasmas* **17**, 032701 (2010).
- W. R. Donaldson, J. R. Marciante, and R. G. Roides, "An Optical Replicator for Single-Shot Measurements at 10 GHz With a Dynamic Range of 1800:1," *IEEE J. Quantum Electron.* **46**, 191 (2010).
- R. Florido, R. C. Mancini, T. Nagayama, R. Tommasini, J. A. Delettrez, S. P. Regan, V. A. Smalyuk, R. Rodríguez, and J. M. Gil, "Argon *K*-Shell and Bound-Free Emission from OMEGA Direct-Drive Implosion Cores," *High Energy Density Phys.* **6**, 70 (2010).
- T. B. Jones, R. Gram, K. Kentch, and D. R. Harding, "Capillarity and Dielectrophoresis of Liquid Deuterium," *J. Phys. D: Appl. Phys.* **42**, 225505 (2009).
- R. L. McCrory, D. D. Meyerhofer, S. J. Loucks, S. Skupsky, R. E. Bahr, R. Betti, T. R. Boehly, R. S. Craxton, T. J. B. Collins, J. A. Delettrez, W. R. Donaldson, R. Epstein, K. A. Fletcher, C. Freeman, J. A. Frenje, V. Yu. Glebov, V. N. Goncharov, D. R. Harding, P. A. Jaanimagi, R. L. Keck, J. H. Kelly, T. J. Kessler, J. D. Kilkenny, J. P. Knauer, C. K. Li, L. D. Lund, J. A. Marozas, P. W. McKenty, F. J. Marshall, S. F. B. Morse, S. Padalino, R. D. Petrasso, P. B. Radha, S. P. Regan, S. Roberts, T. C. Sangster, F. H. Séguin, W. Seka, V. A. Smalyuk, J. M. Soures, C. Stoeckl, K. A. Thorp, B. Yaakobi, and J. D. Zuegel, "Direct-Drive Inertial Fusion Research at the University of Rochester's Laboratory for Laser Energetics: A Review," in *Current Trends in International Fusion Research—Proceedings of the Fifth Symposium*, edited by E. Panarella and R. Raman (NRC Press, Ottawa, Canada, 2008), pp. 267–277.
- A. V. Okishev, "Optical Differentiation and Multimillijoule ~150 ps Pulse Generation in a Regenerative Amplifier with a Temperature-Tuned Intracavity Volume Bragg Grating," *Appl. Opt.* **49**, 1331 (2010).
- S. P. Regan, N. B. Meezan, L. J. Suter, D. J. Strozzi, W. L. Kruer, D. Meeker, S. H. Glenzer, W. Seka, C. Stoeckl, V. Yu. Glebov, T. C. Sangster, D. D. Meyerhofer, R. L. McCrory, E. A. Williams, O. S. Jones, D. A. Callahan, M. D. Rosen, O. L. Landen, C. Sorce, and B. J. MacGowan, "Suprathermal Electrons Generated by the Two-Plasmon-Decay Instability in Gas-Filled *Hohlraums*," *Phys. Plasmas* **17**, 020703 (2010).
- H. F. Robey, T. R. Boehly, R. E. Olson, A. Nikroo, P. M. Celliers, O. L. Landen, and D. D. Meyerhofer, "Experimental Validation of a Diagnostic Technique for Tuning the Fourth Shock Timing on National Ignition Facility," *Phys. Plasmas* **17**, 012703 (2010).
- J. E. Schoenly, W. Seka, and P. Rechmann, "Investigation Into the Optimum Beam Shape and Fluence for Selective Ablation of Dental Calculus at $\lambda = 400$ nm," *Lasers Surg. Med.* **42**, 51 (2010).
- R. Shen, S. N. Shafir, C. Miao, M. Wang, J. C. Lambropoulos, S. D. Jacobs, and H. Yang, "Synthesis and Corrosion Study of Zirconia-Coated Carbonyl Iron Particles," *J. Colloid Interface Sci.* **342**, 49 (2010).
- L. Sun, S. Jiang, and J. R. Marciante, "All-Fiber Optical Magnetic-Field Sensor Based on Faraday Rotation in Highly Terbium-Doped Fiber," *Opt. Express* **18**, 5407 (2010).
- L. Sun, S. Jiang, J. D. Zuegel, and J. R. Marciante, "All-Fiber Optical Isolator Based on Faraday Rotation in Highly Terbium-Doped Fiber," *Opt. Lett.* **35**, 706 (2010).

Forthcoming Publications

S.-W. Bahk, E. Fess, B. E. Kruschwitz, and J. D. Zuegel, “A High-Resolution, Adaptive Beam-Shaping System for High-Power Lasers,” to be published in *Optics Express*.

M. A. Barrios, D. G. Hicks, T. R. Boehly, D. E. Fratanduono, J. H. Eggert, P. M. Celliers, G. W. Collins, and D. D. Meyerhofer, “High-Precision Measurements of the Equation of State of Hydrocarbons at 1–10 Mbar Using Laser-Driven Shock Waves,” to be published in *Physics of Plasmas* (invited).

Z. Bei, T. B. Jones, and D. R. Harding, “Electric-Field Centering of Double-Emulsion Droplets Suspended in a Density Gradient,” to be published in *Soft Matter*.

R. Betti, P. Y. Chang, B. K. Spears, K. S. Anderson, J. Edwards, M. Fatenejad, J. D. Lindl, R. L. McCrory, R. Nora, and D. Shvarts, “Thermonuclear Ignition in Inertial Confinement Fusion and Comparison with Magnetic Confinement,” to be published in *Physics of Plasmas* (invited).

J. Bromage, C. Dorrer, J. R. Marciante, M. J. Shoup III, and J. D. Zuegel, “Modal Measurement of a Large-Mode-Area Photonic-Crystal Fiber Amplifier Using Spatially Resolved Spectral Interferometry,” to be published in *Solid State Diode Laser Technology Review*.

P. Y. Chang, R. Betti, B. K. Spears, K. S. Anderson, J. Edwards, M. Fatenejad, J. D. Lindl, R. L. McCrory, R. Nora, and D. Shvarts, “Generalized Measurable Ignition Criterion for Inertial Confinement Fusion,” to be published in *Physical Review Letters*.

C. Dorrer and J. Bromage, “High-Sensitivity Optical Pulse Characterization Using Sagnac Electro-Optic Spectral Shearing Interferometry,” to be published in *Optics Letters*.

V. N. Goncharov, T. C. Sangster, T. R. Boehly, S. X. Hu, I. V. Igumenshchev, F. J. Marshall, R. L. McCrory, D. D. Meyerhofer, P. B. Radha, W. Seka, S. Skupsky, C. Stoeckl, D. T. Casey, J. A. Frenje, and R. D. Petrasso, “Demonstration of the Highest Deuterium–Tritium Areal Density Using Multiple-Picket Cryogenic Designs on OMEGA,” to be published in *Physical Review Letters*.

W. Guan and J. R. Marciante, “Power Scaling of Single-Frequency Hybrid Brillouin/Ytterbium Fiber Lasers,” to be published in *IEEE Journal of Quantum Electronics*.

S. X. Hu, “Optimizing the FEDVR-TDCC Code for Exploring the Quantum Dynamics of Two-Electron Systems in Intense Laser Pulses,” to be published in *Physical Review E*.

H. Irie and R. Sobolewski, “Terahertz Electrical Response of Nanoscale Three-Branch Junctions,” to be published in the *Journal of Applied Physics*.

A. M. Kaplan, G. P. Agrawal, and D. N. Maywar, “Optical Square-Wave Clock Generation Based on an All-Optical Flip-Flop,” to be published in *IEEE Photonics Technology Letters*.

V. Kaushal, I. Iñiguex-de-la-Torre, H. Irie, G. Guarino, W. R. Donaldson, P. Ampadu, R. Sobolewski, and M. Margala, “A Study of Geometry Effects on the Performance of Ballistic Deflection Transistors,” to be published in *IEEE Transactions on Nanotechnology*.

J. P. Knauer, O. V. Gotchev, P. Y. Chang, D. D. Meyerhofer, A. Polomarov, R. Betti, J. A. Frenje, C. K. Li, M. J.-E. Manuel, R. D. Petrasso, J. R. Rygg, and F. H. Séguin, “Compressing Magnetic Fields with High-Energy Lasers,” to be published in *Physics of Plasmas* (invited).

R. L. McCrory, D. D. Meyerhofer, S. J. Loucks, S. Skupsky, J. M. Soures, R. Betti, T. R. Boehly, M. J. Bonino, R. S. Craxton, T. J. B. Collins, J. A. Delettrez, D. H. Edgell, R. Epstein, V. Yu. Glebov, V. N. Goncharov, D. R. Harding, R. L. Keck, J. H. Kelly, T. J. Kessler, J. P. Knauer, L. D. Lund, D. Jacobs-Perkins, J. R. Marciante, J. A. Marozas, F. J. Marshall, A. V. Maximov, P. W. McKenty, S. F. B. Morse, J. Myatt, S. G. Noyes, P. B. Radha, A. L. Rigatti, T. C. Sangster, W. Seka, V. A. Smalyuk, C. Stoeckl, K. A. Thorp, L. J. Waxer, M. D. Wittman, B. Yaakobi, J. D. Zuegel, K. A. Fletcher, C. Freeman, S. Padalino, J. A. Frenje, C. K. Li, R. D. Petrasso, and F. H. Séguin, “Direct-Drive Inertial Fusion Research at the University of Rochester’s Laboratory for Laser Energetics: A Review,” to be published in *6th Current Trends in International Fusion Research: A Review*.

P. W. McKenty, R. S. Craxton, F. J. Marshall, T. C. Sangster, J. A. Marozas, A. M. Cok, M. J. Bonino, D. R. Harding, D. D. Meyerhofer, R. L. McCrory, J. D. Kilkenny, A. Nikroo, J. Fooks, M. Hoppe, J. M. Edwards, A. J. MacKinnon, D. H. Munro, and R. J. Wallace, “Design of High-Neutron-Yield Polar-Drive Targets for Diagnostic Activation Experiments on the NIF,” to be published in the *Journal of Physics: Conference Series*.

C. Miao, J. C. Lambropoulos, and S. D. Jacobs, "Process Parameter Effects on Material Removal in Magnetorheological Finishing of Borosilicate Glass," to be published in *Applied Optics*.

P. M. Nilson, S. P. D. Mangles, L. Willingale, M. C. Kaluza, A. G. R. Thomas, M. Tatarakis, R. J. Clarke, K. L. Lancaster, S. Karsch, J. Schreiber, Z. Najmudin, A. E. Dangor, and K. Krushelnick, "Plasma Cavitation in Ultraintense Laser Interactions with Underdense Helium Plasmas," to be published in the *New Journal of Physics*.

J. Qiao, A. W. Schmid, L. J. Waxer, T. Nguyen, J. Bunkenburg, C. Kinglsey, A. Kozlov, and D. Weiner, "*In Situ* Detection and Analysis of Laser-Induced Damage on a 1.5-m Multilayer-Dielectric Grating Compressor for High-Energy, Petawatt-Class Laser Systems," to be published in *Optics Express*.

T. C. Sangster, V. N. Goncharov, R. Betti, T. R. Boehly, D. T. Casey, T. J. B. Collins, R. S. Craxton, J. A. Delettrez, D. H. Edgell, R. Epstein, K. A. Fletcher, J. A. Frenje, V. Yu. Glebov, D. R. Harding, S. X. Hu, I. V. Igumenshchev, J. P. Knauer, S. J. Loucks, C. K. Li, J. A. Marozas, F. J. Marshall, R. L. McCrory,

P. W. McKenty, D. D. Meyerhofer, P. M. Nilson, S. P. Padalino, R. D. Petrasso, P. B. Radha, S. P. Regan, F. H. Séguin, W. Seka, R. W. Short, D. Shvarts, S. Skupsky, V. A. Smalyuk, J. M. Soures, C. Stoeckl, W. Theobald, and B. Yaakobi, "Shock-Tuned Cryogenic-Deuterium-Tritium Implosion Performance on OMEGA," to be published in *Physics of Plasmas* (invited).

J. E. Schoenly, W. Seka, and P. Rechmann, "Selective Near-UV Ablation of Subgingival Dental Calculus: Measurement of Removal Rates," to be published in the *Proceedings of SPIE*.

V. A. Smalyuk, R. Betti, J. A. Delettrez, V. Yu. Glebov, D. D. Meyerhofer, P. B. Radha, S. P. Regan, T. C. Sangster, J. Sanz, W. Seka, C. Stoeckl, B. Yaakobi, J. A. Frenje, C. K. Li, R. D. Petrasso, and F. H. Séguin, "Implosion Experiments Using Glass Ablators for Direct-Drive Inertial Confinement Fusion," to be published in *Physical Review Letters*.

A. A. Solodov, M. Storm, J. F. Myatt, R. Betti, D. D. Meyerhofer, P. M. Nilson, W. Theobald, and C. Stoeckl, "Simulations of Electron-Beam Transport in Solid-Density Targets and the Role of Magnetic Collimation," to be published in the *Journal of Physics, Conference Series*.

Conference Presentations

J. E. Schoenly, W. Seka, and P. Rechmann, "Selective Near-UV Ablation of Dental Calculus: Measurement of Removal Rates," *BiOS 2010*, San Francisco, CA, 23–28 January 2010.

L. Sun, S. Jiang, and J. R. Marciante, "Compact All-Fiber Optical Faraday Isolator," *SPIE Photonics West–LASE*, San Francisco, CA, 23–28 January 2010.

The following presentations were made at *Advanced Solid-State Photonics*, San Diego, CA, 31 January–3 February 2010:

J. Bromage, C. Dorrer, and J. D. Zuegel, "High-Resolution Spatio-Spectral Characterization of Noncollinear Optical Parametric Amplifiers."

J. Bromage, C. Dorrer, and J. D. Zuegel, "Performance Trade-Offs for High-Repetition-Rate Noncollinear Optical Parametric Amplifiers."

R. Xin and J. D. Zuegel, "Directly Chirped Laser Source for Chirped-Pulse Amplification."

A. V. Okishev, D. Wang, D. Westerfeld, L. Shterengas, and G. Belenky, "Characterization of Highly Stable Mid-IR, GaSb-Based Laser Diodes," *Laser Applications to Chemical, Security and Environmental Analysis*, San Diego, CA, 31 January–4 February 2010.

The following presentations were made at the *19th Target Fabrication Meeting*, Orlando, FL, 21–26 February 2010:

Z. Bei, T. B. Jones, D. R. Harding, and A. Tucker-Schwartz, "Electric-Field Mediated Double-Emulsion Droplet Centering Using Density Gradient Suspension."

M. J. Bonino, D. R. Harding, S. G. Noyes, J. Fooks, D. Turner, M. D. Wittman, and L. D. Lund, "Stalk-Mounted Cryogenic Targets: Rationale and Results."

D. H. Edgell, M. D. Wittman, R. S. Craxton, D. R. Harding, B. Smith, and T. Lu, "Three-Dimensional Characterization of Cryogenic Targets Using X-Ray Phase-Contrast Imaging and Shadowgraphy at LLE."

D. R. Harding, T. B. Jones, R. Q. Gram, Z. Bei, W. Wang, M. Moynihan, and S.-J. Scott, "Mass Fabrication of Cryogenic Targets for Inertial Fusion Energy."

R. L. McCrory, "Inertial Confinement Fusion Research at the Laboratory for Laser Energetics."

P. W. McKenty, R. S. Craxton, J. A. Marozas, A. M. Cok, R. Epstein, M. J. Bonino, D. R. Harding, D. D. Meyerhofer, R. L. McCrory, J. D. Kilkenny, A. Nikroo, J. Fooks, M. Hoppe, J. M. Edwards, A. J. MacKinnon, D. H. Munro, and R. J. Wallace, "Results of Recent NIF Polar-Drive Diagnostic Activation Experiments."

M. Moynihan, D. R. Harding, and S. H. Chen, "Microfluidic T-Junctions to Mass Produce NIF and IFE Size Foam Targets."

S.-J. Scott, D. R. Harding, and J. Fooks, "Mechanical Forces that Develop in Foam Material During Evaporative Drying."

W. T. Shmayda, "Decontaminating Tritiated Surfaces with Humid Purge Streams."

W. Wang, T. B. Jones, and D. R. Harding, "On-Chip Double-Emulsion Droplet Assembly Using EWOD and DEP."

M. D. Wittman and D. R. Harding, "Development of NIF-Scale Polar-Drive Cryogenic Targets."

The following presentations were made at OFC 2010, San Diego, CA, 21–25 March 2010:

J. R. Marciante and W. Guan, "Single-Frequency Hybrid Brillouin/Ytterbium Fiber Laser with 1-W Output Power."

L. Sun, S. Jiang, and J. R. Marciante, "All-Fiber Optical Magnetic Field Sensor Based on Faraday Rotation."

D. R. Harding, T. B. Jones, and D. D. Meyerhofer, "Mass Production of Targets for Inertial Fusion Energy," 5th IAEA Technical Meeting, Vienna, Austria, 24–26 March 2010.

